Use of Ultrasound to Characterise and Estimate State-of-Charge, State-of-Health, and Temperature In Lithium-Ion Batteries

Daniel Carl Williams

A thesis submitted in partial fulfilment of the requirements for the degree of

Doctor of Philosophy

The University of Sheffield

Faculty of Engineering

School of Mechanical, Aerospace and Civil Engineering

Submission Date

June 2025

Abstract

Lithium-ion batteries have seen rapid adoption since the 1990s, a trend set to continue with global decarbonisation efforts. Electric vehicles represent a major driver of this growth. These batteries operate through the movement of lithium-ions between electrodes during charge and discharge. Current battery management systems do not exploit these internal changes directly, instead relying on charge counting, voltage, and impedance measurements.

Recent research has introduced ultrasound as a method to monitor internal changes by tracking variations in the ultrasonic signal, which reflect changes in electrode material properties. This has been applied to estimate state-of-charge and state-of-health, though the relationship between SOH and ultrasonic response remains unclear due to conflicting findings. This thesis addresses these inconsistencies and investigates the under-explored impact of temperature on the ultrasonic signal.

Long-term cycling experiments were used to track ultrasonic time-of-flight drift as a function of battery degradation, separating this from cyclical variations due to charge-discharge. The time-of- flight drift direction was suggested to be dependent on cathode chemistry. The ultrasonic method showed high sensitivity to SOH fluctuations across the battery lifecycle.

A thermal cycling method combined with a global sensitivity analysis was used to assess the effects of temperature (10 to 50 ℃) and state-of-charge (0 to 100%) on the ultrasonic signal. Results showed both variables independently affect the signal, with temperature having the dominant effect.

Two regression models—linear and Gaussian Process—were trained to predict SOC and temperature from ultrasonic data. The linear model demonstrated consistent stability and accuracy across varying noise levels, but was significantly influenced by data formatting.

This thesis focusses on the effects of temperature and state-of-charge on the ultrasonic signal to improve the accuracy of state-of-charge monitoring and has demonstrated the use of machine learning to predict both variables.

Declaration

I, the author, confirm that the Thesis is my own work. I am aware of the University's guidance on the Use of Unfair means (https://www.sheffield.ac.uk/ssid/unfair-means). This work has not been previously presented for an award at this, or any other, university. Part of this work is published in the following papers:

1. (Williams et al., 2024) Williams, D. C., Copley, R., Bugryniec, P., Dwyer-Joyce, R. & Brown, S. F. (2024) A review of ultrasonic monitoring: Assessing current approaches to li-ion battery monitoring and their relevance to thermal runaway. Journal of Power Sources, 590. https://doi.org/10.1016/j.jpowsour.2023.233777
2. (Williams et al., 2025) Williams, D. C., Green, J., Bugryniec, P., Brown, S. F. & Dwyer-Joyce, R. (2025) Battery age monitoring: Ultrasonic monitoring of ageing and degradation in lithium-ion batteries. Journal of Power Sources, 631, https://doi.org/10.1016/j.jpowsour.2025.236174
3. (Williams et al., 2026) Williams, D., Milton, R., Taylor, J., Dwyer-Joyce, R., & Brown, S. F. (2026). Acoustic Assessment of Lithium-Ion Batteries: Unravelling Temperature and Charge Contributions. Journal of Power Sources, 665. https://doi.org/10.1016/j.jpowsour.2025.238788
4. Williams, D., Milton, R., Dwyer-Joyce, R., & Brown, S. F. (2025). Acoustic Estimation of Lithium-Ion Batteries: Regression Modelling of Li-ion Battery State-of-Charge and Temperature [Manuscript submitted for publication to the Journal of Energy Storage]. School of Mechanical, Aerospace and Civil Engineering, University of Sheffield.
5. (Bugryniec et al., 2025) Bugryniec, P. J., Khanna, S., Wootton, M., Williams, D., & Brown, S. F. (2025). Assessment of the risks

posed by thermal runaway within marine Li-ion battery energy storage systems—Considering past incidents, current guidelines and future mitigation measures. Journal of Energy Storage, 128, 117070. https://doi.org/10.1016/j.est.2025.117070

Acknowledgements

I would like to first give thanks to my family, without whom this chapter of my life, and every other, would not have been possible. Your unwavering support and encouragement were crucial to me finishing this project. To my parents, I cannot thank you enough for the loving environment and opportunities for growth you provided me. To Oli and Noy, thank you for all the laughs and decompression. To Uncle Clive and Nan, thank you for always being there when I needed it. To Pop and Aunt Rose, thank you for the inspiration you gave me. I love you all in ways I cannot describe.

George, a friend who has become a brother. Throughout the years, you have taught me so much about myself and helped me become a better person. It feels that I still have much to learn from you. Thank you for being the lighthouse during the many rough storms. Here's to many more Wednesday sessions of tomfoolery.

To the Bristol folks- you guys have been paramount in me finishing this project, everything before and what will come after. The constant laughter, support, and interest (even if you didn't understand most of it) were refreshing and gave me the much needed reminder of the life that exists beyond the walls of academia. So to Abby, Aidan, Daryl, Ian, Jakub, and George, thank you. I love you guys.

I would also like to show my appreciation to Josh and Josh, one of whom is colloquially known as Wood. We may have started out as assigned friends by the university, but we stuck it out for nine years. Living together during lockdown created so many memories, and is a time I will never forget. To many more years.

Alex, a man who I voluntarily chose to live with for four years. From carrying you home on our first night of undergrad to finishing 2 degrees, you have been an incredible friend. Our many pub discussions, regardless of topic, have always been a delight, even with the introduction to beer. I eagerly look forward to seeing where the future takes you.

Many thanks to Sam, Ahranee, Gary, and everyone else in D133a, the first office that helped me get on feet during the awkward time of the Covid lockdowns. Your help and advice when I needed it cannot go understated. To Jack, Joe, and E01, the office that adopted me part way through this project with open arms. Thank you for your support as my project shifted more towards modelling and away from sanity.

I would like to thank Royce Copley and Peter Bugryniec, who both took me under their respective wings when I started out and showed me the ropes when lockdown restricted both him and me. Without your help, I would have been lost for many more months. I would also like to thank Robert Milton, who's wisdom, knowledge and willingness to help was instrumental in me getting through this project.

I would like to finish by giving thanks to of both my supervisors, Prof. Rob Dwyer-Joyce and Prof. Solomon Brown. Rob, you reaching out to me with this project, when I wasn't sure of what path I wanted to go down, was nothing short of a lifesaver. Your guidance from the very beginning was invaluable to me carving out the direction of the PhD. Sol, your support, compassion and belief in me was instrumental in me finishing this project.

Contents

List of Figures

List of Tables

Chapter 1

Introduction

In this chapter, lithium-ion batteries (LIBs) are introduced and evidence of the increased rate of adoption is provided. Attention is paid to the limitations and challenges associated with the safe usage of LIBs, and utilised methods to combat these are presented. The scope of the work is introduced.

1.1 The Expanded Use and Complexities of Lithium-Ion Batteries

A LIB is a type of secondary, or rechargeable, battery that uses the reversible intercalation of Li^+ ions, known as lithiation and delithiation (Figure 1.1). The ions travel between, and lithiate into a positive electrode (cathode) and negative electrode (anode) via an electrolyte during operation. When charging, the ions delithiate from the cathode and lithiate in the anode, and the reverse occurs during discharge. Anodes are commonly made of graphite whilst cathodes consist of lithium-metal-oxides. The electrolyte is a lithium salt in an organic solvent [1].

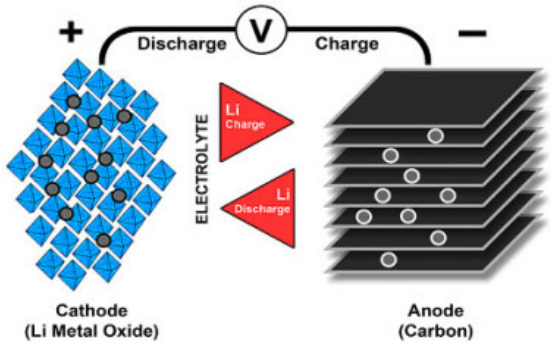

Figure 1.1: Ion Movement in a Li-ion Battery [2]

Within the last few decades, LIBs have seen a surge in popularity and application from personal electronics to the electric vehicle (EV) market and large scale energy storage [3–5]. With this increase in demand, investment in the LIB sector is expected to grow by 22% by 2030. The growth is driven, in part, by their high energy density, long cycle life, low self discharge and high power output making them an ideal energy storage device for electrical applications [6, 7].

However, there are several limitations that are associated with LIBs, including: capacity fade; current collector degradation; gas evolution and thermal runaway (TR) [8]. These limitations can damage the cells by: reducing available lithium or electrode; creating internal stress; causing short circuiting; and potentially leading the cell to catch fire or explode. Even optimal usage still results in a finite lifespan (limited charge/discharge cycles). This leads to a need for more sophisticated diagnostic systems to monitor the health and charge levels of LIBs.

There has been a growing rise in LIB sales worldwide. As of 2021, the global lithium-ion market size was $41.9 billion, and estimated to grow to $182.53 billion by 2030 [9]. Consumer electronics accounted for over 40% of the LIB market share,

with automotive applications accounting for approximately a third [10], see Figure 1.2, with rapid growth expected by the end of the decade. For example, on 19th August 2023, Tata Motors announced a plan to build a £4 billion 40 GWh battery factory in Somerset. The batteries will be manufactured for car manufactures, starting with Jaguar Land Rover in 2026 [11].

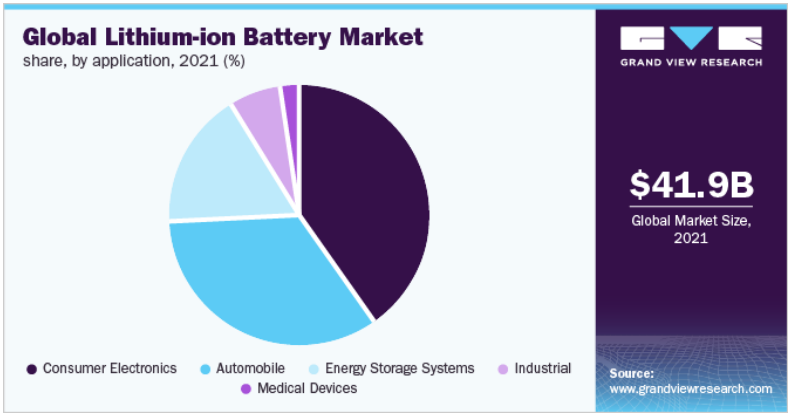

Figure 1.2: Market share of LIBs in 2021 [10].

EVs have an efficiency between 59% to 90% from grid to wheel compared to internal combustion engines at 12-30% from energy stored in the gasoline to wheels [12]. EVs also emit no exhaust pollutants, though the power plant producing the electricity may generate emissions if not renewable-based. This is important as exposure to air pollutants is the fifth leading risk factor of death in the world [13]. If the power plants utilise renewable energy, the transportation sector will be more environmentally friendly [14]. However, in order to meet 2050 Net Zero Emissions targets, the rate of growth of EV sales needs to be greater than current policies [9]. See Figure 1.3 for the expected growth of EVs between 2021 and 2030 based on global policies and what is required to reach Net Zero targets.

As the demand for LIBs grow, so too does the requirement to ensure and facilitate safe and efficient battery operation. This is highlighted by the significant number of LIB recalls as a result of explosion or fire damage, which serves to damage the reputation of LIBs [15]. LIB safety is affected by a number of factors: the battery chemistry [16]; operating environment; and abuse tolerance [17]. Abuse is what causes a cell to undergo TR, and can result in the fires and explosions causing the recalls. Battery abuse can be divided into three categories: i) mechanical abuse; ii) thermal abuse and; iii) electrical abuse [18–20]. Thermal abuse is the overheating of a cell, either from external factors or internal heat generation. Electrical abuse is due to short-circuiting, over-charging or over-discharging in the battery. Mechanical abuse is the deformation of the battery due to external forces; this could be caused by piercing or crushing the battery, causing a short circuit within the battery.

As a result of these risks, a battery management system (BMS) is implemented to control battery usage. This is done by monitoring various aspects of the battery, such as the state-of-charge (SOC) or state-of-health (SOH), and adjusting the outputs of individual cells in order to prolong life and safety. However, there are major challenges

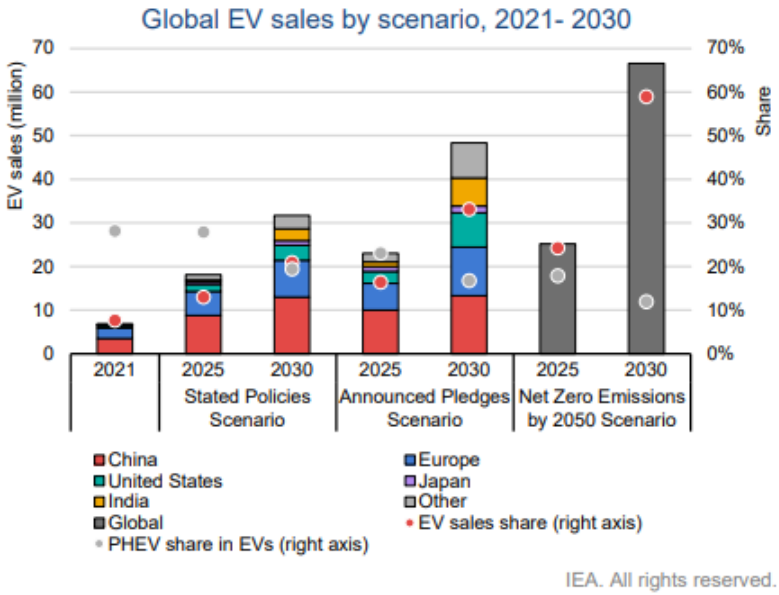

Figure 1.3: Expected EV growth based on differing scenarios [10].

monitoring a cell, as it is a closed electrochemical system. These challenges are highlighted by the readily available comments and articles discussing experiences of inconvenience and annoyance by consumers about their devices using LIBs - specifically the inaccurate estimations of battery charge and health [21–25].

As a result, development of accurate and reliable BMSs continue to be a focus [26]. These monitoring systems will become more important as EVs become more prominent and aerospace moves to battery power. This transition has already begun with Alice (see Figure 1.4), the first all-electric passenger plane having completed a flight of 8 minutes at 3500 ft (1.06 km) [27].

Figure 1.4: Alice, first all-electric passenger plane to take flight [28].

A recently proposed method of monitoring LIBs is ultrasonic monitoring. Ultrasound has been used as a non-destructive technique since the 1960s [29]. High frequency sound waves travel through a material at a velocity that is determined by the material properties. When the wave reaches an interface between two materials, such as steel-oil or steel-air, the wave splits. One part of the wave is reflected back into the original material, and another part is transmitted into the new material. The ratio of the reflected wave and the original is determined by the difference in the material properties.

This reduction in signal amplitude can be exploited to detect sub-surface parameters or defects, such as oil film measurements in journal bearings [30] and sub-surface cracks [31]. Another aspect of the wave that changes between materials is the time-of-flight (TOF). A wave might travel slower in one material compared to another due to the difference in material properties. This is the main variable exploited in this work, as it can take advantage of the movement of lithium-ions within the cell during charge and discharge, and the subsequent change in material properties in the electrodes that can then be related to the SOC and SOH.

In a 2 Ah cell, the amount of lithium that moves between layers during operation is 0.5 g. The movement causes changes in the cross sectional density distribution and elasticity of the active electrodes. Ultrasonic waves are able to detect these changes, allowing for real-time measurements of internal changes in the cell *in-situ* in a non-destructive manner. The mechanism of ultrasound is further explored in Section 2.2, and the development of the technique for lithium-ion monitoring is discussed in Section 3.1.

With the research still within its infancy, and focussing on SOC monitoring, the influence of temperature has been mostly disregarded. SOH monitoring has also received some interest, though this is not to the same extent and is not as agreed on. This thesis is focussed on addressing the lack of attention temperature has received, whilst also furthering understanding of ultrasonic-based SOH inspection.

1.2 Aims and Objectives

The aim of this project was to investigate and characterise the effects of temperature, charge and degradation on the ultrasonic measurements of lithium-ion batteries. This was to improve the accuracy of state-of-health and state-of-charge estimations for battery management systems. The objectives for this work can be summarised into three parts:

1. **Artificial ageing testing.** Adapt the ultrasonic method to detect drop in capacity in cells undergoing continuous charge and discharge cycling. Compare ultrasonic results with information from different battery parameters: voltage; current; charge; temperature. Assess ultrasonic hysteresis during degradation.

2. **Decoupling of charge and temperature effects.** Investigate the effects of temperature and state-of-charge on ultrasonic behaviour. Decouple the ultrasonic signal to isolate charge effects and temperature effects.

3. **Statistical ultrasonic estimation of charge and temperature.** Train machine learning models to estimate the temperature and state-of-charge of a LIB during standard cycling operation using the ultrasonic response.

1.3 Thesis Layout

The layout of this thesis is as follows:

Chapter 2 provides background knowledge to the main concepts - batteries and ultrasound. Battery operation is described, discussing the working mechanics of material transportation during operation, as this is the process that allows for ultrasonic monitoring. The ultrasound section explains the concepts presented in this work. Sensor options and bonding methods are briefly described.

Chapter 3 presents a literature review which is split into three sections. Firstly, a comprehensive review of ultrasonic monitoring of lithium-ion batteries, covering the history and scope of the field. Secondly, a thorough review of abuse monitoring of lithium-ion batteries, exploring the behaviour of batteries when heated, overcharged or mechanically damaged. Thirdly, a look into the ultrasonic monitoring of lithium-ion batteries during abuse condition testing, covering the potential scope and opportunities of this new area of research.

Chapter 4 provides an introduction to each publication in this work, presenting the publication information so that the contribution from each co-author is clearly stated. All the publications presented in this thesis focus on the application of ultrasonic monitoring of LIBs.

Chapter 5 concludes the thesis with a summary of the research, solidifying the importance of the research before describing the future work this thesis has led to.

Chapter 6 to **Chapter 8** present each publication in full.

Chapter 2

Background

In this chapter the two main aspects of this work are described. Firstly, Section 2.1 introduces batteries, specifically battery operation and the mechanics of their operation. Safe operating conditions for battery operation are presented, looking at what factors are monitored to prevent unsafe operation. Battery management systems are introduced, with a focus on the SOC estimation methods. Section 2.2 defines the theory of ultrasonic waves and how they travel through a medium, with a focus on multi media boundary layer interactions. Concepts such as frequency, reflection coefficient and how these relate to wave propagation are discussed. Transducer instrumentation arrangements are outlined.

2.1 Batteries

2.1.1 Li-ion Battery Operation

LIBs are primarily used due to their high energy density, high power density and long cycle life compared to other common battery types [32, 33]. A comparison of the energy density to power density of various secondary cell chemistries is shown in Figure 2.1, where the lithium type batteries have the highest gravimetric (Wh/kg) and volumetric (Wh/m^3) energy densities of the shown battery material types.

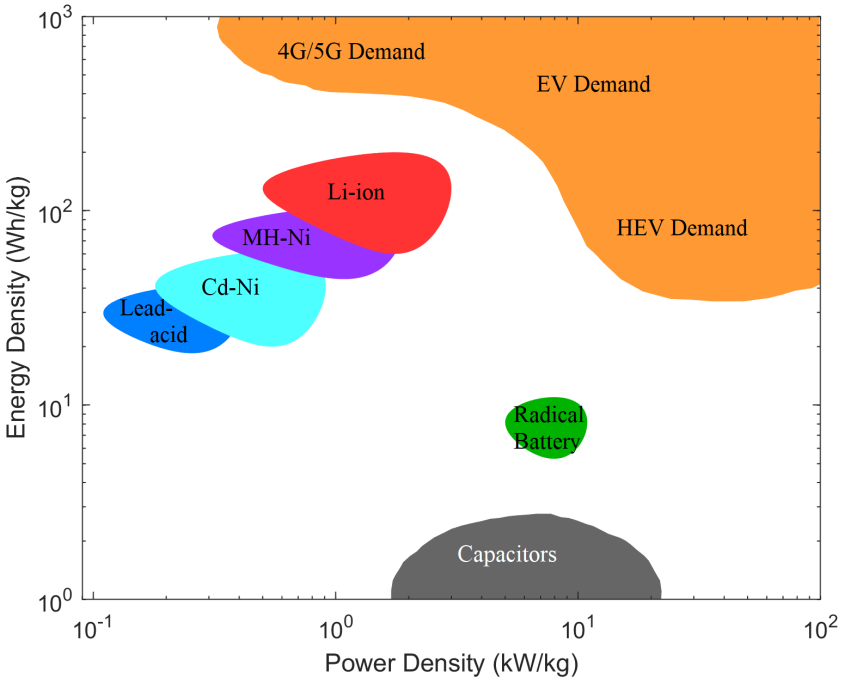

Figure 2.1: Comparison of energy density to power density in various secondary cell chemistries, reproduced from [34].

There are various cathode materials that LIBs can utilise such as NMC (lithium-nickel-manganese-cobalt-oxide), NCA (lithium-nickel-cobalt-aluminium-oxide), and

LFP (lithium-iron-phosphate). LIBs can also have different electrolytes, material structures and cell construction [35]. The combinations of these materials affect various battery properties, such as energy density, life cycle, specific power, and safety.

One major restriction with LIBs is the small range for safe operation - for both voltage and temperature - restricting use in more variable climates and work conditions. For voltage, the safe operating range is between 1.5 - 4.2V, depending on the cathode material. The safe operating temperatures can range from 0 to 45°C and from -20 to 55°C when charging and discharging, respectively [32]. When the battery reaches a temperature of 90°C, the solid electrolyte interface (SEI) begins to break down. The SEI has two important roles: i) protection against graphite co-intercalating with electrolyte solvent molecules and; ii) prevention of Li-ions consumption [36]. At higher temperatures, the SEI film is unable to prevent lithiated anode-electrolyte reactions, generating gases [37].

There are multiple reasons for the complexity in estimating the SOC: the maximum possible capacity, Q_{max}, decreasing throughout the lifespan of the battery; the capacity being affected by the ambient temperature and age of the battery [38]; and the requirements of parameters such as the initial SOC and impedance [39]. BMS based on different theories have been developed to monitor and calculate the SOC of a LIB. The use of different methods, within the limitations of available knowledge and hardware, aim to combat the above difficulties. The structure of BMSs are discussed in the following section.

2.1.2 Battery Abuse

Battery abuse can be categorised into three main groups: mechanical abuse, electrical abuse and thermal abuse [37, 40]. Along with latent defects inside the battery such as burrs, material impurities and electrode deflection [41], these abuse mechanics can lead to TR, resulting in battery failure, smoke off-gassing, and fire or explosion [42]. In order to reduce the risk of TR, the SOC of a cell is monitored; preventing the cell from over- or under-charging thus reducing the risk of electrical abuse. The SOC is defined as the percentage of the maximum possible charge remaining in the battery [43] where 100% SOC is fully charged and 0% is fully discharged. Although this definition is straightforward, calculating the SOC is complex.

Over-charging can cause lithium dendrite formation and growth [44], which can pierce the separator. This can lead to the battery short-circuiting, causing a positive feedback loop in temperature increase leading to TR. At lower temperatures, the cathode can undergo short circuiting. When the minimum voltage drops below 1.5V, when the first derivative of the voltage is 0, the copper in the current collector foil begins to oxidise followed by the dissolution of the copper after the cathode breaks down [45]. The dissolution can lead to capacity loss, as well as the deposition of the copper on the anode, cathode and cathode-facing separator surfaces. [46, 47].

2.1.3 Battery Management Systems

A BMS is a system that monitors the states and parameters of the battery pack, which include cell voltage, current, temperature; as well as calculate the SOC and SOH of the pack [48]. The BMS uses these parameters as inputs to determine, amongst other operational criteria, when to limit (dis)charging and to shut down operation of the battery to prevent it being damaged or undergoing TR.

According to How et al. [49], there are two established categories and three relatively new categories for classifying SOC estimation methods, as shown in Figure 2.2. The two established methods are: model-based estimation using electrical data, chemical data or a combination of those properties for individual batteries, based on the porous electrode theory [50] and; data-driven estimation measuring the change in battery parameters. The three new categories are: lookup table estimation which exploits the direct mapping relationship between SOC and external characteristics, such as open-circuit voltage; coulomb counting estimation that measures and integrates the discharging current over time; and a hybrid method using a combination of usually two or three algorithms.

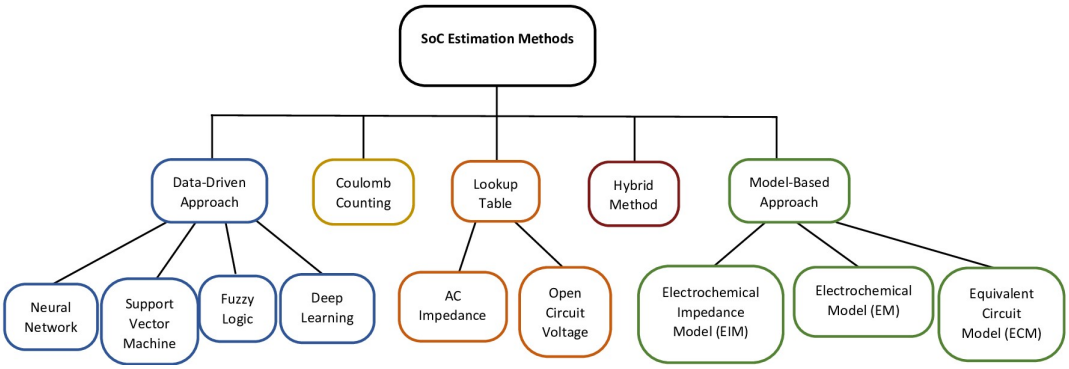

Figure 2.2: Classification of state-of-charge estimation methods, adopted from [49].

There are other ways of classifying BMS estimation methods. One such classification, defined by Berecibar et al., employs two categories: experimental techniques and adaptive models [51], as shown in Table 2.1. Experimental techniques compare cycling data history of an active battery to that of previous batteries, to extract SOH estimations. This is limited by cell chemistry, design and operating conditions, reducing the transferability of the knowledge across multiple batteries. This approach also requires an understanding of the relation between degradation and operation, obtained by evaluation of large data sets or physical analysis of the cell. These arguments form the basis of the author's determination that experimental methods are not suitable for in-situ estimation. For example, when using Coulomb counting, an accurate initial SOC is needed and it is vulnerable to estimation accumulation. The open-circuit voltage (OCV) estimation method requires the battery to be disconnected from any load and rested long enough for the battery to have relaxed from the load [52]. This is less of an issue for batteries that are not under constant use, such as EVs which are used for a few hours per day and are later charged within some hours [53].

Table 2.1: Benefits and drawbacks of the established state-of-charge estimation methods, reproduced from [51].

	Experimental Techniques	Adaptive Methods
Based on	Storing the lifetime data and the use of the previous knowledge of the operation performance of the cell/battery.	Calculation of the parameters, which are sensitive to the degradation in a cell/battery.
Advantages	1. Low computational effort 2. Possible implementation in a BMS	1. High accuracy 2. Possible to be used as in-situ estimation
Disadvantages	1. Low accuracy 2. Not suited for in-situ estimation	1. High computational effort 2. Difficult in BMSs implementation

Adaptive models can quantify degradation based on parameters that are affected by said degradation. The parameters must be measurable or should be examined in the cell throughout the cell operation. This reduces the number of tests required to accurately monitor the cell, as well as allow greater adaptability across different cell chemistries and form factors [32]. There exists a trade-off between accuracy and computational power. The most accurate methods for experimental techniques are impedance measurement and sample entropy. However coulomb counting and the probabilistic methods are the most common due to their simplicity.

Many BMS estimation methods have an estimation error in the range of >1% - 12%, with the most common being reported between 5% - 10%. There are some simple methods that can provide accurate results such as Coulomb counting [54] and open circuit voltage (OCV) methods [55]. However, these low error ranges are obtained if the battery is in a stable state and with a low variance of battery parameters. For accurate measurements in unstable states, more complex methods are required [56] Some complex models include: Kalman filtering [57]; particle filtering [58]; and Gaussian process functional regression [59].

Sophisticated estimation methods have been recently developed using neural networks, due to the limited improvement provided by simple BMSs. Multiple safety incidents in LIBs have occurred when simple BMSs have been used, and the lifespan of a battery pack is noticeably less than an individual cell [60]. More sophisticated BMSs provide better protection against over-charge and over-discharge, improving lifespan and safe usage of batteries.

2.2 Ultrasound

Sound is an pressure – or acoustic – wave that travels through a medium. Ultrasound is defined as a sound wave with a frequency above human hearing, generally regarded as above 20 kHz [61]. Ultrasound waves are non-invasive and non-destructive. The waves travel through a medium with minor, non-permanent changes on a particle level without the need for instrumentation inside a body, allowing for *in-situ* and *in-operando* monitoring. The propagation of ultrasound is dependent on the medium it is travelling through. Solids can support the propagation of longitudinal (pressure) and shear (elastic) waves, whilst fluids - liquids and gases - can only support longitudinal waves as they lack shear strength. Figure 2.3 illustrates these wave propagation modes.

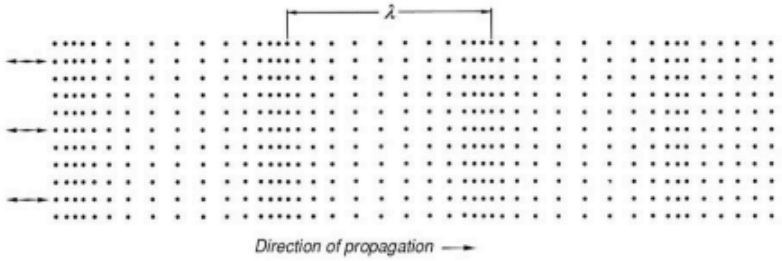

(a) Longitudinal

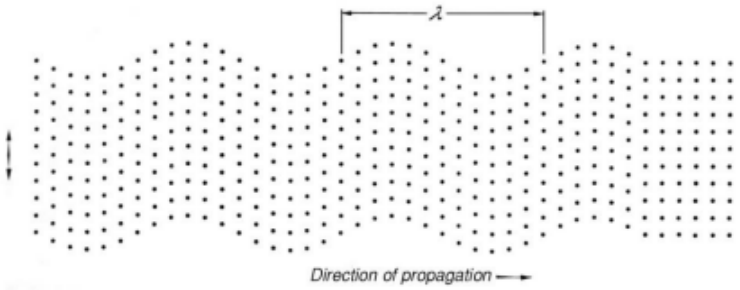

(b) Shear

Figure 2.3: Modes of wave propagation [61].

2.2.1 Ultrasonic Wave Properties

A sound wave has three properties: wavelength, frequency and amplitude. Frequency describes the number of oscillations per second of a wave and is measured in Hertz (Hz). Wavelength describes the distance between two points on a wave that are in the same state, such as two peaks or two valleys, and is measured in metres (m). Amplitude describes the pressure or displacement caused by the acoustic wave, and can be measured in Pascals (Pa) or metres (m), depending on the wave type. When measured using piezoelectric transducers, the amplitude is usually measured in volts (V) as a proxy. Frequency and wavelength are inversely proportional, and are defined in Equation 2.1.

$$c = f\lambda \tag{2.1}$$

where - c = speed of sound of a medium (m s^{-1}), - f = frequency (Hz), - λ is the wavelength (µm). The wave speed is dependent on the material properties of the host medium; it is determined by the elastic forces between the particles. The wave will travel at different speeds in different media. The longitudinal wave speed through a solid and fluid (liquid or gas) can be calculated using Equations 2.2 and 2.3, respectively:

$$c_l = \sqrt{\frac{K + \frac{4}{3}G}{\rho}} \tag{2.2}$$

$$c_l = \sqrt{\frac{K}{\rho}} \tag{2.3}$$

whilst the the shear wave speed through a solid can be calculated using:

$$c_s = \sqrt{\frac{G}{\rho}} \tag{2.4}$$

where - B = Bulk modulus (GPa), - ρ = Density (kg m^{-3}) - G = Shear modulus (GPa). A fluid cannot host a shear wave as fluids do not exhibit shear strength. If the speed of sound through a material is known, the thickness of a material or the depth of a discontinuity in a material can be calculated based on the relationship between distance, speed and time. This is known as the time-of-flight (ToF) method, which is the basis of multiple ultrasonic measurement gauges available on the market.

Temperature is also known to influence the speed of sound through a medium. In metals such as steel, a higher temperature will cause the speed of sound to decrease, resulting in a longer TOF for both shear and longitudinal waves. This was due to a decrease in the bulk and shear modulus of steel as a result of the increase in temperature [62]. The density will also decrease due to thermal expansion of steel [63]. This behaviour is not universal across media. In water at atmospheric pressure, the speed of sound increases between 0 °C and 100 °C [64]. This is a result of B increasing with temperature [65]. The speed of sound also increases with an increase in pressure. Similarly to steel, the density of water also sees a decrease with an increase in temperature [64]. Interestingly, when frozen as ice, the speed of sound decreases as temperature increases [66]. This is due to a decrease in bulk modulus [67] and shear modulus [68] as temperature increases. Density also slightly decreases as temperature increases [69].

2.2.2 Attenuation and Reflections

Ultrasonic testing is a well established method of monitoring solid bodies through the use of high-frequency sound waves, and is very sensitive to surface and subsurface discontinuities. Sound is a vibration that propagates as an acoustic wave through a host

medium. When travelling through a medium, the wave amplitude - the displacement of the particles in the host medium caused by the acoustic wave - decreases which is called attenuation. Attenuation is the reduction in magnitude of acoustic energy as a wave travels through a medium, and has consists of multiple processes: absorption; scattering and refraction. For a homogeneous, one-dimensional medium, attenuation defined in Equation 2.5:

$$Attenuation = \alpha l f \tag{2.5}$$

where l is the length of the material (m) and α is the attenuation coefficient (dB cm^{-1} Hz^{-1}). Attenuation therefore increases with signal frequency, as well as the travel path and the attenuation coefficient of the medium. As such, for longer samples, a lower frequency signal is preferred. Lower frequencies are also preferred for multi-layered samples, which is discussed later in this section.

The main mechanisms of attenuation are absorption, scattering, and refraction. Absorption is the conversion of acoustic energy into thermal energy within a medium [70]. For a single medium, scattering occurs as materials are not ideal, resulting in discontinuities; micro-cracks in the material and variance in grain sizes. These discontinuities introduce boundaries that cause reflections of the wave due to differences in acoustic impedances in the material. The proportion of the wave that is scattered within a single medium is determined by the wavelength of the signal, grain size and anisotropy [71–73].

Scattering can also occur between two media, such as a crack in a steel block or an iron plate in contact with a copper plate. It does not matter if the media are ideal or not. This form of scattering involves the reflection back into the original medium or the transmission (absorption) into the new medium. The difference in acoustic impedances between the two media determines the ratio of the wave that is reflected to transmitted. An example of this is presented in Figure 2.4. This allows for real-time monitoring of material properties, flaw detection and evaluation, and changes in material dimensions [61].

Refraction occurs when the acoustic wave approaches an interface between two differing media. The difference in material properties will cause the wave to change when it reaches the new medium. This change in acoustic velocity causes the wave to 'bend' [72].

The acoustic impedance z (Pa s m^{-3}) of a material is the ratio of acoustic pressure within a medium to the velocity of the particles. It is defined as the product of the material density and the sound wave velocity:

$$z = \rho c \tag{2.6}$$

When an ultrasonic wave reaches an interface between two media, some of the wave is reflected and part is transmitted into the new medium. The proportion of the wave reflected at the interface is called the reflection coefficient, R. The reflection coefficient is defined using the acoustic impedances of the two materials, given in Equation 2.7:

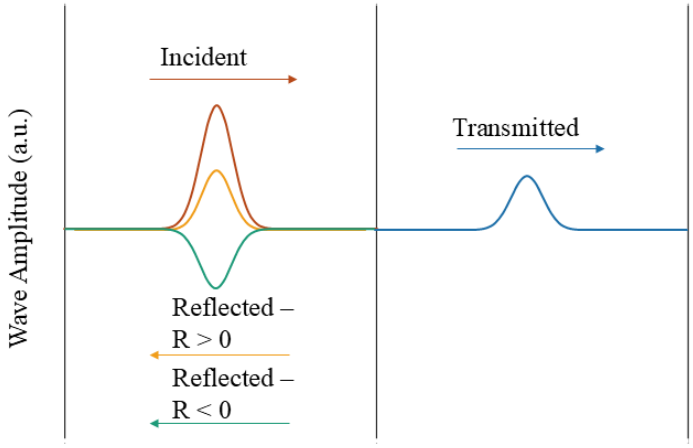

Figure 2.4: Example of a two-layered body of different media, where a wave encounters an interface. At the interface, part of the wave is reflected into the original medium and part is transmitted into the new medium. The phase of the reflected signal is dependent on the polarity of the reflection coefficient. The amplitude of the transmitted is dependent on the absolute value of R.

$$R = \frac{z_2 - z_1}{z_2 + z_1} \tag{2.7}$$

where z_1 and z_2 are the acoustic impedances of the primary and secondary material [74]. As Equation 2.7 shows, the materials with similar acoustic impedances will transmit a larger proportion of the wave compared to materials that have differing acoustic impedances, such as air and steel.

The difference in acoustic impedances also affects the phase of the reflected signal. If R is positive, corresponding to $z_2 > z_1$, the reflected wave remains in phase with the incident wave. If R is negative, corresponding to $z_2 < z_1$, the reflected wave undergoes a phase inversion of π relative to the incident wave [75]. This behaviour is illustrated in Figure 2.4 where the orange waveform represents a positive R reflected wave, and the green represents a negative R reflected wave. The amplitude of the reflected and transmitted signal is also dependent on R; a larger absolute value of R, the greater the reflected amplitude will be, and a corresponding reduction in the transmitted amplitude.

2.2.3 Near and Far Fields

From an ideal point source of acoustic energy, the wave will propagate equally in all directions in a spherical wave front [76]. When generated from a transducer, an ultrasonic wave will propagate from the entire active face. The resultant wave interference will cause signal amplitude fluctuations because of constructive and destructive interference from the multiple generated waves. As the wave propagates, the wave will stabilise. The travel path before this stabilisation is called the near field distance, and data taken within this distance can be problematic [72]. The near field

can be calculated from Equation 2.8.

$$N = \frac{kD^2 f}{4c} \tag{2.8}$$

where D is the diameter of the transducer, f is the frequency, c is the speed of sound, and k is the aspect ratio constant for use with non-circular elements [61]. The distance after the near field is called the far field.

2.2.4 Pulsing and Wave Paths

A sound wave can be produced by a piezoelectric transducer, which generates ultrasonic waves - when subjected to an electrical current - and injects them into the sample. This is a common method of wave generation for ultrasonic testing. There are two main inspection modes for ultrasonic testing: pulse-echo and pitch-catch [77, 78].

The pulse-echo mode is a one transducer setup in which the transducer emits and receives the ultrasonic signal in order to investigate the reflections from discontinuities or boundaries. The pitch-catch mode is a multi-transducer setup in which two transducers are mounted on the material. One transducer acts as the emitter, whilst the other acts as the receiver. The transducers are usually placed on the same face. To ensure the receiving sensor detects the wave, the pulse is emitted at an angle. The transducers can also be located directly opposite one another, referred to as the through-pulse mode. This setup is useful for cylindrical pipes as it increases confidence of discontinuity detection, as the wave has travelled through the pipe's diameter. See Figure 2.5 for a visualisation of the three modes. Such modes can be used for SOC and SOH monitoring in LIBs, as the movement of Li-ions will change the material properties of the electrodes, thereby changing the acoustic signal. This is further explored in Section 2.2.5.

2.2.5 Ultrasonic Setup and Battery Hardware

Ultrasonic monitoring of LIBs is a non-destructive method which allows for *in-situ* testing. For the purpose of this thesis, the hardware required for ultrasonic testing consists of a piezoelectric transducer either directly bonded to the cell or held in contact with the cell in a casing, which is called a contact probe. If bonded directly, a thin layer of adhesive is used to secure the transducer to the cell. If within a housing, a thin layer of ultrasonic gel is applied between the cell surface and the transducer in order to improve the coupling between the transducer and cell [79]. Common transducers include piezoelectric ceramic transducers and capacitive micro-machined ultrasonic transducers.

As stated in Section 2.2.4, the most common modes are pitch-catch and pulse-echo. This is performed with either a contact probe, or with directly bonded piezoelectric elements. These are usually used to monitor changes in the SOC during non-abusive cycling, as well as cell degradation during both abusive and non-abusive cycling. Other arrangements have been used to monitor LIBs, such as an air coupled setup [80]. Air coupled methods involve a through-pulse mode where the elements are not in contact

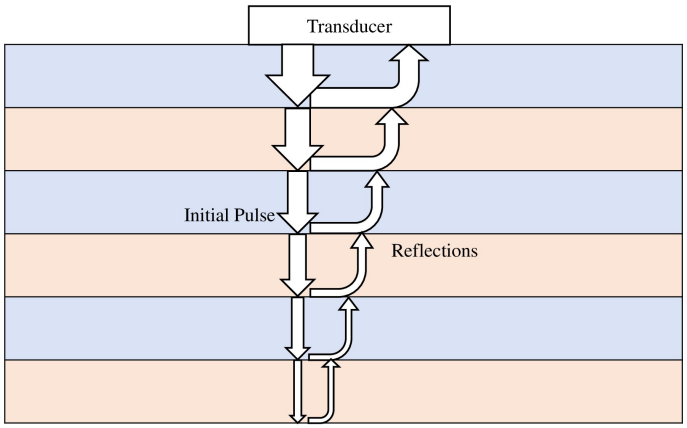

(a) Pulse-echo.

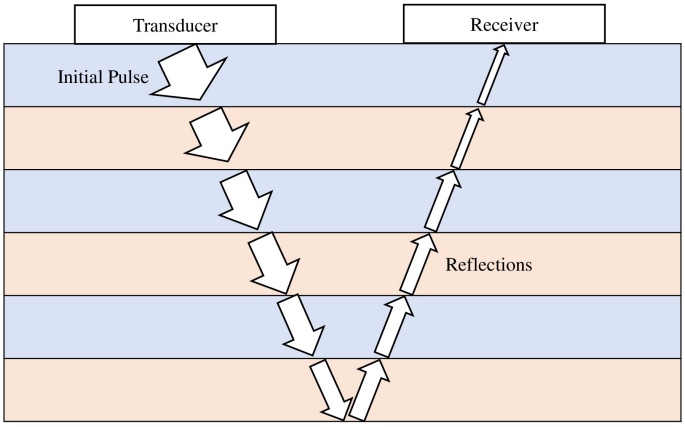

(b) Pitch-catch.

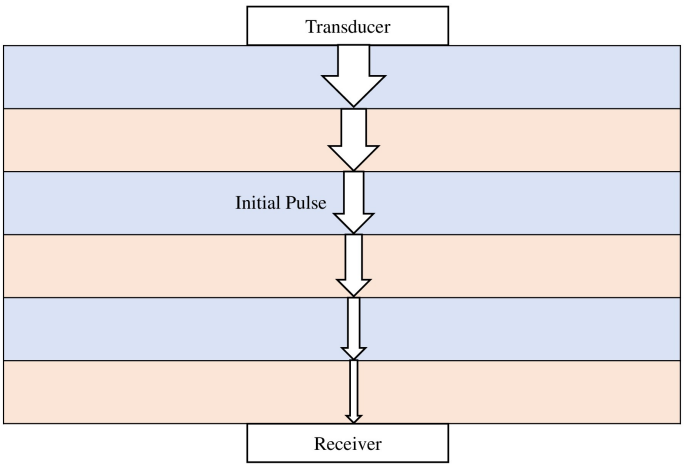

(c) Through-pulse.

Figure 2.5: Sketch of how acoustic signals travel through a multi-layered body via the a) pulse-echo mode, b) pitch-catch mode and c) through-pulse mode. The sketches show a single interaction at each interface, where the signal is part transmitted and part reflected. However, this will occur multiple times for a) and b), resulting in a complex signal of multiple reflections.

with the sample; the wave will propagate through the air before and after propagating through the cell.

In literature there has been a range of frequencies tested, from 200kHz to 5MHz; laboratory use-cases tend to higher frequencies and closer-to-application uses tend to lower frequencies [81–85]. The frequency of the wave is limited by the sampling frequency of the data acquisition system and the penetration depth of the acoustic wave [86], where the resolution refers to the timing between the discrete measurements used to describe the reflection signals. For example, a resolution of 12.8ns for a measurement of 6µs, will result in 495 discrete measurements.

The penetration refers to how deep into the sample the ultrasonic wave can propagate before it fully attenuates. At each medium interface, part of the wave is reflected, part is transmitted and part is absorbed. The frequency has an effect on the penetration depth of a wave; a higher frequency will have a higher sensitivity compared to lower frequencies sensitivity, but also attenuate at a faster rate, reducing the depth of penetration. Finding a compromise between sensitivity and penetration is important to gain the most information from the test whilst having adequate depth of penetration. The information is collected from an amplitude scan (Ascan). An AScan shows the change in amplitude of the signal over time. A high amplitude signal relates to a strong reflection, and a low amplitude signal relates to a weak reflection.

If a pulse-echo mode is used, the AScan will consist of the generated pulse and the reflections, as shown in Figure 2.6. The peaks between the generated pulse and the first reflection is due to ringing from the generated pulse. A pitch-catch or through-pulse will not have the generated pulse visible in the AScan. A reflection refers to the acoustic energy exciting the receiving transducer. The number of peaks do not correlate to the number of layers; a peak is not representative of a single layer, but the culmination of many reflections from within the cell, see Figure 2.5.

When utilising the through-pulse mode, the received signal ensures all active layers of the battery have been monitored - the signal will not otherwise be received. A full battery diagnosis and charge monitor of the battery is therefore possible. However, a more complex system is required for operation. In contrast, the pulse-echo and pitch-catch modes do not ensure full battery diagnosis, as the penetration depth of the signal can not be confirmed. This could call into question the bias of the signal between temperature and charge [7]. The number of peaks do not correlate to the number of layers; a peak is not representative of a single layer, but the culmination of many reflections from within the cell, see Figure 2.5.

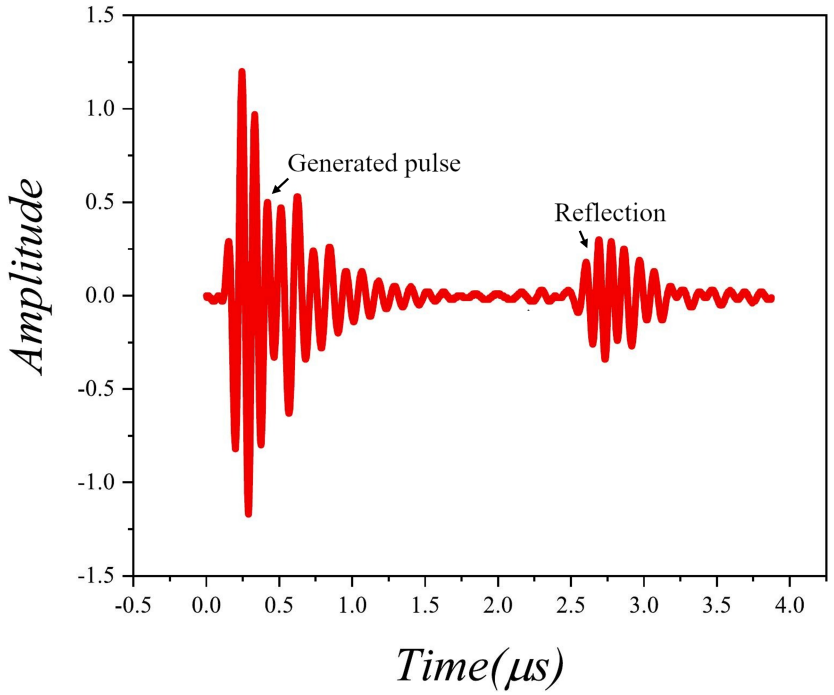

Figure 2.6: Example AScan from a pulse-echo ultrasonic setup. The first region of interest is the initial signal generated by exciting the transducer, and the second region is the received signal after propagating through the cell and reflecting off the back wall [87].

2.3 Conclusions

- The speed of sound in a medium is dependent on the medium's material properties. For a constant speed of sound through a medium, a higher frequency wave results in a shorter wavelength.
- A boundary layer occurs when two adjacent layers have differing material properties. When an acoustic wave interacts with a boundary layer, the wave splits. Part of the wave is transmitted into the new medium and part is reflected back into the original medium. An increase of number of boundary layers can complicate the signal and reduce the signal amplitude.
- Lithium-ion cells can use different chemical setups for the cathode, which effect the cell properties. Lithium-ion cells have a safe operating window for temperature and voltage. Outside of this window, the cell can undergo degradation. Cells can undergo thermal runaway if abused mechanically, chemically and/or thermally.
- There are various methods for monitoring lithium-ion cells via battery-management systems. These methods monitor external variables such as voltage, current and temperature. Some of these methods are experimental in nature and others are model-based.

Chapter 3

Literature Review

The aim of this chapter is to review current literature on ultrasonic monitoring of LIBs, discuss the advantages and flaws of current techniques and make recommendations to enable the practical application of LIB monitoring. To do so, the chapter is split into three sections. Section 3.1 focuses on the current use of ultrasonic for SOC and SOH and its applicability to the detection of thermal runaway; section 3.2 focuses abuse mechanisms of thermal runaway in LIBs and how the chemistry and charge and charge rate have an effect; and Section 3.3 takes a look at the application of ultrasonic to monitor abuse conditions of LIBs. Section 3.4 compiles the references used in this chapter, providing a brief summary of the experimental setup and results. The chapter concludes with Section 3.5, outlining recommendations on what needs to be addressed - and how to address these aspects - in order to improve viability of ultrasonic monitoring of LIBs in practical applications.

3.1 Ultrasonic Monitoring of State-of-Charge and State-of-Health in Li-ion Batteries

The SOC and the SOH can be measured by the change in voltage, charge, and temperature of the cell as stated in Section 2.1.3. Voltage and charge data provide electrochemical insight into the cell; however, it does not provide the greatest accuracy for the SOC of the cell. The parameters used are measured outside the cell; they are the outputs of the change in SOC. Temperature data provides limited insight into the state of safety (SOS) of the cell, and therefore of the potential of thermal runaway [88]. Temperature does not provide SOC information by itself however.

US has been implemented to provide insight into the SOC and SOH of LIBs. The SOC is measurable due to density and stiffness changes within the electrodes due to lithium intercalation/deintercalation [89]. This results in a speed of sound change in the electrodes, see Equation 2.3. The ToF will be affected by the change in speed of sound, allowing the SOC to be monitored [82]. As this method is based on internal changes to the cell, US can provide a different perspective to conventional BMSs. Combining these methods could create a more complete view of the cell/pack in question and improve the accuracy of the estimation.

Cell degradation is measurable due to the gas generation, electrode expansion, residual stress development or electrode ruffling/delamination. As these modes appear and progress, the cell will swell. This increases the distance the US wave must travel, resulting in a change in ToF. The US wave will also attenuate at a greater rate in an older battery as a result of these modes: gas will create more interfaces within the cell that have high reflection coefficients; electrode ruffling/delamination leads to less contact between the electrodes, reducing the transmissibility of the wave. These result in a weaker signal [81].

3.1.1 SOC Monitoring

The method used to infer SOC in LIBs via US is based on the principle that the movement of Li-ions during charge/discharge leads to a change in density, and in

turn the acoustic impedance, of the electrodes. As described in Equation 2.7, the proportion of the signal that is reflected will therefore vary during operation. The distribution of Li-ions, along with the rate of change of the distribution, could provide insight in to the SOH. The cell chemistry will not have an effect on the adaptability of this method as the movement of the ions is integral to the operation of the cells.

The first paper showing the application of US ToF to monitor the SOC and SOH of batteries was written by Hsieh et al. in 2015 [82]. In this paper, two 2.25 MHz sensors were placed in a through-pulse setup. The cells were $LiCoO_2$/graphite prismatic pouch cells. Alongside this, the pulsing sensor listening for the response, in a pulse-echo setup. It was found that the ToF peak shifts towards lower values and the signal increased in intensity during charging. The opposite was true for discharging; the ToF shift would tend towards higher values and the signal intensity would decrease.

Gold et al. [83] used US testing to validate the determination of SOC based on volumetric expansion of the graphite. It was found that 200 kHz was the most favourable and allowed for easy discrimination between charged and discharged states. This difference can be seen in Figure 3.1. It was found that the second reflection has a ToF shift of ∼30 µs between charged and discharged. The signal amplitude demonstrated a relation to the SOC; the first reflection was largely unaffected by the change in SOC, but the second reflection showed a linear reduction in amplitude of 14.08±0.61% as the cell was discharged. The authors concluded that the SOC can be determined without a reference electrode. Therefore, the SOC of LIBs could be estimated using the direct US method in real-use cases.

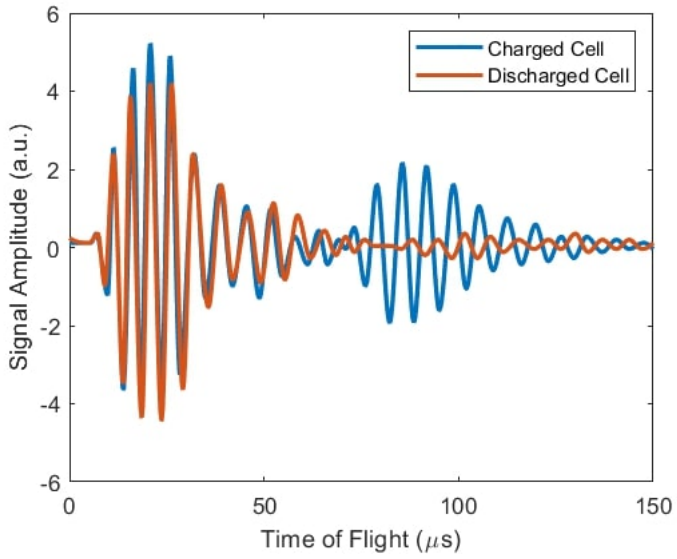

Figure 3.1: AScan of 200 kHz pulse through a cell at fully charged and fully discharged states. Recreated from [83].

It was unknown from Gold's research what dependencies the US signal had when estimating the SOC. To address this, Popp et al. [90] investigated the effects of C-rate and temperature on the measured ToF. They found that the C-rate produced uncer-

tainties in the ToF measurements, with higher C-rates resulting in longer ToF and less pronounced local minima. This behaviour was possibly influenced by inhomogeneity in the Li-ion distribution in the electrodes [91]. Higher temperatures resulted in a higher ToF, due to the decreased stiffness of the cell at higher temperature, and thus a lower wave propagation speed. As expected, the ToF also varied with the SOC, as at 25 °C, the change in ToF between charged and discharged was 10 μs.

The literature described used longitudinal US waves; there are multiple types of US propagation types. One of these types is surface - or Rayleigh - waves, which was investigated by Ladpli et al. [92]. It was found that they were able to estimate the SOH and SOC with error less than 0.05% and 0.36%, respectively. Surface waves differ from other US waves as they travel across the surface of a medium, rather than penetrating into the medium. The penetration of surface waves is dependent on the wavelength [93], thereby reducing the ability to monitor changes in the electrode layers deeper within the cell.

A non-contact method was tested, where the 400 kHz sensors were situated 40 mm from the cell, suspended in the air. The SOC estimation was possible even with the low signal-to-noise ratio present in the test. A near linear relationship was also stated to exist between the amplitudes of both the longitudinal wave and the SOC , which aligns with other reports [80].

Copley et al. [7] studied the qualities in a signal passing through the different layers of a LIB. A model was developed to understand the features and nature of the US signal, and validated against a repeat experiment of Hsieh et al. [82]. The model indicated that small changes to the electrode properties, such as density and elastic modulus, could have a significant effect on the US signal. ToF shift had a stable correlation with the charge state of the cell, whereas the amplitude was found to be unstable. Figure 3.2 shows that the ToF correlation is consistent for both charge and discharge, but the amplitude varies between the two states. Frequency was suspected to have an effect on signal reliability; if the wave has weak penetrating power, then the signal is dominated by layers close to the sensor and are susceptible to temperature bias.

Multiple chemistries have been tested, including LCO and LFP [94]. LFP cells were shown to have a lower SOC estimation error, of 1%, compared to LCO, of 2.3 to 3%, when using ToF and signal amplitude. This was an improvement over using voltage measurements; LFP had an error of 6% and LCO had an error of 3%. This suggests that the cathode chemistry has an effect of the reliability of US monitoring. The authors did not provide a suggestion as to why there is a difference in accuracy. A possible explanation for this could be the change in cathode mechanical properties during battery operation. As defined in Equations 2.2 and 2.7, the bulk modulus, shear modulus, and density of the cathodes will affect the speed of sound and attenuation of the signal. A smaller change in elastic modulus will result in a smaller change in speed of sound resulting in a smaller ΔToF available to use for SOC estimation. Further testing is required to determine this discrepancy.

Table 3.1 summarises the research and respective findings in this subsection.

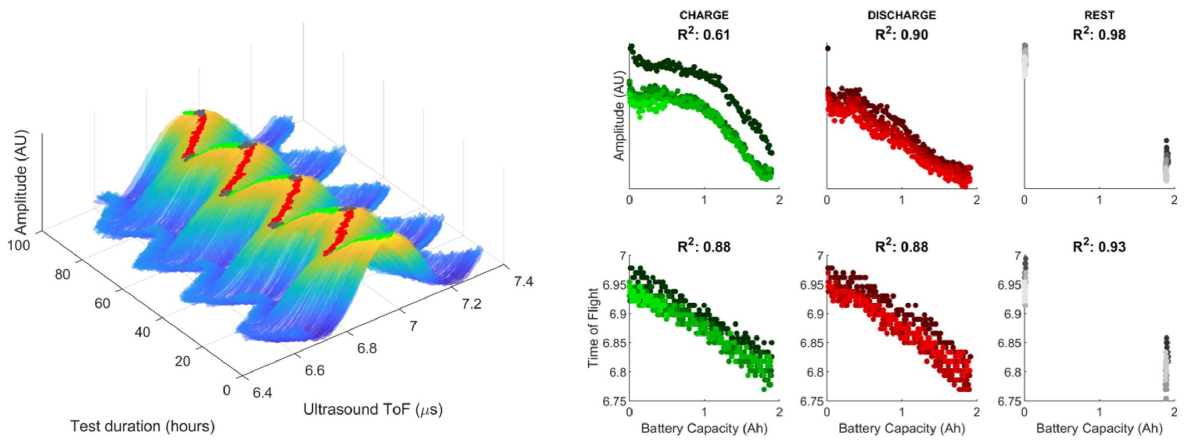

(a) (b)

Figure 3.2: a) Graphical peak evolution throughout a charging test b) the correlation plots of the charge states with amplitude and ToF [7].

3.1.2 SOH Monitoring

Sood et al. [81] used two 5 MHz transducers in a pitch-catch mode and cycled the cells to investigate signs of cell degradation. The ultrasonic response was used to monitor swelling, electrode expansion, electrode ruffling, delamination and voiding within a LIB. The LIB was put through numerous charge cycles, and a change in the AScan signal was detected. The weakened signal was concluded to be from degradation, though the cause of said degradation was not determined. The cause of the degradation was suspected to be gas evolution, residual stress on the interfaces or electrode expansion.

Rather than looking at detecting degradation methods, Ladpli et al. [95] used guided-wave-based US waves to monitor the change in ToF during artificial ageing of LIBs using bonded piezoelectric transducers. The results, shown in Figure 3.3 a, demonstrate a decrease in ToF as a battery ages. This contradicts the results found by Wu et al. [96] (see Figure 3.3 b) where it was found that the deviation of the increased ToF becomes more prominent as the cell ages. The cause of this increased ToF is a result of the density changes of the electrodes, as the Li-ion content in each electrode changes as the cell charges and discharges. A Spearman coefficient greater than 0.94 was calculated showing a high correlation between ToF and SOH [96]. In the over-charge test, Wu et al. found that the ToF increased sharply after some time (2.8 hours). The authors suggested the over-charging caused internal gas generation, which resulted in cell expansion.

Oca et al. [97] studied Li-ion capacitors abused by mild over- and under-charge. The capacitors were rated to 2.2 - 3.8 V, with the mild under-charge/over-charge defined as 2.0 V and 4.5 V, respectively. They found ToF can be used to detect permanent changes that may not be seen from voltage alone. They state that ToF is a good indicator of swelling, initiated during discharge over the first mild over-charge, which agrees Wu et al. [96]. However, they were unable to determine whether the ToF change was due to change in the electrode material or gas generation.

Aim	Diagnosis	Transducer Setup	Reference
Through-pulse measurements of SOC and SOH using ToF	ToF had an inverse linear relationship with SOC	2.25 MHz contact probe	[82]
		200 kHz Bonded transducer	[83]
	Linear relation between signal amplitude and SOC	125 kHz Air-coupled through-pulse	[80]
C-rate and temperature effects on ToF	Relationship between increased C-rate and ToF and temperature and ToF	25-40 kHz surface waves	[90]
Through-pulse measurements of SOC and SOH using ToF	Low error estimation of SOC and SOH, despite shallow penetration	Surface-wave pitch-catch	[92]
Model ToF changes based on electrode property changes	ToF has consistent correlation with SOC	Model	[7]

Table 3.1: Table of SOC diagnosis using ultrasound.

Bommier et al. [98] studied SEI formation within NMC - Si/graphite cells as well as long-term cycling effects. The cells were instrumented with two 2.25 MHz transducers in a through-pulse mode. It was found that the onset of gassing - suggested to be caused by the initial formation of the SEI - was detected by a loss in acoustic signal. This was only present in cells with Si/graphite anodes [82]. As the cell was cycled and the capacity drop increased, an upward ToF trend was found.

Robinson et al. [99] used a 5 MHz sensor in 36 locations to spatially resolve US diagnostics of the electrodes in LIBs. The authors state that the acoustic peaks were typically doublets, or two peaks in close proximity. These doublets exhibited a noticeable change during charging and discharging: during charging the earlier peak would decrease in amplitude whilst the later peak would increase in amplitude. This was attributed to the density changes in the anodes and cathodes, with one peak associated to one electrode type. The depth of the anode current collecting tab was detected due to variation in the ToF across the 36 locations. This suggests that localised defects could be detected using ultrasound.

In order to test this, the viability of detecting defects within Li-ion cells using US was investigated by Robinson et al. [100]. Bespoke pouch cells of pristine condition and built-in defects were compared. The location and scale defects were measured and verified via the use of X-ray tomography. It was found that the signal must be tailored to the cell. A microscale defect was also recorded, that was ca. 20 µm in diameter. An area of 200 µm around the defect was observed in a commercial cell to create an acoustically resistive 'void', affecting the propagation pathway. This resulted

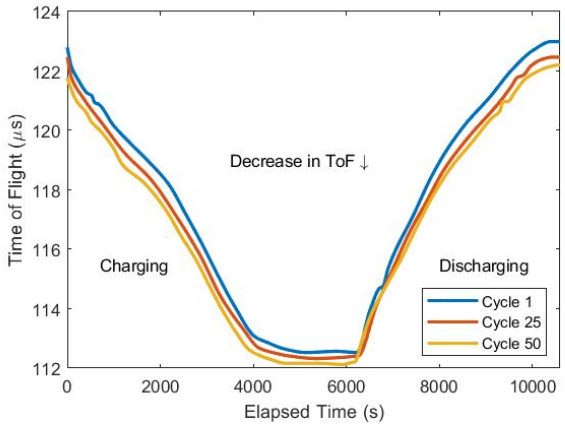

(a) US evolution demonstrating the change in ToF during a full charge and discharge cycle for a single AScan peak. A comparison between different cycles shows a general decrease in ToF as the cell aged. Recreated from [95].

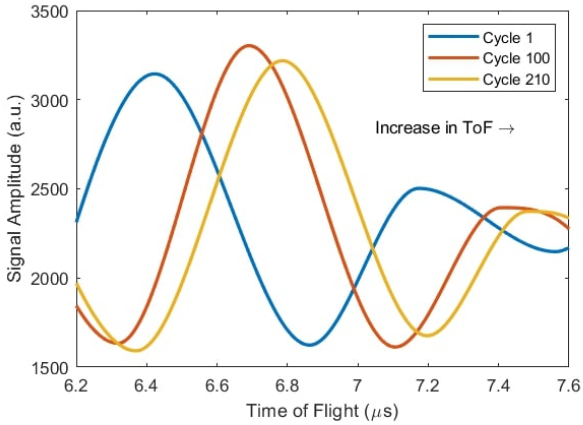

(b) First reflection of an AScan after different charge cycles. An increase in ToF can be seen by the shift of the first peak to the right, but the rate of change of ToF decreases as the cell is further cycled. A change in amplitude of the peaks is also observed. Recreated from [96].

Figure 3.3: Comparison of ToF change of a single AScan peak from two cells during aging testing.

in a delayed response in the signal, which was not detected in the bespoke cells.

Table 3.2 summarises the research and respective findings in this subsection.

Aim	Diagnosis	Transducer Setup	Reference
Detection of degradation methods	Amplitude decreased as the cell was cycled	5 MHz pitch-catch	[81]
ToF shift during cell ageing	ToF decreases as cell ages	Guided-wave pitch-catch	[95]
	ToF increases as the cell ages	1 MHz pulse-echo	[96]
Capacitor degradation during over- and undercharge	ToF shifts could be used to detect gas swelling and SOC changes	125-500 kHz through-pulse	[97]
US detection of SEI formation and cycle-induced capacity loss	Onset of gassing from SEI formation was detected by the ToF. ToF increased as capacity dropped	2.25 MHz through-pulse	[98]
Spatial resolution of electrodes	ToF shifts agreed with previous reports. Able to detect the depth of the anode current collecting tab.	5 MHz pulse-echo	[99]
Detection of localised defects in cells	Defects were measured and verified	10 MHz pulse-echo	[100]

Table 3.2: Table of SOH diagnosis using ultrasound.

3.1.3 Summary

Recent research had suggested that US monitoring of LIBs could be used to infer the SOC and SOH of cells despite it being an emerging field. It has been posited that information regarding the internal conditions of cells could be provided without damaging the cells. The technique could also be used in tandem with conventional BMSs to provide a more concrete understanding of cells. However, use of US to identify and decouple the failure modes in LIBs requires further work.

It is difficult to identify features within a cell as the US signal is complex due to the superposition of the main pulse and smaller internal reflections. It is suggested that defects and degradation could be detected, and characterised by depth and size, using US. But the failure mechanism/mechanisms causing the degradation were not discernable without the use of other techniques. This also means multiple defects could not be separated from each other, as the effects would be combined within the US signal.

Ultrasonic monitoring of LIBs is subject to limitations. Notably, as the monitored cell experiences degradation or develops defects, the ultrasonic signal response undergoes analogous changes, such as a global ToF shift [95, 96]. Such changes can have an adverse effect on the precision of SOC estimations, as this is reliant on the shift in ToF.

There are some disagreements in the literature; for example, the ageing of a cell

has been shown to both increase and decrease the ToF. The cause of this discrepancy could be the behaviour exhibited by the cell as it ages; gas generation would reduce the acoustic signal and SEI formation would increase the ToF due to an increased path length - the SEI formation creates new layers within the cell [98]. Further research is required to decouple gas generation, electrode delamination, voiding and electrode expansion such that the effects due to ageing can be isolated.

The impact of temperature on ToF measurements is a subject of debate within the literature. Preliminary research has suggested that temperature may have a reduced effect on ToF within earlier ranges (up to 5 µs) [6], though modelling data argues that temperature variation could reduce the reliability of the US signal [7]. Further investigation is imperative to determine the influence of temperature, both in static and dynamic states, on US measurements conducted at varying ToF ranges.

3.2 Thermal Runaway

Thermal runaway is a significant safety concern for LIBs as it can lead to a fire and/or an explosion [101, 102]. The occurrence of TR events are rare, but as the use of LIBs increases it is important to develop technologies that prevent TR and allow detection in its earliest stages. There are two practical detection methods that can be incorporated into LIBs for the early detection of TR onset. These are expansion (dilatometry, strain/force) and acoustic (acoustic emission, US probing) based methods [85].

TR within a LIB is a process in which the exothermic chemical decomposition of the active battery materials and electrolyte lead to exponentially increasing reaction and heat generation rates with temperature [103, 104]. Failure within LIBs leading to TR can be caused by thermal (e.g. cell overheating), physical (e.g. cell penetration) and electrical (cell over-charge) abuse. During failure, multiple events occur including: cell swelling; SEI decomposition; gas generation; the separator melting; electrolyte evaporation; internal short-circuiting and; cathode-electrolyte interaction [37, 102–112]. See Table 3.3 for the expected temperatures and temperature rates of the events stated, which is visualised in Figure 3.4 along with the effects from over- and under-charging.

Feature	Expected value	Reference
Swelling/delamination	40°C / 60°C	[107]
SEI decomposition	57°C†, 80°C‡	[37, 113]
Electrolyte evaporation	60 - 100°C	[114]
Anode decomposition	80 - 160°C	[115–118]
Separator melt (PE/PP)	130°C /170°C	[102]
Onset of self-heating	$0.02\,^{\circ}\mathrm{C\,min^{-1}}$	[119]
Onset of Thermal runaway	$1.0\,^{\circ}\mathrm{C\,min^{-1}}$	[119]

†Theoretical

‡Detectable

Table 3.3: Summary of the events during thermal runaway and their respective onset temperatures.

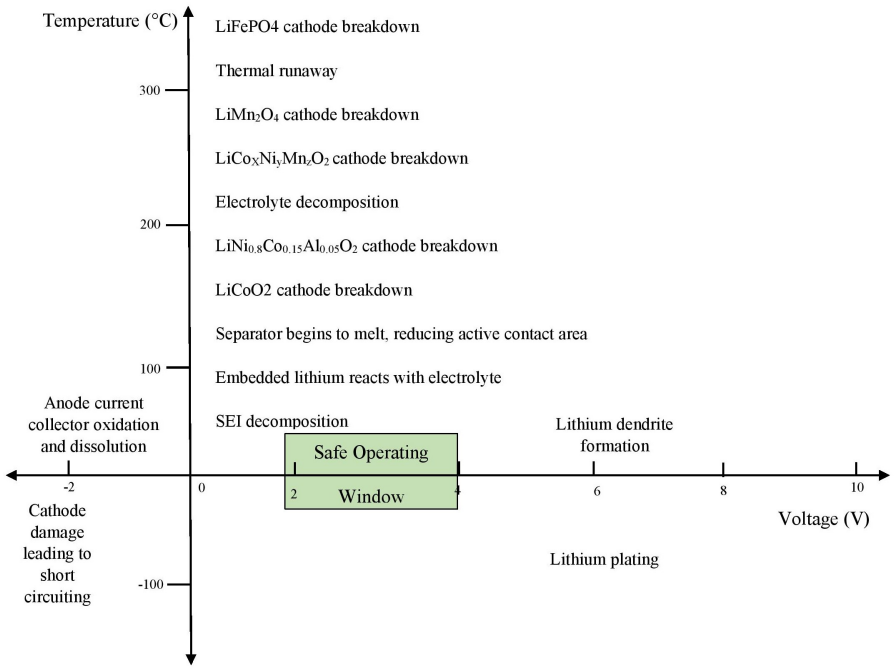

Figure 3.4: Generalised safe operating range of Li-ion cells, and events that occur outside said range, recreated from [32].

3.2.1 Thermal Abuse

LIBs have an optimum operating temperature of 20 °C to 40 °C [120]. Outside this range, the battery experiences accelerated ageing [121]. The increased ageing is caused by the build-up of the SEI, increasing the internal resistance of LIBs. The SEI is the reaction between the active electrode materials and conductive salt within the interface between the separator and the active electrodes, namely the anode [122]. The chemistry of the cathode and SOC of the cell both affect the thermal stability (i.e. onset of thermal decomposition) and heat released during TR, shown in Table 3.4 [104, 123–126].

LFP cells tested under adiabatic calorimetry in an accelerated rate calorimeter (ARC) were observed to not undergo TR below 28% SOC, but at SOC greater than 28% TR onset occurred at approximately 200 °C, as seen in Figure 3.5. The anode was the major influence on self-heating in the cell at an SOC above 28% up to 100%. Above 100%, the cathode and anode have more equal influence [119]. This has been explained as a fully lithiated anode generates an order of magnitude more heat than a fully lithiated cathode [112, 118].

LCO cells have been observed to have poorer thermal stability than LFP cells. At 50% and 100% SOC, the LCO cells were found to have a much greater explosive power than the LFP cells, reaching an equivalent of 1.77 g of TNT at 100% SOC [136]. The TNT equivalents can be seen in Table 3.5. Though it should be noted that while both chemistries exhibited high temperatures and pressures, LCO cells exhibited greater temperatures and pressures.

Compared to LCO, LMO exhibit a greater thermal stability across all SOC up to 120%. This was examined by Hernandez et al. [125]. Two types of 18650 cells, one LCO and one LMO, were charged to the desired SOC, then placed in an ARC. The cells were heated using a Heat-Wait-Seek (HWS) method, which heated the cells by 5 °C with a waiting-step of 30 minutes and a seeking-step of 5 minutes. The seeking step monitored for high self-heating rates, defined as above 0.05 °C min^{-1}. As stated, LCO cells undergo TR at 50% SOC and above. LMO cells undergo TR at 75% SOC and above, with consistently lower temperature increase rates compared to LCO cells, as seen in Figure 3.6 [125].

Synthesized $LiMnPO_4$ (LMP) cells have been found to be less thermally stable than LFP cells, as greater amounts of heat are produced when overheated at a delithiated state. This is accompanied by a lower onset temperature on par with NCA cells [111, 137].

3.2.2 Mechanical Abuse

Penetration induced TR in an array of NMC cells was investigated by Feng et al. [103]. The first battery was penetrated by a nail to a depth of 8 mm at a speed of 10 mm/s. From penetration, it took around 10 seconds for the penetrated cell to reach TR, with the following cells reaching TR due to the heat from their respective preceding

Cathode	Ref.	Temperature Range of Decomposition (°C)	Heat Release (J g^{-1})
LCO	[127]	220-500	450
NCA	[128]	160	850±100
	[129]	200	793
LMO	[130]	225-400	350±100
	[127]	150-300	450
	[131]	89	2014.3
LFP	[132]	190-285	290
	[133]	180	145
NCM	[134]	17	322.7
	[134]	178	364.3
	[134]	183	534.6
	[134]	199	645.8

Table 3.4: Reaction properties of different cathode materials [135].

Cathode Material	SOC (%)	TNT Equivalent (g_{TNT}/18650 cell)
LFP	50	0.11
LFP	100	0.23
LCO	50	0.88
LCO	100	1.77

Table 3.5: TNT equivalent per individual 18650 type cells at thermal runaway [136].

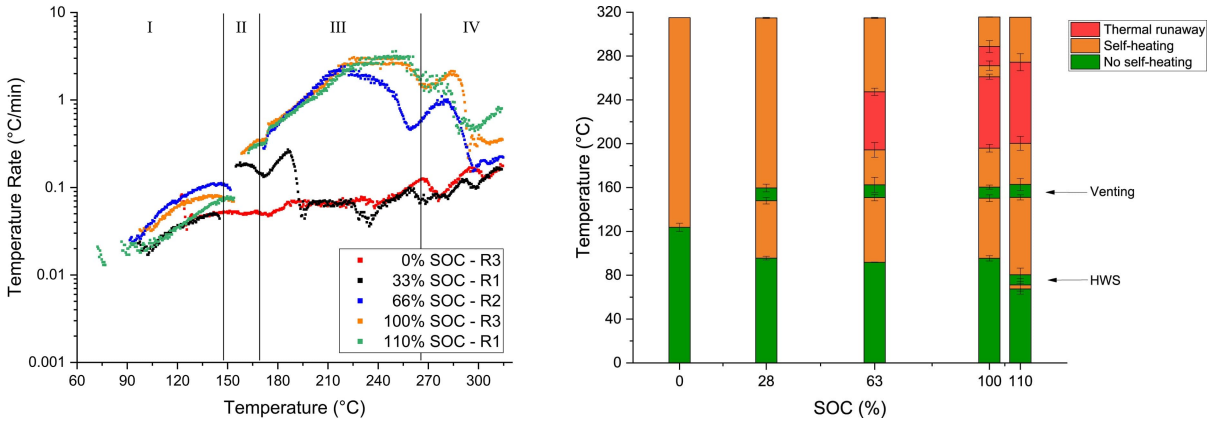

(a) (b)

Figure 3.5: (a) Rate of temperature change of LFP cells at different states-of-charge within an ARC. Regions: I - first exothermic event (self-heating); II - endothermic event (venting); III - second exothermic event (first peak temperature rate); IV - third exothermic event (second peak temperature rate). (b) Thermal map of (a) stating when a cell underwent self-heating and entered thermal runaway at the tested states-of-charge. Reproduced from [119].

cell. Once TR was achieved in the first cell, it took around five seconds for the sixth cell to reach TR. It was found that the TR onset temperature was lower for penetration than for uniform heating TR. The cause of TR was the breakdown of the separator, causing short circuiting [103, 138]. However when penetrated, the temperature distribution through the cells was not uniform, as the heat generation localised around the penetrated area. This creates a temperature gradient in the cell. The TR propagation is independent of fire during the self-heating, as the heat transfer between the cells had little variation from the cells that caught fire and those that did not [139].

The thermal and electrochemical behaviour of a penetrated cell is independent of the penetration speed [140, 141]. The location of the nail when penetrating had an effect on the thermal behaviour. Penetration at the edge of the electrode was found to be more dangerous, as the heat dissipation to the cell wall/nail was limited by the separator and electrolyte thermal conductivity [142]. The SOC of the cell had an effect on the onset of TR, similar to [119]. For 18650 type cells with cathode material of 98% NMC and 2% LMO, an SOC of less than 50% would not lead to TR when the cell is penetrated, which was found to be higher than the cutoff for uniform thermal heating of 28%. The maximum temperature of the cell was also dependent on the SOC: a higher SOC results in a higher TR maximum temperature [143].

3.2.3 Electrical Abuse

Over-charging-induced TR is dangerous due to the excess energy in the cell [102, 144]. When the SOC of the cell is charged above 120%, oxidation within the electrolyte occurs, and lithium deposition on the anode surface begins [145, 146]. This differs

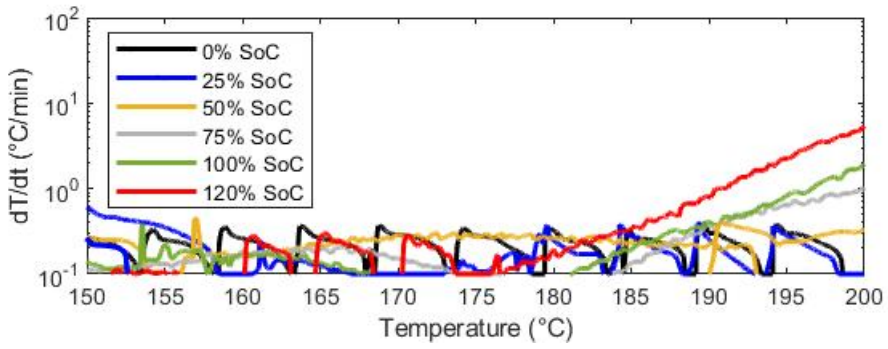

(a)

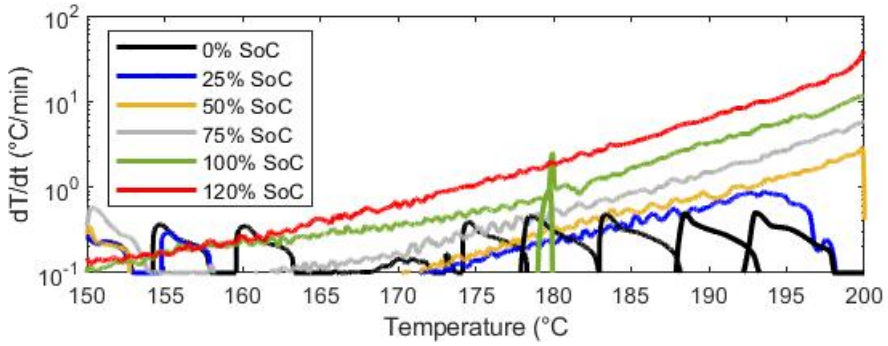

(b)

Figure 3.6: Heating rate compared to temperature of a (a) LMO cell and a (b) LCO cell at various states-of-charge. Recreated from [125].

from the SEI layer as the lithium does not react with the electrolyte. The SEI film would thicken due to a solvent reaction with the deposited lithium, increasing the internal resistance [146]. Above an SOC of 140%, the cell would see an increase in the rate of temperature rise causing: swelling; increased electrolyte oxidation and heat generation [147, 148]. This would cause the SEI to decompose, leading to an lithiated anode-electrolyte reaction [103, 115]. There was a drop in voltage, despite the SOC increasing [149]. Above 160% SOC, the internal pressure ruptures the cell, leading to thermal runaway [147].

The heat generation caused by over-charging was investigated by Saito et al. [150], where it was found the heat generation was closely proportional to the C-rate. This suggests the heat generation is largely influenced by ohmic heating. The onset of heating was located in the cathode, regardless of the level of cathode lithiation [151]. The cathode also provides the strongest intensity of TR when heated, compared to the other materials in the cell [152]. When a cell has been over-charged, a number of outcomes can occur; the cell can swell from gas generation at low currents and rupture at higher currents [151].

The effect of over-charging on the onset of TR was investigated by Zhang et al. [153]. The cells were charged to SOCs of 100%, 105%, 110%, 115%, 120% then heated via HWS. The cells were measured for the self heating temperature, T1 (self-heating

rate of >0.02 °C min^{-1}), TR trigger temperature, T2 (>5 °C min^{-1}) and maximum temperature, T3. It is shown that the TR onset temperature decreases with SOC increase above 100%. It was stated that the time required to reach TR also decreases up to 4.8 V, suggesting that over-charging can cause an early onset of TR [153, 154].

3.2.4 Gas Generation

Gas generation occurs during normal and abusive operation of LIBs. Monitoring the gas production internally within a cell is challenging with typical battery state determination methods derived from voltage, current and temperature measurements [155, 156]. However, mechanical measurements could provide information about internal condition of cells, specifically regarding to safety, as they can detect the physical changes resulting from decomposition [85].

The evolution of gases during lithium-ion operation is not fully understood. During normal operation, multiple gases are generated due to chemical reactions, such as hydrocarbons and hydrogen fluoride. One such gas is C_2H_4. During the first cycle, there is a sharp increase in concentration in C_2H_4. The formation of the SEI layer is suggested to be associated with this generation [157, 158]. Following the initial formation, concentration of C_2H_4 gas increases at a slower rate, independent of the cycling voltage [158] or stops increasing [159]. CO is believed to evolve simultaneously with C_2H_4, but can be attributed to the absorbed-on-cathode atomic oxygen during electrolyte decomposition [160]. Increase in the concentration of CO_2 rise is believed to be a result of a chemical reaction between residual moisture and CO evolution on the anode during the charge cycle [159]. H_2 evolution is believed to be the result of residual H_2O in the cell [160, 161]. A comprehensive review of gas generation and evolution during normal operation is covered by Rowden et al. [158].

The generation of gases can cause internal structural changes and delamination when a cell is heated above normal operating temperatures. Gas pockets have been seen using CT and X-ray imaging when the surface temperature reached values greater than 100 °C [108, 162]. Over-charging a LCO pouch cell showed that swelling began at 40 °C with no adverse changes to the voltage profile, while delamination was observed at 60 °C with a rise in voltage as internal resistance increased due to gas generation and delamination [107]. Compared to temperature rate data [103, 104] this shows that gassing occurs before significant rates are recorded, and hence provides an opportunity for the early detection of TR. In these cases, gas was generated from the decomposition/degradation of the electrolytes and SEI, which can be a result of both thermal and electrical abuse.

NMC cells have a similar thermal stability to LCO, as at 50% SOC the cells do not undergo TR [163]. This was observed using force readings, along with temperature and voltage readings similar to the methods mentioned above. Notably, for both 50% and 100% SOC for NMC cells, there was an abrupt and substantial rise in force readings, followed by a subsequent decline due to off-gassing. This observed pattern exhibited a strong association with the generation and subsequent venting of gases. The rate of gas generation was found to be faster at higher SOC than lower SOC, and this was observed in the force readings [163].

Swelling is not uncommon to observe in abused Li-ion pouch cells. The swelling increases the stress on the cell casing and internal layers leading to cell rupture and delamination, respectively [164, 165]. The delamination of the internal layers in the jelly roll of hard cased cells (cylindrical and prismatic) is caused by the gas generation, along with the heat generation [108, 144]. The gas will also increase the overall thermal resistance of the cell significantly [165, 166]. This is due to the increased spacing between the layers, where the initial thermal resistance of the air is negligible compared to the layers.

3.2.5 Detection of TR

Failure mechanisms can be present in the lead up to TR, such as gas generation; temperature increase; and voltage drop. In order to detect TR, monitoring attempts of these mechanisms have been made.

As stated in Section 3.2.4, gas generation occurs before changes in temperature. Modelling the efficacy of gas generation monitoring as a TR detection method has been performed by Cai et al. [167]. Nine NMC 18650 cells were modelled in a three by three grid in the centre of a cylindrical drum with a radius of 0.292 m and a height of 0.85 m. The model estimated centre cell was externally short circuited and underwent TR. The drum was modelled at atmospheric CO_2 concentrations - 400 ppm - and would detect TR at a CO_2 concentration of 2000 ppm. The time taken for the neighbouring cells to undergo TR was 710 s, called t_{crit}. The gas sensors detected TR after 85 s, which was significantly quicker than t_{crit}. At t_{crit}, the drum surface temperature changed by less than 0.001 °C.

Force sensors have also been used to measure gas generation during TR. A cell was fixed in place, with force sensors attached to the corners of the fixture in order to measure battery expansion [163]. Two NMC pouch cells underwent internal short circuiting, one at 50% SOC and one at 100% SOC. Only the 100% SOC cell underwent TR. However, the force sensors were able to detect internal cell pressures for both tests accurately when compared to the modelled pressure increase. Both tests saw a quick drop in force, which was due to the cells venting.

Attempts to use temperature for TR onset detection have been made. External surface temperature measurements were unable to provide enough time in order to shut off the cell before TR and more extreme reactions, such as fires, could occur [168].

Seven sensors - voltage; gas; smoke; temperature; pressure; creep; and force - were tested and compared by Koch et al. [169]. Three experiments, V1; V2; and V3, involved cells undergoing TR. V1 was a 20 Ah NMC cell that underwent thermally induced TR. V2 and V3 involved multiple NMC cells undergoing penetration induced TR. V2 and V3 used 65 Ah cells and 58 Ah cells, respectively. The capacity of the cells differed between tests, but were consistent within each test. The sensors were based on three criteria: detection speed; signal clarity; and sensor feasibility. Each sensor was graded good, neutral or bad for these criteria, see Table 3.6 for performance in these criteria. It was found that no single method was deemed the 'favourite'.

In a similar fashion, Klink et al. [170] compared seven detection sensors. These were: voltage; current; temperature; strain; gas; smoke; and pressure. A model-

Sensor	Detection Speed	Signal Clarity	Sensor Feasibility
S1 - voltage	Bad	Good	Good
S2 - gas	Good	Good	Bad
S3 - smoke	Bad	Neutral	Neutral
S4 - creep	Bad	Bad	Good
S5 - temperature	Neutral	Neutral	Neutral
S6 - pressure	Good	Bad	Good
S7 - force	Good	Bad	Neutral

Table 3.6: Evaluation of different sensors based on three criteria. Signal clarity describes how close the detection signal comes to a step function and how easy it is to evaluate it, whereas sensor feasibility evaluates how easy the sensor can be deployed. Reproduced from [169].

based method was also compared. The experimental methods were all capable of detecting TR more than five minutes before TR onset, which was the baseline for the work. The model was the quickest in detecting TR; TR was detected significantly earlier compared to the five minute pre-warning time. The smoke and gas sensors also achieved this. There were eight criteria the sensors were tested on: detection time; certainty; localisation; monitoring; complexity; integration; scalability; and transferability. The model performed the best against these criteria, with voltage, gas and smoke performing the best out of the experimental methods. This is in disagreement with Koch et al., as the smoke sensor did not perform as well in their work [169]. Further investigation is required to conclude the effectiveness of these sensors. There was contention over the efficacy of the gas sensor. Koch et al. stated that the gas sensor is not feasible given the large size and energy requirement [169], while Klink et al. stated that it is a viable method [170]. Both papers were in agreement of the feasibility of the other sensors.

3.2.6 Summary

Li-ion cells can be damaged by multiple abuse mechanisms, including thermal, mechanical and electrical. These mechanisms can cause failure mechanisms such as: electrode delamination; electrode decomposition; short circuiting; gas generation; and cell self heating, all which can lead to thermal runaway. The chemistry and SOC of the cell has also been shown to have an effect on the behaviour of TR, including the onset of TR and the overall hazards from the failed cell. Research into the detection of TR is limited, and not always successful [171].

Multiple sensors for detecting TR have been tested including gas, temperature, voltage, smoke, and force [167–170]. Not all these methods were able to detect TR individually, but were successful when combinations of the sensors were used. The gas sensor was shown to have good detection speed and signal clarity across multiple tests, however there is contention with the feasibility of such a sensor [169, 170]. Current BMS struggle to monitor gas production [155, 156]. US has been shown to be sensitive

to internal changes within cells in Section 3.1.2, such as gas generation [100], whilst having a smaller form factor and lower power consumption, which may make it a viable method of detecting TR.

3.3 Ultrasonic Monitoring of Li-ion Abuse and Thermal Runaway

As shown in Section 3.1, US monitoring of LIBs has been a growing field in the last decade. While Section 3.2 showed that TR monitoring of Li-ion batteries has been a large field for over a decade. However, there has been little work that considers coupling these two research areas which together have the potential to make significant advancements in the detection of TR. However, interest in coupling these two areas have developed in recent years.

In 2019, Robinson et al. [6] looked into the cycling behaviour of LIBs using US, and assessed the impact of thermal expansion caused by temperature change during charging. A 210 mA h LCO cell was cycled at 1 C, with the US data at 25 °C and 30 °C being recorded. The cell was then heated in a climate-controlled environment, with the US data being recorded at the temperature extremes. From the AScans of the climate-controlled tests it was observed that there were no significant changes in the low ToF peaks (0 to 5 us). However small changes in the signal amplitude were observed; the 30 °C signal had a slightly greater amplitude over the 25 °C signal for most of the peaks. The authors suggested the change in intensity was due to variations in the Young's modulus rather than temperature.

Chang et al. [172] cycled LCO cells over a temperature range of 0 - 60 °C. Using US, it was demonstrated that the cells underwent catastrophic failure across the temperature range. Lithium plating typically occurs below 10 °C with this cathode, which can lead to excessive gassing if a high temperature shift occurs. In order to monitor this, cells were cycled at 1 C at temperatures below 10 °C then heated to 20 °C, 30 °C, 40 °C, 50 °C and 60 °C. It was found that for all tests, the ToF shifted after cycling and heating, with the shift increasing in magnitude with temperature. All tests also saw a loss in acoustic signal. The 60 °C test saw signal loss within one hour of reaching the target temperature and the 20 °C test losing acoustic signal after approximately 63 hours of reaching the target temperature. This was suggested to be caused by accelerated electrolyte degradation at higher temperatures, combined with the lithium plating.

Zappen et al. [121] measured in-plane and through plane signals during the thermal abuse of a pouch cell. The cell was heated with pauses until 110 °C, at which point it was allowed to passively cool. When plotting the US signal amplitude against temperature, changes in the signal were identified at 65 °C and then again at 90 °C. This is in the temperature range of SEI decomposition and electrolytes evaporation. Unlike other work, Zappen used the *centre of gravity* (µ s) of the US signal to infer material changes. The *centre of gravity* allows for the optimal fraction of the peak that contains the most information about the peak position, using the original signal or the 1^{st} or 2^{nd} derivatives [173]. The *centre of gravity* is dependant on the speed of sound

through the medium as well as the signal intensity. For both the signal intensity and *centre of gravity*, there was a significant change at 90 °C. The signal intensity reduced while the centre of gravity increased for both in-plane and through-plane readings.

Pham et al. [165] investigated gas-induced delamination during thermal runaway using US. A trend of increased ToF was observed during gradual cell heating, which was attributed to the decrease in density of the electrodes, leading to a decrease in propagation speed. The rate of heating, and therefore the rate of propagation of thermal runaway, had a positive effect on the ToF shift; a more gradual propagation resulted in a more gradual ToF shift. A gradual thermal runaway propagation also led to prolonged gas generation, which meant a greater time between the loss of the US signal and the onset of thermal runaway. The test used two 210 mA h cells. Cell 1 underwent gradual heating, whilst cell 2 underwent more aggressive heating. The more gradual heating of cell 1 resulted in a sharper increase in ToF and a more abrupt loss of signal compared to cell 2, yet the onset of failure began later. It was suggested that the quicker propagation of TR in cell 1 was due to the lower temperature gradient, resulting in a higher average temperature.

Owen et al. [174] looked into the behaviour of US signals based on changes in temperature and charge cycling rates. It was found that, at constant SOC, the ToF increased as the temperature increased, with the shift becoming greater at lower SOC. This was measured over a range of 0 to 10 µs, focusing on the first echo around 8 to 9 µ s. The relationship between temperature and ToF was linear across all SOC, as well as the gradient of temperature and SOC. The authors also looked into decoupling the temperature effect on ToF from the SOC. This was achieved by subtracting the change in ToF caused by temperature change - from a separate test - from the measured change in ToF from the charge cycle. The difference between the corrected and measured ToF was shown to diverge more as the temperature increased during discharge, suggesting temperature has an effect on the change in ToF shown in Figure 3.7. The resultant shifts in ToF were suggested to be due to material changes of the electrodes as they "relaxed", as indicated by a similar change in the voltage.

Appleberry et al. [175] used pitch-catch US monitoring to provide warnings about cell over-charging, and test feasibility of stopping cell operation (E-stop). The warnings would occur if the signal amplitude would reduce by at least 3.5 standard deviations from normal operation, and the cell would stop when the amplitude dropped below 10 standard deviations. The US detection consistently identified failure conditions as each test resulted in a warning and a triggered E-stop. Time before warning and E-stops did vary between the tests (see Table 3.7.) At the point of these warning the signal amplitude decreased rapidly. The loss of amplitude was attributed to the gas generation from the overcharge scenario.

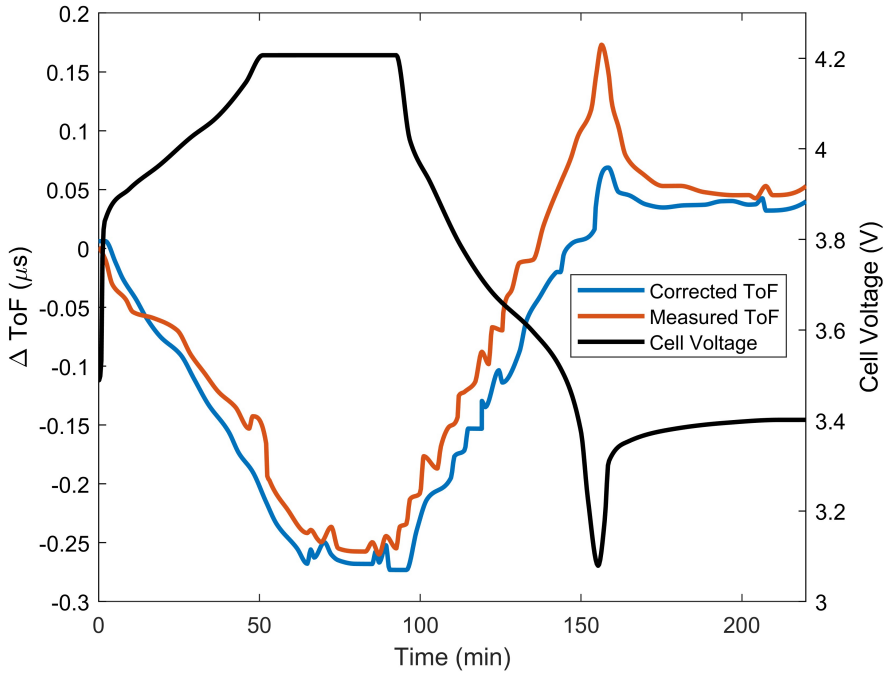

Figure 3.7: Difference in ToF variation due to temperature effects, superimposed on the voltage profile. Adapted from [174].

Experiment	Induced failure	Warning before failure	E-Stop before failure	Time from overcharge to failure
1	~23°C, CC-overcharge	124 min (81%)	54 min (35%)	154 min
2	~23°C, CC-overcharge	90 min (66%)	90 min (66%)	136 min
3	~23°C, CV-overcharge	93 min (93%)	92 min (92%)	100 min
4	~23°C, CV-overcharge	348 min (99%)	347 min (99%)	352 min
5	65°C, CV-overcharge	21 min (84%)	15 min (60%)	25 min
6	65°C, CV-overcharge	20 min (65%)	19 min (61%)	31 min
7	65°C, CV-overcharge	12 min (75%)	4 min (25%)	16 min
8	65°C, CC-overcharge	76 min (50%)	58 min (38%)	151 min
9	65°C, CC-overcharge	285 min (99%)	139 min (48%)	289 min

Table 3.7: Summary of experiments and the respective response time for the warning and E-stop compared to the failure time, reproduced from [175].

3.4 Compilation of Published Work on Ultrasonic Monitoring of Lithium-Ion Cells

Table 3.8: Compilation of Published Ultrasonic Detection Work.

Authors, Reference	Test Parameters	Analysis
	2013	
Sood et al. [81]	Frequency: 5 MHz Mode: Pitch-catch Room Temperature C-Rate: 0.5C	Weakened acoustic signal and delayed response due to degradation
	2015	
Hsieh et al. [82]	Frequency: 2.25 MHz Mode: Pitch-catch Room Temperature Chemistry: LCO C-Rate: 0.4C	Ultrasonic response was correlated with SOC. Increase in SOC resulted in decreased TOF and signal amplitude
	2016	
Ladpli et al. [95]	Frequency: 100-200 kHz Mode: Pitch-catch - Rayleigh Temperature: 23°C C-Rate: 0.18C	Cell degradation resulted in decrease in global TOF
	2017	
Gold et al. [83]	Frequency: 200 kHz Mode: Pitch-catch Room Temperature C-Rate: 2C and 4C	Slow reflections were sensitive to SOC in terms of TOF and amplitude. Change in signal was due to volumetric expansion/contraction of anode
Davies et al. [94]	Frequency: 2.25 MHz Mode: Pitch-catch Room Temperature Chemistry: LCO and LFP C-Rate: 0.5C	Different chemistries can affect TOF estimation error. Acoustic estimation was more accurate than voltage measurement based estimations
	2018	
Ladpli et al. [92]	Frequency: 100-200 kHz Mode: Pitch-catch - Rayleigh Temperature: 30°C C-Rate: 0.1C	Rayleigh surface waves were able be used to accurately estimate SOC and SOH

Continued on next page

Authors, Reference	Test Parameters	Analysis
	2019	
Popp et al. [90]	Frequency: 30 kHz Temperature: Cycled between 5 - 45°C in 10°C steps Chemistry: NMC Mode: C-rate: 0.1, 0.5 and 1C	Higher C-rates resulted in longer TOF. Higher temperatures also resulted in longer TOF
Chang et al. [80]	Frequency: 400 kHz Mode: Through pulse Temperature: 25°C Chemistry: NMC C-Rate: 2C and 4C	Air coupled ultrasonic detection is feasible. Fast waves were sensitive to SOC changes, along with slow waves.
Wu et al. [96]	Frequency: 1 MHz Mode: Pulse-echo Temperature: 45°C Chemistry: LCO C-Rate: 0.5C	TOF increases with cell degradation. Internal gas generation can be detected via ultrasound
Copley et al. [7]	Model based on conditions from [82]	Small changes in in electrode material properties can have significant effects on TOF. TOF has a stable correlation with SOC, but amplitude is not. Frequency can affect signal reliability based on penetration power
Oca et al. [97]	Frequency: 120 - 500 kHz Mode: Through pulse Chemistry: NMC Temperature: -30 - 70°C C-Rate: 10C	TOF was able to detect permanent changes from abusive charging that voltage measurements could not see. TOF could be used to detect swelling
Robinson et al. [99]	Frequency: 5 MHz Mode: Pulse-echo Chemistry: LCO Room Temperature C-Rate: 0.035C	Individual peaks of a reflection were coupled. The amplitude of the doublets were inversely related. Localised defects could be detected using ultrasound if spatially monitored

Continued on next page

Authors, Reference	Test Parameters	Analysis
Robinson et al. [6]	Frequency: 2.25 MHz Mode: Pulse-echo Chemistry: LCO Temperature: Controlled C-Rate: 1, 2 and 4C	Temperature had no observable change on fast wave TOF. Signal amplitude saw a change with a change in cell temperature. This was suggested to be due to material property changes rather than temperature
2020		
Robinson et al. [100]	Frequency: 1 MHz Mode: Through pulse Chemistry: LCO Room Temperature	Purposefully built-in cell defects were detected using ultrasound. A microscale defect was also detected that was not built-in. The defects were confirmed through the use of X-ray tomography
Bommier et al. [98]	Frequency: 2.25 MHz Mode: Through pulse Chemistry: NMC C-Rate: C/50, C/12, C/7, C/5 and C/2.5	Gassing potentially caused by SEI formation and growth was detected by the TOF. TOF increased with cell degradation.
Chang et al. [172]	Frequency: 2.25 MHz Mode: Through pulse Chemistry: LCO Temperature: 0 - 60°C C-Rate: 0.1 and 1C	An increase in temperature so an increased shift in TOF to a higher value. Higher temperatures also saw a quicker loss in acoustic signal response once said temperature was reached
Zappen et al. [121]	Frequency: 2.25 MHz Mode: Through pulse and Rayleigh Chemistry: NMC Temperature: 2K/min until thermal runaway, ramp with pauses until venting and ramp with pauses until 110°C Charge Levels: 50% and 100% SOC	The signal intensity was weaker at higher temperatures
Pham et al. [165]	Frequency: 2.25 MHz Mode: Pulse-echo Chemistry: LCO Room Temperature C-Rate: 0.5C	Increase in temperature saw an increase in TOF. A higher rate in temperature increase saw a greater increase in TOF.

Continued on next page

Authors, Reference	Test Parameters	Analysis
	2022	
Owen et al. [174]	Frequency: 5 MHz Mode: Pulse-echo Chemistry: LCO Room Temperature C-Rate: 0.2, 0.5 and 1C	TOF saw a linear increase with temperature at constant SOC. Lower SOC saw a greater TOF shift with temperature. Temperature effects were decoupled from the TOF. Achieved through subtraction of TOF change via temperature from a separate test from TOF change from cycle test.
Appleberry et al. [175]	Frequency: 500 kHz Mode: Through pulse Temperature: Room Temperature and 65°C C-Rate: C/0.38	Ultrasonic detection of failure conditions before cell went into failure. Warnings and emergency stops were given before failure with varying levels of success

3.5 Review Discussion

Ultrasonic monitoring of the Li-ion cells has been researched and implemented by numerous researchers as reported in literature. Either by direct coupling or air coupling, the SOC of cells can be accurately estimated over a large range of frequencies. The sensors are low cost and easy to implement onto current cells, however the form factor of many sensors used are too large for practical applications. Individual transducers, which have a small form factor, have been successfully used at low frequency. Pitch-catch and pulse-echo inspection modes have both proven effective at monitoring LIBs. The benefit of this approach is the ability to measure the internal failure mechanisms of the cell *in-situ*, allowing for the detection of gas generation, swelling, lithium-plating and ageing of cells in a non-destructive method. Detection of these behaviours can occur much earlier using ultrasound compared to more conventional BMS systems. While research has shown the aforementioned failure mechanisms can be detected in dedicated failure tests, further work is required to identify which failure mode is occurring within a cell under real world operating conditions. Considering that failure modes of this type can occur simultaneously there is also the need to deconvolute the signals of concurrent failures so that the correct failure mechanism is identified.

Abuse conditions have been widely studied in LIBs as a result of the inherent risks of this technology, notably the risk of thermal runaway. The cathode material has a major effect on the stability of the cell, causing the onset of TR to vary across LIBs. Independent variables in the cell, such as the SOC, C-rate and temperature, also have an effect on the stability of the cell. The monitoring of TR can be detected when the cell is electrically, thermally or mechanically abused. The cause of internal gas

generation, and subsequent cell swelling, has been researched in different chemistries and cell form factors. However, the detection of TR is still needing development, as these methods require external variables to monitor the cell. External variables include, but not limited to, open-circuit voltage characterization and coulomb counting. Open-circuit voltage characterization requires cutting off power to the cell to allow for an extended period of rest, meaning it is not applicable for *in-situ* use [176]. Coulomb counting requires knowledge of the initial SOC and cell capacity, and is at risk of errors such as time oscillation drift [177]. The use of a BMS with the addition of ultrasonic sensors to monitor the internal and external behaviours of cells could improve the detection of abuse symptoms, allowing for the mitigation of thermal runaway during cell operation.

Recently research has begun into the use of ultrasound to monitor temperature and TR effects in LIBs. Symptoms of abuse conditions can be detected by ultrasonic signals during thermal and electrical abuse testing. The coupling of the temperature and SOC effects on the ultrasonic signal is an aspect that needs addressing in order to allow this application of ultrasound to be accurate. Ref [6] determined that temperature did not have an effect on the ultrasonic signal within 5µs, as the difference in the AScans at 25°C and 30°C showed slight variation but was suggested to be caused by differences in the elastic modulus. However, refs [7, 174] found that when charging/discharging, the temperature, and rate of change, causes the ultrasonic signal to deviate from the expected result outside of 5µs. During operation, cells generate heat energy due to internal resistance. This heat energy causes thermal expansion in all layers of the cell, increasing the volume of the cell. This results in a longer ultrasonic path, and therefore longer ToF. Thermal expansion also increases the speed of sound, which would decrease the ToF. Additional to these thermal effects, the (de)intercalation of lithium-ions within the electrodes and their movement through the cell will change the elastic modulus, density and volumes of all layers, thereby affecting the speed of sound and ToF. As shown by [174], temperature has an overall increase in ToF. This suggests that the thermal expansion of the cell has a greater effect than the density change due to temperature and the change in material properties due to (de)intercalation.

3.5.1 Conclusion

- There has been limited discussion on the effects of temperature on the signal during cycling. Within that there is disagreement. An attempt to decouple temperature effects from charge has been made.
- There is contention on which section of the signal should be used for estimations. Processing methods are rarely described.
- No discussion about ultrasound using frequencies above 5 MHz, hereby called high frequency.
- Disparity on the behaviour of ultrasound as cells degrade. Some state that ultrasound tends to a greater speed, whilst others found that ultrasound tends to a slower value.

Chapter 4

Introduction to Publications

This chapter introduces the publications that comprise the research in this thesis, including published articles and submitted manuscripts. It contains four sections, each covering an individual publication in order of thesis appearance. For each publication, the title and reference (where applicable), author contributions, and the paper's contribution to the literature are provided. Paper 1 addresses the literature review forming Chapters 2 and 3, whilst Papers 2, 3, and 4 correspond to Chapters 6, 7, and 8 respectively. All experiments performed in these papers followed the baseline setup shown in Figure 4.1. The batteries used in these studies were instrumented in the same configuration, as shown in Figure 4.2.

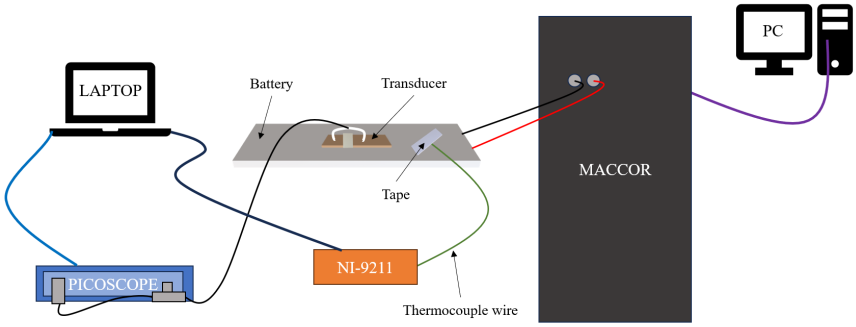

Figure 4.1: Baseline setup for all tests.

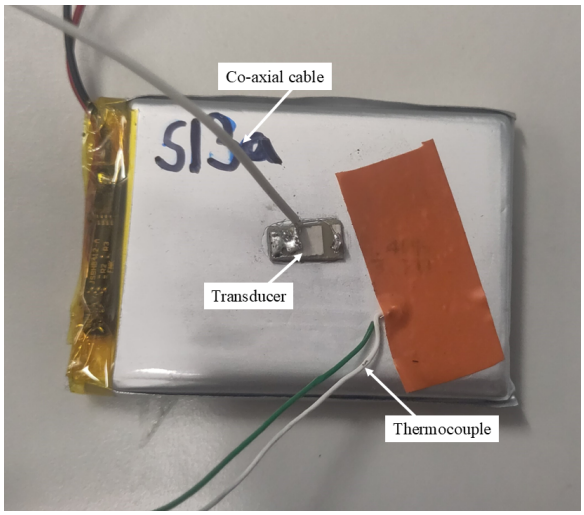

Figure 4.2: Example of instrumented battery with a thermocouple and a piezoelectric transducer.

4.1 Paper 1

Title

A review of ultrasonic monitoring: Assessing current approaches to Li-ion battery monitoring and their relevance to thermal runaway [178]

4.1.1 Publication Information

The first paper is published in the Journal of Power Sources which has provided confirmation that the published journal article "can be posted publicly by the awarding institution with DOI link back to the formal publications on ScienceDirect".

In this publication, I, the candidate, co-wrote the manuscript with Dr Royce Copley. The review was conceptualised by Dr. Royce Copley. I, the candidate, identified the progress of ultrasonic monitoring of lithium-ion batteries and the gaps found within in regards to temperature calibration. For the manuscript itself, I, the candidate, performed a critical analysis of the literature and wrote the findings of the review. Dr. Royce Copley assisted in the writing of the manuscript. Finally, the project received supervision from Prof. Rob Dwyer-Joyce and Prof Solomon F. Brown, with help editing and reviewing from Dr. Peter Bugryniec.

4.1.2 Paper Contribution

The first paper published focused on reviewing and identifying the current state of the art of ultrasonic monitoring of lithium-ion batteries. The review was split into three sections: ultrasonic monitoring of lithium-ion batteries; the detection and mechanisms of thermal runaway induction methods of lithium-ion batteries; and the use of ultrasound to detect and monitor when lithium-ion batteries were entering thermal runaway, with an emphasis on temperature.

The first section describes the use cases of ultrasound for charge and health monitoring. These variables were able to be detected using a variety of frequencies, though the majority are around 2-5 MHz. Different coupling methods and wave propagation modes all provided accurate state-of-charge (SOC) estimations through the use of cheap commercial sensors. The detection of internal failure mechanisms could be detected earlier with ultrasound than with more conventional detection methods. However, the identification of the failure mechanisms, and isolation in the case of multiple active mechanisms, was not viable with the state-of-the-art. The second section found that there have been advancements in the understanding of failure mechanisms that lead to lithium-ion thermal runaway. The cathode chemistry was found to be a source of instability in lithium-ion batteries. Other major factors of instability include C-rate, SOC and battery temperature. Thermal runaway onset can be detected, regardless of the abuse case. Some methods that were used for detection are not suitable for in-situ use, as they require knowledge that cannot be obtained during battery operation. The third section found that the temperature-charge relationship with the US signal needed to be decoupled in order to increase the

efficacy of estimating the state-of-charge and to assist in thermal runaway detection. There is contention in the literature on the effect of temperature on the ultrasonic time-of-flight (TOF) when measuring the SOC. There was data suggesting there was a greater impact from temperature at later time-of-flight ranges. The decoupling of temperature and charge has been started, but further tests need to be performed in order to confirm the usability of decoupling. In conclusion, this literature review provided an insight into the current advancements of ultrasonic monitoring of lithium-ion batteries, and provided a direction for future research to aim for. It was found that detection of SOC and state-of-health (SOH) was possible using ultrasound. There is a need to decouple the temperature effects from the acoustic response in order to improve charge estimations and improve detection of the onset of thermal runaway.

4.2 Paper 2

Title

Battery age monitoring: Ultrasonic monitoring of ageing and degradation in lithium-ion batteries [179]

4.2.1 Publication Information

The second paper is published in the Journal of Power Sources which has provided confirmation that the published journal article "can be posted publicly by the awarding institution with DOI link back to the formal publications on ScienceDirect".

In this publication, I, the candidate, co-wrote the manuscript together with Joshua Green, an undergraduate student on a summer research internship under my supervision. I, the candidate, led the experimental set-up, performance and analysis of ultrasonic detection of long term cyclic battery degradation. The manuscript was written by myself, the candidate, with assistance writing the introduction by Joshua Green. The work, shown in Chapter 6, describes the manner in which ultrasound can vary when detecting cell degradation, along with the fluctuation in ultrasonic TOF measurements that match the SOH fluctuations. The manuscript was supervised by Prof. Robert Dwyer-Joyce and Prof. Solomon Brown, with help editing and reviewing from Dr. Peter Bugryniec.

4.2.2 Paper Contribution

The second paper published focused on investigating the use of ultrasound to monitor ageing and degradation in lithium-ion batteries. The study consists of four parts: the use of TOF signal shifts to monitor SOH; the investigation and determination of the degradation mechanism; the relationship between normal use-case degradation and the ultrasonic time-of-flight; and the correlation of state-of-health fluctuations and the associated observations by the time-of-flight.

The first part briefly summarises the equations and physical phenomena that allow for the use of ultrasound to be used to monitor LIBs. Focus is given to the equations

governing the speed of sound of a material, the acoustic attenuation and the reflection observed as an acoustic wave reaches the interface of two heterogenous materials.

The second part analysed the degradation of two pouch cells subjected to 100 charge-discharge cycles at low C-rates to minimise temperature-induced degradation. This was confirmed through the comparison of temperature and SOH data, which was determined via Coulomb counting. Both cells showed measurable SOH loss, but the loss of SOH was not perfectly linear due to observations of noticeable fluctuations, largely in cell B. These fluctuations were linked to the regeneration phenomena. An incremental capacity analysis (ICA) was performed, and the resultant curves showed consistent in the voltage peaks to a higher voltage as the cells were aged, suggesting the dominant degradation mechanism was the loss of lithium inventory (LLI), likely due to SEI growth.

The third contribution established the relationship between the ultrasonic TOF signal and SOH degradation. The tracking of multiple peaks within the A-Scan revealed permanent TOF shifts that could be correlated to capacity fade. The strength of these correlations was confirmed via Spearman correlation coefficients, which all showed a value exceeding 0.8. Peaks that were recorded earlier in the capture window, which represent peaks that have less superposition and information of deeper layers, exhibited stronger and more consistent correlations with SOH than later reflections. These observations suggest that the TOF of the selected peak has an effect on the estimation accuracy of the SOH. The use of R^2 provided evidence that the linearity of the relationship between the TOF and SOH shifts is strong, with the earlier TOF peaks having a slightly stronger correlation than the later peaks. The identification of chemistry affecting the polarity of the permanent shift in the TOF was performed by comparing the experimental results to those of other studies.

The fourth section evaluated ultrasonic sensitivity to unexpected SOH fluctuations. TOF fluctuations observed per charge cycle aligned with SOH fluctuations, highlighting the capability for ultrasound to track irregularities of a battery's ageing behaviour in real time. Cross-correlation analysis revealed strong temporal alignment between TOF shifts and capacity anomalies, with the majority of selected peaks showing zero time lag between ultrasonic and electrochemical changes. This simultaneity provides evidence of ultrasound offering the potential for early warning diagnostics. Only one peak showed time-lag behaviour inconsistent with other measurements, suggesting occasional sensor-specific anomalies. Overall, the section demonstrated that ultrasound is capable not only of tracking long-term degradation but also of detecting short-term perturbations in capacity caused by reversible or irregular mechanisms.

In summary, the paper demonstrated that ultrasonic TOF shifts offer a reliable, non-invasive method for monitoring both progressive and irregular SOH degradation in lithium-ion batteries. The study confirmed that signal quality is influenced by peak selection and path length, that acoustic monitoring can detect both stable trends and transient anomalies, and that cathode chemistry may have an effect on the behaviour of the permanent TOF shift. These findings underscore the viability of ultrasonic sensing for advanced battery diagnostics and highlight the need for expanded datasets across chemistries and degradation modes.

4.3 Paper 3

Title

Acoustic Assessment of Lithium-Ion Batteries: Unravelling Temperature and Charge Contributions [180]

4.3.1 Publication Information

The third paper is published in the Journal of Power Sources which has provided confirmation that the published journal article "can be posted publicly by the awarding institution with DOI link back to the formal publications on ScienceDirect".

In this publication, I, the candidate, wrote the manuscript with supervision from Prof. Rob Dwyer-Joyce and Prof. Solomon F. Brown. In this research, I, the candidate, conceptualised a novel method to identify and decouple temperature and charge effects on ultrasonic monitoring of LIBs. I, the candidate, also performed the experimental set-up, performed the experiment and led the analysis of the data. Joshua Taylor assisted with the analysis and visualisation of the relationship between the TOF and temperature. Dr. Robert Milton assisted with the code used to perform the GSA analysis, and reviewed the visualisation of such analysis. The work, shown in Chapter 7, investigated the effect on temperature on the acoustic TOF measurements, as previous studies stated it was not a major factor with little to no evidence to support such a statement.

4.3.2 Paper Contribution

The third paper planned for publication focused on the combined and individual influences of temperature and SOC on the ultrasonic TOF in LIBs. A large portion of the research was dedicated to isolating the thermal and electrochemical effects to better understand their role in acoustic monitoring of LIBs. This was motivated by existing work in the field, where SOC had been considered the primary factor influencing TOF, while the effect of temperature was largely disregarded or stated to be negligible without strong supporting evidence.

The work introduced a novel experimental approach, using a thermal-SOC matrix to control and monitor the acoustic response across stable temperature and charge conditions. Through empirical testing, it was shown that temperature had a consistent and dominant effect on TOF, producing a strong positive linear correlation due to material expansion and density changes. SOC, by comparison, exhibited a negative linear effect, driven by lithiation-induced changes in the electrodes. The distinction between these two variables was made clear by tracking TOF shifts across multiple acoustic peaks and cells, revealing consistent behaviour, though with some variance in response magnitude between cells of the same batch.

A Global Sensitivity Analysis (GSA) using the first and second order Sobol' indices was then applied to determine the statistical independence between temperature and SOC effects. The results confirmed that temperature dominated the variance in

TOF, while SOC had a smaller, though measurable, contribution. The co-dependence between the two variables was shown to be statistically negligible. This finding was significant in demonstrating, for the first time, that temperature and SOC can be treated as independent inputs in acoustic interpretation of battery state.

The method and results presented here lay the groundwork for future decoupled ultrasonic monitoring of SOC and thermal behaviour without the need for additional sensing. This work was the first to apply a statistical framework such as a GSA to the acoustic monitoring of LIBs and has brought necessary attention to the importance of accounting for temperature.

4.4 Paper 4

Title

Acoustic Assessment of Lithium-Ion Batteries: Regression Modelling of Li-ion Battery State-of-Charge and Temperature

4.4.1 Publication Information

The third paper has been submitted for consideration as a research paper in Applied Energy.

In this publication, I, the candidate, wrote the manuscript with supervision from Prof. Rob Dwyer-Joyce and Prof. Solomon F. Brown. In this research, I, the candidate, along with Dr Robert Milton and Prof. Brown, conceptualised the research through my knowledge of the ultrasonic measurements and Dr. Milton's knowledge of machine learning (ML) and development. Dr. Milton developed the software used for the linear and Gaussian process regression while I, the candidate, completed the formal analysis and visualised the findings.

4.4.2 Paper Contribution

The fourth paper focused on the development of machine learning algorithms to estimate SOC and temperature of lithium-ion batteries solely through ultrasonic monitoring, removing the need for additional equipment such as thermocouples. The method was based on the findings of Paper 3, exploiting the independent influences temperature and SOC have on the ultrasonic signal through the use regression models. The study consisted of four main components: the comparison of linear regression (LR) and Gaussian process regression (GPR) approaches; robustness testing across multiple charge cycles; noise tolerance analysis; and investigation of ultrasonic peak formatting effects on model performance.

The first component established that LR outperformed GPR when generalising to independent test cycles, achieving mean absolute errors of 0.40% for SOC and 0.03°C for temperature during cross-validation. Contrary to expectations that complex non-linear models would be necessary, the simpler linear approach proved more robust, with

GPR showing signs of over-fitting to training data characteristics. The computational efficiency of LR also made it more suitable for embedded battery management system applications.

The second component demonstrated that the LR model maintained reasonable accuracy across sequential charge cycles, with performance varying between cycles. SOC estimation showed strong correlations for most cycles, whilst temperature estimation exhibited some variability. This highlighted the method's capability for short-term monitoring.

The third component confirmed the LR model's tolerance to Gaussian noise levels up to 15%, though error margins increased primarily at extreme SOC and temperature ranges. Interestingly, moderate noise injection (5-10%) improved some performance metrics, suggesting the baseline models were over-fitted and benefited from regularisation effects that would be seen in real-world applications.

The fourth component revealed the importance of peak selection and temporal sequence preservation. Using all available peaks, either with no change or averaging provided optimal performance, whilst using a limited number of peaks or randomising their order substantially degraded accuracy. This indicated that individual ultrasonic peaks contain distinct information that cannot be simplified without compromising estimation quality.

The work identified systematic biases in predictions, particularly at charge cycle boundaries, attributed to ultrasonic hysteresis effects from cell degradation that linear regression cannot adequately capture. The curved residual distributions suggested opportunities for non-linear modelling approaches to better represent the underlying ultrasonic-battery relationships.

The novelty of this work was the successful demonstration that a single piezoelectric crystal could provide accurate estimations of both SOC and temperature through machine learning, effectively creating an "ultrasonic thermocouple" that replaces physical temperature sensors. This proof-of-concept established the potential for simplified battery management architectures with reduced sensor requirements whilst maintaining critical monitoring capabilities. However, the research highlighted the need for larger datasets, validation across diverse battery chemistries, and development of non-linear models to address systematic biases before practical implementation could be achieved.

Chapter 5

Conclusion

5.1 Concluding Remarks

The growing popularity of lithium-ion batteries (LIBs) as both portable and stationary energy storage solutions cannot be overstated. This trend is driving increased demand across multiple markets, particularly in the electric vehicle (EV) sector with the number of EVs on the road to increase from 10 million in 2021 to upwards of 190 million by 2030 [181]. The stationary EES market is also expected to grow from 56 GWh as of 2021 to 2850 GWh by 2040 [182]. Such growth is largely motivated by the global push for decarbonisation, which seeks to replace traditional fossil fuel-based technologies across all sectors. Despite their widespread adoption, the understanding of the topic of LIB safety remains limited, leading to growing area of research. With this expected increase in growth, there must be a corresponding increase in safety and monitoring methods to reduce potential risks to both consumers and industry.

This is emphasised by the increase in the number of fires in personal light electric vehicles (PLEV), rising from two fires in 2017 to 211 in 2024 in the UK [183]. Of the e-bikes specifically, 75% of the fires were due to aftermarket conversion kits, and there is evidence suggesting that some fires were caused by incompatible chargers, rated up to double the voltage of the battery involved in the fire [183]. However, with regards to domestic battery energy storage systems (DBESS), the number of incidents has been consistent since 2011, whilst the number of DBESS products sold has increased [184]. This highlights an issue with no OEM manufacturers using adequate BMSs on their batteries, resulting in avoidable abusive usage of LIBs.

Ultrasonic monitoring offers a non-destructive, compact approach for detecting internal material changes in LIBs. This thesis investigates its application for measuring SOH and temperature. Thereby showcasing the broad versatility ultrasound can provide both research and industry. Throughout this work, ultrasound has been used in two distinct ways: first, to understand how the SOC, SOH and temperature affect the ultrasonic signal; and second, to reverse-engineering the signal to estimate arguably, the two most important battery parameters - SOC and temperature. In this thesis, three experiments have been presented, each presenting novel work that is either published or submitted for review to leading scientific journals.

The thesis provides an in-depth exploration of the mechanics behind this emerging methodology and incorporates both empirical and statistical analyses. The results suggest that ultrasonic monitoring can play an integral role of future battery management systems (BMSs), complementing existing techniques providing information on the internal mechanical structural changes alongside the already provided electrochemical information. This gives the BMS a more comprehensive dataset for battery monitoring and management.

5.1.1 Research Paper 1

Research Paper 1 investigated how acoustic signals evolve with battery degradation by performing long-term cycling on LIBs. A single bonded transducer, set up in a pulse-echo mode, was used during standard charge cycling tests of 100 cycles. A consistent shift in TOF was observed as the batteries aged, strongly correlating with

capacity loss, indicating a measurable decline in SOH.

The analysis revealed that the earlier peaks within the ultrasonic response were more reliable indicators of SOH likely due to the reduced superposition of internal reflections. A peak captured later in the response will be the culmination of multiple reflections from within the battery, providing more information than can be extracted, but also increasing the complexity of untangling such information. In addition, the study demonstrated that ultrasonic signals could track both long-term degradation and non linear per cycle SOH fluctuations, such as those caused by regenerative phenomena and manufacturing variations. It was suggested that the direction of permanent TOF shifts was influenced by cell chemistry, through a discussion of previous studies compared to the experiments performed.

5.1.2 Research Paper 2

Research Paper 2 explored the individual and combined effects of temperature and SOC on the TOF response in LIBs. By exposing batteries to thermal and charge cycles, a matrix of temperature and SOC states was produced. This was performed in a climate controlled environment, using a single transducer, pulse-echo mode setup. The study demonstrated that while both variables influence the TOF, temperature has a dominant and independent effect on the signal.

A positive linear relationship was observed between the TOF and the temperature, primarily caused by the thermal expansion, and change in stiffness, of the internal layers. In contrast, a change in SOC resulted in a negative linear correlation in TOF. This was driven by the change in material properties of the electrodes, mainly the negative anode, due to the lithiation/delithiation. Crucially, through the use of a Global Sensitivity Analysis (GSA), the codependence of temperature and SOC on the signal was shown to be statistically insignificant.

These findings demonstrate the predictable and consistent influence temperature and SOC have on the TOF. The linearity and statistical independence of these variables provide strong evidence that both can be independently estimated using only ultrasonic measurements, potentially removing the need for additional sensors in future battery systems.

5.1.3 Research Paper 3

Research Paper 3 demonstrated the first application of machine learning algorithms to ultrasonic LIB monitoring, investigating whether regression models could accurately estimate SOC and temperature using time-of-flight measurements. Linear regression (LR) and Gaussian Process regression (GPR) were compared across multiple training and testing charge cycles with varying noise levels and peak formatting approaches.

The study revealed that the LR outperformed the GPR when generalising to independent test cycles, achieving strong correlations and low error margins for both SOC and temperature estimation. This finding was counter-intuitive, as the GPR was expected to better capture non-linear ultrasonic-battery relationships, and performed better during cross validation. The linear model demonstrated robust performance

across consecutive charge cycles, though systematic bias was observed at extreme charge states due to non-linear behaviour.

Peak formatting analysis showed that maintaining the peak order had a significant effect on the estimation, with randomising the order of all available peaks producing notably worse accuracy than other formats, such as selecting a limited number of peaks from different time points in the ultrasonic response. The method proved tolerant to multiple Gaussian noise levels, with moderate noise injection seeing improvement some estimation metrics likely due to regularisation effects. These findings demonstrate that machine learning can be adopted to not only track battery state parameters *in-situ* for post use analysis, but estimate multiple parameters, potentially simplifying BMS instrumentation by reducing equipment requirements.

5.2 Limitations and Future Work

The work presented in this thesis developed methods that used MLs and produced experimental data that provided insightful results. The findings of this work have successfully answered the research questions proposed in Section 1.2. In doing so, more questions and avenues for future research presented themselves that can further improve the utilisation of ultrasonic monitoring of LIBs.

5.2.1 Research Paper 1

The work presented in Research Paper 1 showed a consistent correlation between TOF shifts and the degradation of LIBs. This work was performed on two pouch cells that were from the same manufacturing batch. This limited the conclusions of the results. The battery-to-battery variation, despite being from the same batch, was likely due to transducer bonding or manufacturing variation. The lack of temperature control resulted in ambient temperature variation alongside the internal heat generation of the charging/discharging, adding an additional variable affecting the battery degradation. The single cathode chemistry limited the conclusion of the cathode having an effect on the TOF shift direction to only an implication, despite the comparison to previous research.

In order to further the findings of this work, repeats of this experiment should be performed. This should be done with various cathode chemistries, and a larger number of batteries being cycled in tandem. This will provide results explaining the difference in chemistries within the literature, and will allow for the assessment of the generalisation or deviation of the observed trends. Performing this experiment in a temperature control chamber would reduce the environmental impact on the battery degradation. Extending the length of the test to end-of-life would observe whether the ultrasonic behaviour is consistent as the degradation persist. The addition of post-mortem analysis would confirm the degradation mechanism of the batteries, potentially associating certain mechanisms to behavioural differences in the TOF measurements.

5.2.2 Research Paper 2

A large part of this study was dedicated to the effects of temperature on the ultrasonic signal, specifically the TOF, alongside the SOC. The focus on temperature was chosen due to the lack of interest shown within the literature. The work presented in Research Paper 2 established the individual and combined effects that SOC and temperature had on the TOF measurements. Notably, the dominance temperature had, as well as the lack of combined influence on the TOF, leading to the work conducted in Research Paper 3.

All measurements were conducted using discrete SOC steps and a fixed temperature profile per SOC state. This limited the resolution of the dataset, and excluded dynamic charging conditions seen in real-world use. The chemistry of the batteries, being purely NMC, prevented evaluation of whether the observed linearity and independence between variables holds across different cathodes. Additionally, the magnitude of TOF changes with temperature and SOC varied between batteries from the same batch, indicating possible manufacturing variations that may reduce confidence in the reproducibility of the results.

Future work should apply the GSA to data collected from a standard charge cycle, within a temperature control chamber. This would determine whether the statistical independence of temperature and SOC effects on the ultrasonic response is universally valid. Similarly to Research Paper 1, repeating this experiment with different chemistries would allow for the comparison of the ultrasonic behaviour; to confirm if the linearity and magnitude of the relationships between SOC, temperature and TOF is universal or not. Performing this with greater temperature and charge resolution would provide greater granularity and insight.

5.2.3 Research Paper 3

The machine learning approach presented in Research Paper 3 showed promising results for ultrasonic estimation of multiple parameters of LIBs, but several limitations constrained the broader applicability of these findings. The study was conducted on only two cells from the same manufacturing batch and chemistry (NMC), limiting conclusions about generalisation across different battery types and manufacturers. The training and testing cycles were sequential, providing limited insight into long-term model stability as batteries undergo significant degradation over extended cycling.

The systematic bias observed in residual analysis, particularly the curved distribution indicating consistent over- and under-estimation at different SOC ranges, suggests that linear regression oversimplifies the non-linear aspects of relationships between ultrasound and the battery. The pronounced hysteresis effects, which has been observed to increases as cells undergo cycling within literature, indicated more complexity in the relationship that may not be accurately modelled with a simple linear regression.

Future work should validate the model across larger battery populations with diverse chemistries and manufacturing batches to assess generalisation capabilities. Investigation into non-linear regression models, such as neural networks, could address

the limitations identified in the residual analysis. Testing on charge cycles further removed temporally from the training data would assess long-term model stability and robustness to battery degradation effects. Additionally, investigation of dynamic charging conditions rather than controlled laboratory cycles would better reflect real-world operating scenarios.

Chapter 6

Battery age monitoring: Ultrasonic monitoring of ageing and degradation in lithium-ion batteries

Abstract

Lithium-ion batteries, widely used in modern technology, degrade with use, leading to reduced capacity and power output. Monitoring and diagnosing this degradation is essential, and ultrasound has emerged as a potential tool because of its low cost and non-destructive nature. Studies have noted changes in ultrasound behaviour with battery degradation, making it potentially valuable for tracking battery health. However, the behaviour of ultrasound as a battery degrades has been an issue within studies. This paper explores the relationship between state-of-health (SOH) loss and permanent ultrasonic signal changes over 100 charge cycles. A strong correlation was found between SOH reduction, observed to be caused by the loss of lithium inventory (LLI), and shifts in ultrasound signal responses. The analysis of individual peaks within a single acoustic signal showed consistent shifts in time-of-flight (TOF), often trending toward shorter TOFs. In particular, the rate of degradation was not entirely linear, with fluctuations observed across the cycles. These findings suggest that ultrasound can effectively monitor the rate of lithium-ion battery degradation. Future work could expand on these results by inducing varied degradation conditions and cathode chemistries to determine specific TOF shifts, enhancing detection methods for different degradation mechanisms in lithium-ion batteries.

Keywords: Lithium-ion battery; Battery Degradation; Ageing mechanism; Incremental capacity; Ultrasonic acoustics

6.1 Introduction

6.1.1 Battery SOC and SOH

Lithium-ion cells have become commonplace in handheld electronics, such as mobile phones and laptops, and in larger energy storage, such as electric vehicles and grid storage since their commercialisation in the 1990s [3–5]. This can be attributed to their high energy density, high operating voltage, no memory effect, and small levels of self discharge [7, 185]. However, there are limitations with this technology: stress-induced material damage, capacity fade, and thermal instability which can lead to thermal runaway. Optimal use will provide a finite number of charge/discharge cycles, and nonoptimal use will lead to faster degradation of cell life and an increased rate of loss of cell performance [186].

In order to ensure safe, efficient usage of lithium-ion cells, battery management systems (BMS) have been developed and deployed. A BMS can estimate the state-of-charge (SOC) of a lithium ion cell, which is the ratio of the current cell capacity to the maximum capacity of the cell. This can be estimated using measured values, such as Coulomb counting and open circuit voltage lookups, or using modelling approaches such as electrochemical circuit models and neural networks [49,187]. Other examples of common BMS methods include: the equivalent circuit model, utilising the open-circuit voltage, ohmic internal resistance, and resistor-capacitor network to model a cell [4]; and support vector machines, which use machine learning algorithms to estimate SOC [49]. These approaches each have their individual benefits and drawbacks: experimental methods require less computational effort and allow easier estimations than modelling approaches, whilst having greater estimation errors [51].

BMSs are capable of providing state-of-health (SOH) estimates based on comparisons between current and past cell performance [178], or by measurable parameters and comparisons to electrochemical models [51]. These parameters include, but are not limited to, internal resistance, terminal voltage, and self-discharge resistance [188, 189]. However, all these methods use values that measure the electrical state of the cell and do not provide accurate measurements of the internal physical state of the cell [190]. Hybrid approaches, involving both empirical data and models, can greatly improve SOH accuracy [191], but these require large datasets and greater computing power.

Estimating the SOH of a cell is a complex task. Several definitions and methods are being deployed for SOH estimations. See ref [192] for further details. The SOH can also be estimated as a function of open circuit voltage (OCV), incremental capacity analysis (ICA) curves, [193], and based on the internal resistance of the cell [194]. One of the most common methods to estimate the SOH is by coulomb counting [51]. It is defined as the ratio of the maximum capacity at cycle t, Q_t (A h), to the original maximum capacity, Q_0:

$$SOH = \frac{Q_t}{Q_0} \cdot 100\% \tag{6.1}$$

This allows for the capacity fade of the cell to be measured, which can be caused by multiple physical and chemical reactions. These are outlined in the supplementary material in Figure S1.

6.1.2 Ultrasonic Non-Destructive Monitoring of Lithium-ion Batteries

Recently, there have been many studies using ultrasound to measure internal changes *in-situ* in order to estimate the health and performance of lithium-ion cells [90,94–96,99]. Ultrasound is defined as sound with a frequency above the human hearing range, normally around 20 kHz [61]. It is a well-developed non-destructive technique used for detection of surface and subsurface changes in bodies of interest. Piezoelectric transducers are excited to generate ultrasonic pulses that travel through bodies of interest and get partially reflected at interfaces, such as between two materials, a crack or an air bubble. In addition to monitoring, ultrasound has been used to improve the leaching of active materials from spent LIBs [195, 196] which exposes the cells to high powered, continuous wave. The improvement in the electrochemical performance of LIBs via ultrasound has also been investigated by subjecting cells to a continuous low power acoustic energy [197].

The relationship between ultrasonic signals and battery SOH is complicated when considering the numerous side reactions that can affect the SOH. Side reactions occur almost everywhere because of the electrochemical nature of LIBs, both during normal and abusive conditions. Such reactions include lithium plating, SEI formation and growth, gassing, electrode delamination, and porosity [198, 199]. Post-mortem analysis has confirmed these reactions to be detected, however there is an issue of decoupling these effects for more accurate detection. If multiple reactions occurred within a cell, the ultrasonic response would not be able to discriminate between them.

When LIBs are cycled, there is a cyclical, reversible change in the TOF through the cell that correlates with the SOC. As the cell is charged, the TOF decreases; as the cell is discharged, the TOF increases. There are different reports on the direction of the permanent TOF shift in the literature. The TOF also experiences an non-reversible shift as the cell degrades, which is independent of the SOC. This overall TOF shift is related to the SOH (distinct from the cyclical TOF change driven by the SOC) and is hereafter called the permanent shift. The permanent shift has been observed with different acoustic frequencies, from 90 kHz to 2.25 MHz. The direction of the permanent shift varies within the literature; a permanent shift to a shorter TOF was observed by [95, 200], while a longer permanent shift was observed by [94, 96, 201].

Using a low C-rate reduces the self-heating temperature of the cell due to ohmic heating (heat from the resistance of lithium-ions moving through the electrolyte) and allows for even lithium-ion deposition dispersion [202]. This allows for a more isolated look at degradation methods caused by chemical physical reactions as a result of normal operation rather than as a result of extreme external factors. As stated in [203], some degradation methods occur outside the safe operating conditions, such as cathode degradation at relatively high temperatures (45 °C) [204] and electrode damage and potential rupture at high C-rates [205].

In this work, temporally resolved ultrasonic TOF measurements are performed in lithium-ion cells to investigate the effect of cell degradation on the permanent shift of the acoustic signal. The cells were cycled for over 100 cycles at a low C-rate within the manufacturer's voltage limit to mitigate pronounced degradation whilst

ageing. The cycle number was selected as the cells were rated for 301 cycles by the manufacturer, so the effect of cell ageing is accelerated. This allows for a comparative exploration into ageing and the effects on the ultrasonic response. Multiple reflections were analysed to investigate and compare correlations and permanent shift directions between peaks with different TOF within the A-Scan.

6.2 Experimental

6.2.1 Battery Instrumentation

This work involved testing two nominally identical cells, cell A and cell B. The cells were commercial pouch lithium-ion batteries 2000 mA h with consisted of a cathode with NMC chemistry and a graphite anode (stock number 125-1266 RS Pro, London, England) with dimensions of 63 x 43.5 x 7 mm. The cells were purchased at the same time, from the same manufacturing batch and were manufactured on the same day. The cells were instrumented with a single ultrasonic piezoelectric transducer of dimensions 10 mm x 5 mm with a central frequency of 2 MHz. (DeL Piezo Specialties, LLC, FL, US), which were bonded to the cell surface using a commercial adhesive. The centre frequency influences the penetration depth, signal attenuation and wave sensitivity. Based on previous studies [7, 82, 206], 2 MHz was determined as the most suitable frequency. Each cell was instrumented with a single transducer that will act as both transmitter and receiver. A thermocouple was attached to the surface of each cell to record the surface temperature.

6.2.2 Ultrasonic Pulsing and Receiving

The acoustic response was obtained using a Picoscope 5444D oscilloscope, operated by proprietary Picoscope 6 software (Pico Technology, Cambridgeshire, UK). The Picoscope acted as both a function generator and an acoustic DAQ. The signal was produced by, and the reflections were captured by the Picoscope.

The acoustic signal was controlled through a bespoke virtual instrument (VI) built in LabVIEW, utilising the Picoscope 6 software. This VI also allowed recording of the surface temperature along with the ultrasonic signal, both of which were recorded once a minute. Each capture lasted for one second and recorded 50 pulses, of which the average was taken and used for analysis. The resolution of each pulse was 3900 discrete measurements. This provided a sampling interval of 7.7 ns over a time window of 30 µs. The source wave for each pulse consisted of three sinusoidal waves, with an amplitude of $\pm$ 2 V, that transmitted through the cell and were reflected back to the transducer once they reached the opposing face of the cell. The surface temperature of the cells was monitored using a K-type thermocouple. The temperature was recorded using the NI-9211 temperature input module (National Instruments, TX, US).

Both cells were cycled at the same time. To capture the acoustic data from both cells, a bespoke multiplexer was used to connect the cells to the Picoscope. This allowed a single Picoscope channel to be used. A sequence table was created to control

the acoustic inputs and the parameters of the recorded response. As the cells were connected through a single channel, cells were recorded sequentially. The VI was also designed to receive multiple thermocouple inputs at the same time.

6.2.3 Battery Cycling

The cells had a maximum charge rate of 0.5 C and a maximum discharge rate of 1 C and were cycled at 600 mA h (0.3 C) using a MACCOR Model 4600A Automated Test System (MACCOR, OK, US) in a constant current-constant voltage (CC-CV) cycle. Internal heat generation has been shown to have a dependency on the C-rate, with higher C-rates resulting in greater heat generation [207]. An increase in heating can cause accelerated ageing in LIBs [208]. The focus of this work is to investigate degradation through internal mechanical and structural changes with reduced influences from controllable factors such as C-rate and temperature. Ultrasonic equipment can be sensitive to temperature, and the exploitation of this is called ultrasound thermometry [209]. To reduce the influence of temperature on the ultrasonic response to ensure that cell ageing has the greatest influence, the C-rate for this work was kept low. The charge cycle saw the cells charged between 3.0 V (0% SOC) and 4.2 V (100% SOC). The upper and lower voltages were held constant until the current dropped below 60 mA h (0.03C) (see Table 6.1).

Phase	Mode	Voltage (V)	Current (mA)
Charge	Constant current	3.0 to 4.2	600
	Constant voltage	4.2	600 to 60
Discharge	Constant current	4.2 to 3.0	600
	Constant voltage	3.0	600 to 60

Table 6.1: Charge cycle parameters.

6.2.4 Signal Processing

The charge data, surface temperature, and acoustic response were recorded every 60 seconds throughout the test. The reflected signal (A-Scan) of cell A at the beginning of the test is shown in Figure 6.1a. The acoustic signal contained information such as the TOF and the signal amplitude. The charge data includes information on the voltage, current and estimated battery capacity. To correlate the acoustic data with the charge and temperature data, a method called peak tracking was employed. In Figure 6.1a, the first seven peaks are related to the pulse generated that created the acoustic signal and the associated damping. These peaks are highlighted by the blue shading. The other peaks relate to reflections or reflected signals - acoustic signals that have travelled through the cell and returned to the transducer. As lithium ion cells have multiple layers, either rolled or layered, there are many interfaces. The cells used in this work were purchased from the same batch at the same time. Due to the nature of cell manufacturing, there may be differences between the cells.

Each interaction between the acoustic signal and an interface results in a part of the signal being reflected in the original medium and a part transmitted in the new medium. Therefore, some signals can get trapped reflecting between two interfaces, whilst some of the signal travels through the entirety of the cell. The signal detected by the transducer is a superposition of all the reflections that have split within the cell. A single interface cannot be related to a single peak as a result of this, as the number of interfaces that are superimposed in the signal increased as the TOF increased. Therefore, the highest peak is unlikely to have the best correlation, as investigated by [7]. In order to ensure that the peaks analysed provide the strongest correlation to the loss in SOH, a peak tracking method was employed.

Peak tracking involved selecting individual peaks and recording the respective TOF and amplitude change throughout the cycles [7]. This is done by creating windows centred on the peaks representing a set time either side of the selected peak in the TOF domain. Between each data point, the greatest amplitude is found within the window range is found, and the windows were shifted to maintain the original set distance from the new peak. This is repeated throughout the dataset, resulting in a spectogram of the A-Scan focused on the peak in question. This method allowed for the identification of the peak that had the strongest correlation with the internal battery changes.

Selecting multiple peaks individually creates the capability to compare the results of individual peaks across the A-Scan. In doing so, two peaks were selected for each cell. For cells A and B, these are Short A, Long A, Short B, and Long B, respectively. The naming convention is related to where in the A-Scan (i.e. the TOF) the peaks were selected. Short A and Short B were selected from earlier peaks in the A-Scan, and Long A and Long B were selected from later peaks. The reason for this is due to the internal structure of the cells tested. The cells have a prismatic winding construction which results in spacing in the centre of the cell. This spacing is enough to create an acoustic barrier and was confirmed by Copley et al. when a genetic algorithm was able to accurately predict the internal construction of the cell [210]. The algorithm identified an irregularity in the centre of the cell, which corresponds to a prismatic winding construction. This spacing resulted in a proportion of the signal being reflected. The resultant reflected signal is a half-reflection in which the signal has only travelled back and forth through half the cell. As such, the second reflection was a superposition of the half-reflection after two passes, and the full reflection having made one pass.

Figure 6.1a shows the A-Scan of cell A. The two peaks, Short A and Long A, are highlighted with the dotted lines. The green shaded area identifies the first two reflections, or the first half-reflection and first full reflection, as described earlier. The blue shaded area therefore emphasises the third and fourth reflections. The change in the TOF of peak Long A, highlighted in Figure 6.1a, over all the charge cycles is shown in Figure 6.1b. The colour of the plots change from yellow to blue as the signal amplitude decreases. The red line denotes the location of the peak that is being tracked within the peak window of Long A. In order to improve the signal-to-noise ratio of the signal, the selected peaks were denoised using wavelets via the wdenoise function in MATLAB.

What can be seen in Figure 6.1b is a cyclical increase and decrease in ToF alongside

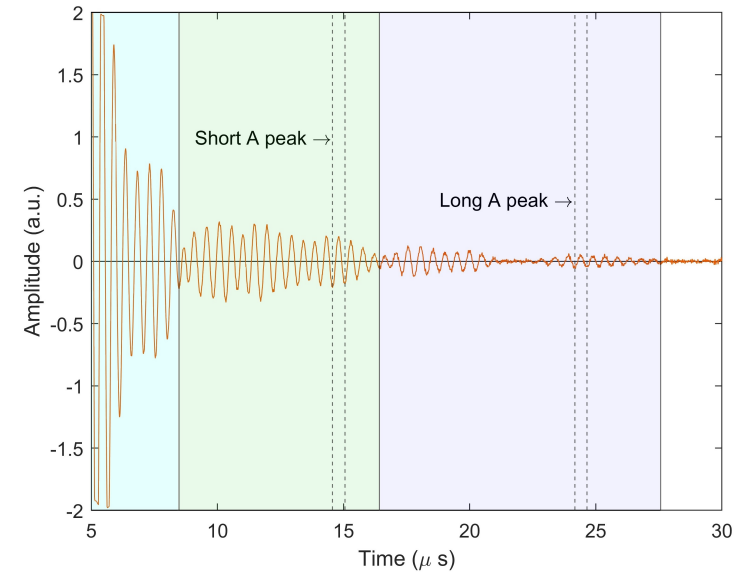

(a)

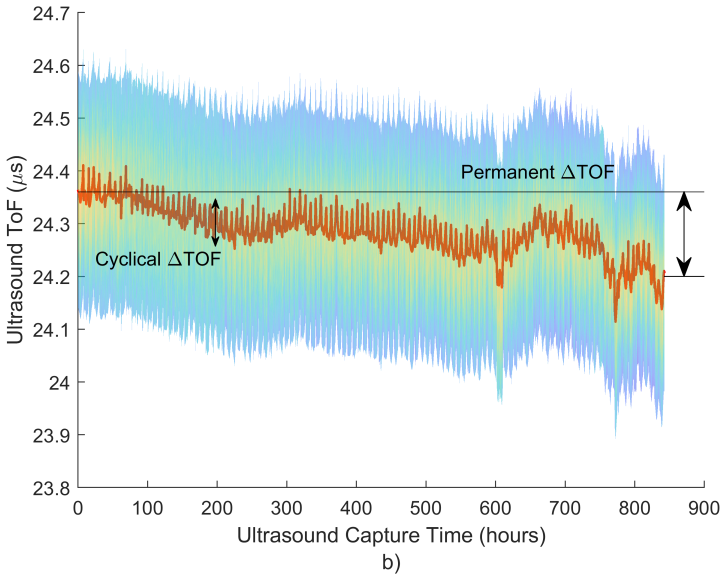

b)

Figure 6.1: a) A-Scan of Cell A, with the window around peaks Short A and Long A shown with dashed lines. The green and purple shaded areas highlight the first and second sets of half and full reflections, respectively. the blue shaded area shows the initial pulse and the associated attenuation. b) TOF of peak Long A using peak tracking. The colour of b) represents to amplitude of the peak capture area. The red lines in b) highlights the peak in the range; the greatest value within the peak capture area.

a general trend to a shorter TOF. The cyclical change is related to the charging cycle of the cell, as lithium-ions intercalate and deintercerlate into and out of the electrodes. This TOF variation is therefore related to the SOC of the cell. The general trend to a

shorter TOF (or the permanent decrease in TOF) is related to the loss in SOH of the cell. This relates to non-reversible changes in the cell such as LLI or LAM. The kink seen around 600 hours into the test will be discussed in the next section.

Tracking single peaks allows for direct comparison between the battery, temperature, and acoustic data. Figure 6.2 shows this comparison for four charge cycles for cell A, using the same peak in Figure 6.1. There is a clear correlation between the acoustic and battery data, as the TOF (Figure 6.2e) shows a decrease as the stored charge (Figure 6.2a) increases, whilst the inverse is true for the amplitude (Figure 6.2d). The temperature is shown to exhibit cyclical behaviour, as the temperature increases significantly as the cell nears the end of the discharge stage, followed by a sharp decrease as charging begins.

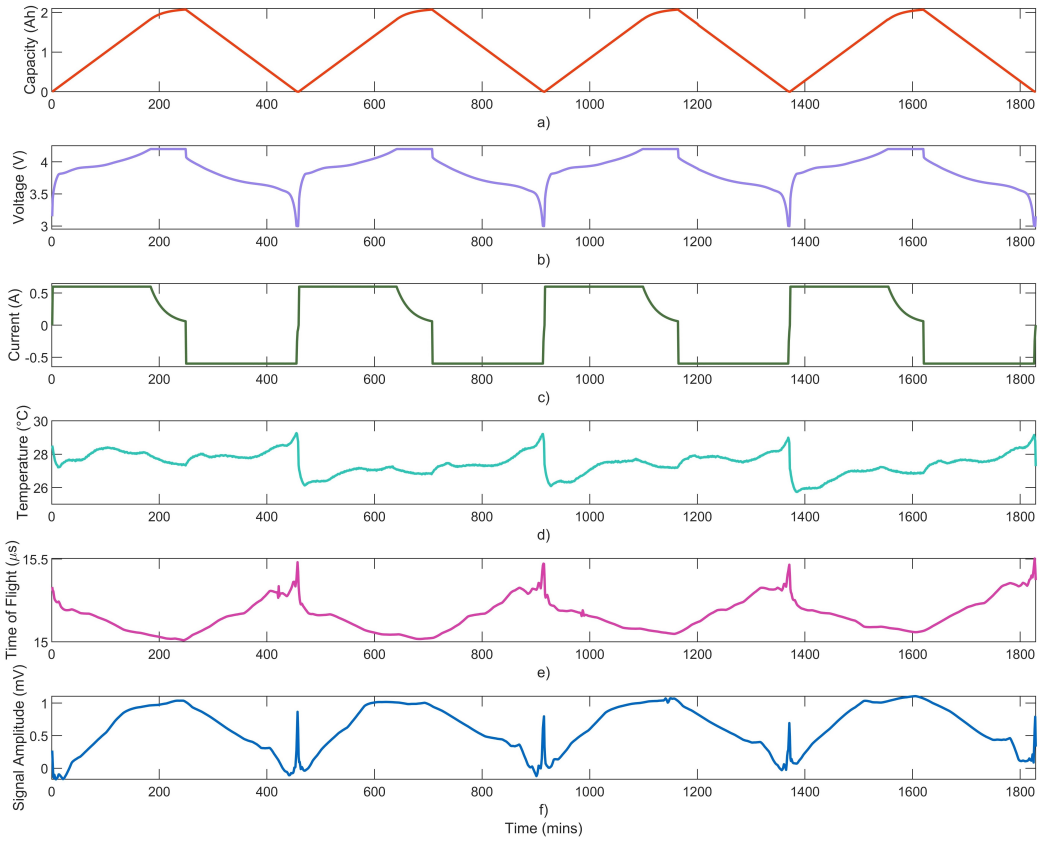

Figure 6.2: Change in a) capacity, b) voltage, c) current, d) temperature, e) time-of-flight over four cycles and f signal amplitude. The amplitude and time-of-flight are from peak Short A. A cyclical response from the acoustic signal and the temperature can be seen that correlates with the charge cycles of the cell.

6.3 Results and Discussion

6.3.1 Generated ultrasonic signal generated by a pouch cell

The amplitude of the reflected wave as it varies with time (known as an A-Scan) is recorded. Figure 6.3 shows an A-Scan response from one of the lithium-ion cells used in this work. The 2Ah cells used in this work are the same cells used by Copley et. al, which were described to contain around 15 "unit cells", each containing multiple interfaces [210]. The authors described a "unit cell" as a repeating pattern of battery components consisting of two anode layers, two cathode layers, two current collectors, an electrolyte, and two separators. Each interface acts as an acoustic reflector, and the resultant A-Scan is a superposition of all internal interfaces within the body. For this reason, the peaks seen in Figure 6.1 do not correspond to individual layers or structures within the cell, but rather to a superposition of many layers and structures. The speed a longitudinal ultrasonic pulse travels through a medium, c (m s^{-1}), is defined by:

$$c = \sqrt{\frac{K + \frac{4}{3}G}{\rho}} \tag{6.2}$$

where E (GPa) is the elastic modulus of the material and ρ (kg m^{-3}) is the material density. As lithium-ion cells charge and discharge, the material properties of the electrode change based on the amount of lithium (de)intercalated within. This influences how the ultrasonic signal travels through the cell, resulting in the difference seen in Figure 6.3. The A-Scan can vary in two ways: the time-of-flight (TOF) and amplitude. The TOF is the time it takes for an ultrasonic signal to travel through a medium and be received by a transducer, and for a homogeneous material, with known speed and thickness, is calculated using the relationship between the speed of sound c, distance d and TOF:

$$TOF = \frac{d}{c} \tag{6.3}$$

The use of a pulse-echo setup in this work means the distance travelled by the reflected signal is 2 d, as it must make a round trip to and from the transducer. The TOF in this work was measured using the electrical signal generated by the excitation of the transducer once the reflected wave returned. A cell is not a homogeneous material, with different materials for the electrodes, current collectors, separator and electrolyte, the travel time of the wave will fluctuate with changes in the speed of sound described in Equation 6.2.

The signal amplitude is the intensity of the acoustic wave. The signal attenuates as it travels through a medium, due to a combination of scattering and absorption. This attenuation results in the decay of the signal amplitude. Scattering is the result of heterogeneity in a material. This could be caused by flaws within a single host medium, or the sudden change in acoustic impedances found at medium interfaces. Absorption is the conversion of acoustic energy into heat by the host medium. When

only accounting for these factors, an exponential function can be used to describe the attenuation of an acoustic signal:

$$A = A_0 e^{-\alpha d} \tag{6.4}$$

where A_0 and A are the initial and final acoustic amplitudes, respectively, α is the attenuation coefficient and d is the distance travelled by the wave. As seen in Figure 6.3b, the A-Scan shows that the time-of-flight (TOF) increases as the SOC drops, that is, the peaks shift to the right of the A-Scan. The amplitude of some peaks show an increase, while some show a decrease in amplitude with a change in SOC.

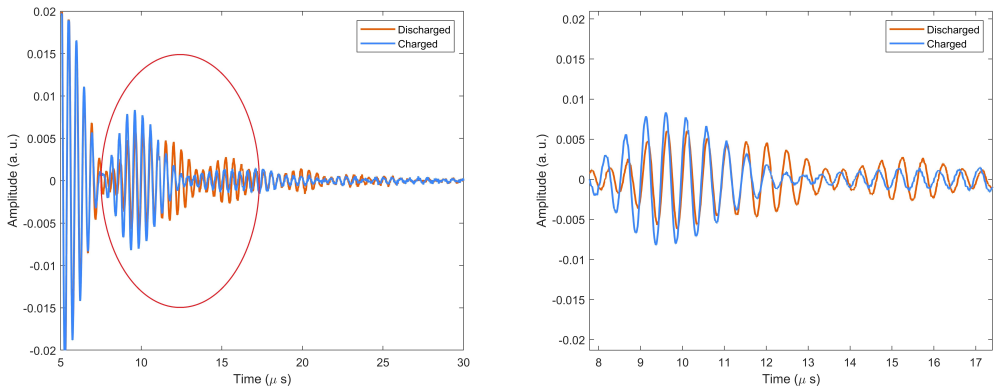

(a) (b)

Figure 6.3: a) An A-Scan of one of the tested cells at full charge (blue) and full discharge (orange). The A-Scan section in the red circle is shown in b) to isolate the first two reflections.

The reflection at an interface is described by the reflection coefficient R, which is the ratio of the reflected wave back divided by the incident wave. The reflection coefficient depends on the acoustic impedances of the two media, and is determined by:

$$R = \frac{Z_2 - Z_1}{Z_2 + Z_1} \tag{6.5}$$

where Z (Pa s m^{-1}) is defined by:

$$Z = \rho c \tag{6.6}$$

where ρ is the density (kg m^{-3}) and c is the speed of sound (m s^{-1}).

6.3.2 Cell degradation

The SOH of both cells, obtained using Equation 6.1, is shown in Figure 6.4. It should be noted that the decline is not perfectly linear, as there are SOH fluctuations present in both cells. Batteries such as lithium-ion can suffer from self-charging when certain

conditions are met, causing a sudden, temporary increase in available capacity in the next cycle. This is known as regeneration phenomena, which can affect the accuracy and precision of SOH estimations [211–213]. The significance of fluctuations due to regeneration phenomena on the ultrasonic response will be explored in Section 6.3.4. Cell B underwent more significant fluctuations than cell A, with a significant drop around 20 cycles. Both cells were tested in tandem using the same protocol as described in Table 6.1, reducing the probability of environmental influences on the cells.

Figure 6.4 also shows the change in temperature of cells A and B during the test. The dotted lines represent the temperature at which the cells were fully discharged, and the solid lines represent the fully charged temperature. The fluctuations at the start of the cycle for cell B, and the drop at cycle 81 in cell A, can be seen to replicate in the temperature readings. The temperature trends outside these isolated points follow the non-linearity of the loss in SOH, but not to the same extent. This is because internal heat generation depends on the final capacity of the cell. A cell that is closer to fully charged or fully discharged will generate more heat [214].

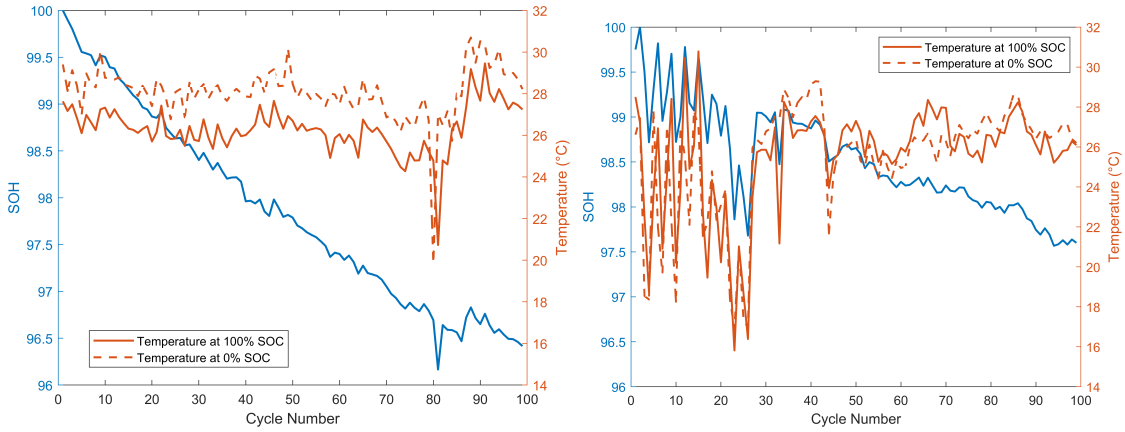

Figure 6.4: Change in temperature of a) cell A and b) cell B at 0% SOC (dotted line) and 100% SOC (solid line) against the SOH drop.

Aside from these fluctuations, the temperature of the cells does not show a permanent trend that matches the SOH drop - the temperature range remains consistently within 24 - 30 °C for both cells. The regeneration phenomenon is reflected in the temperature, as fluctuations are seen in both fully charged and fully discharged temperature readings. As the testing was not performed in a temperature controlled environment, variations are also a result of slight room temperature changes. In a semi-empirical degradation model by [215], the main mechanism of battery degradation in a cell between 25 - 30 °C is the SEI layer growth. This growth is caused by an interaction between the electrolyte and active lithium-ions, leading to the formation of a surface layer film on the anode. This process consumes lithium ions, reducing the effective capacity of the cell over time [216, 217], while increasing internal resistance [218].

In order to understand which driving forces are causing the cell degradation,

incremental capacity analysis (ICA) curves of the cells were employed. This analysis involves the differentiation of the capacity with respect to the voltage, allowing voltage plateaus to be highlighted as peaks, as defined in Equation 6.7.

$$\frac{dQ}{dV} = \frac{Q_t - Q_{t-1}}{V_t - V_{t-1}} \tag{6.7}$$

$$Q_t = \int_0^t I \, dt \tag{6.8}$$

where Q_t and V_t are the capacity and voltage at time t, and I is the current. Changes in these peaks were evaluated as the number of cycles increased. Through these equations, plateaus in the voltage curve are converted into peaks in the ICA plot [219]. A rolling average with a window of 5 steps was applied to smooth the ICA curves. Figure 6.5 shows the ICA plots of the two cells tested. Two peaks corresponding to voltage plateaus were observed. These peaks seen during charging relate to graphite intercalation and the crystal structure change of the cathode, respectively [220]. As such, the peaks are strongly dependent on the cell chemistry [221].

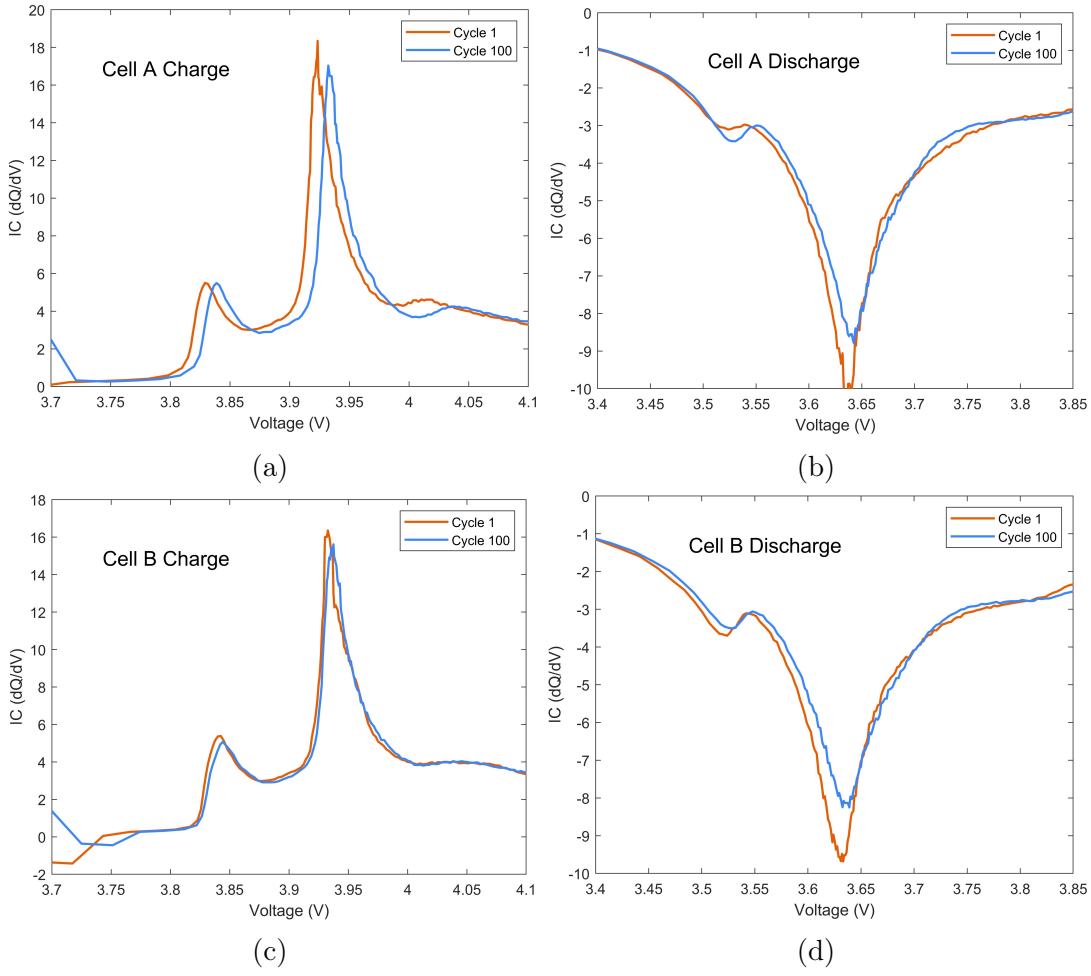

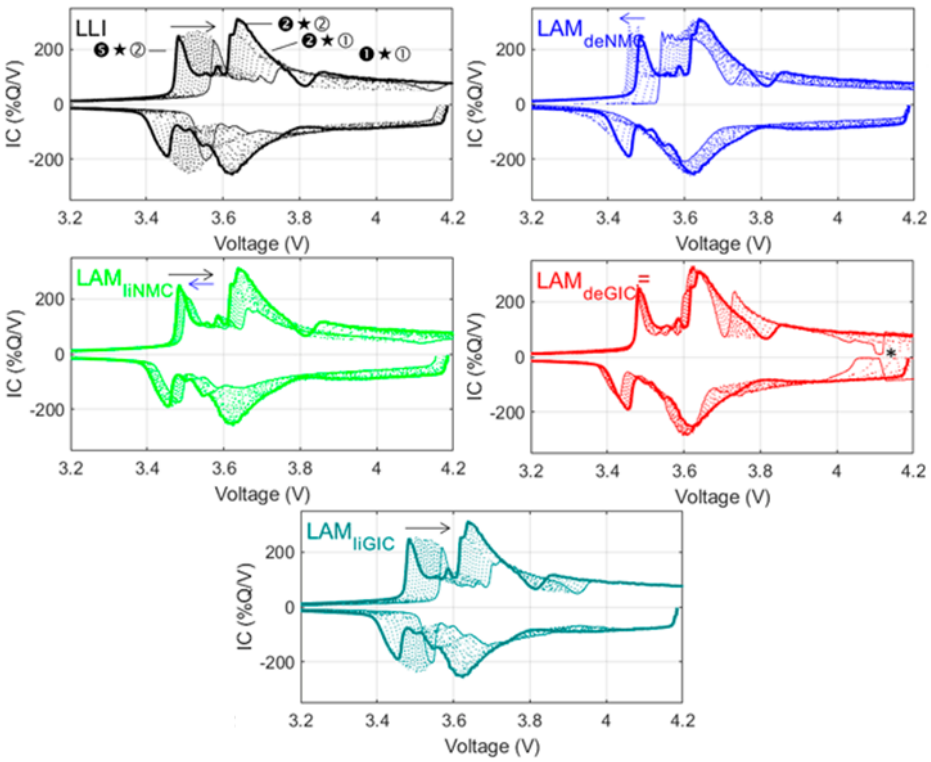

(e)

Figure 6.5: The ICA of cell A during a) charge and b) discharge. The ICA of cell B is represented in c) and d). All plots show a trend to a higher voltage as the cell ages. e) shows how the ICA of an NMC/graphite cell will change when influenced by different degradation methods. deNMC = delithiated cathode; liNMC = lithiated cathode; deGIC = delithiated anode; liGIC = lithiated anode. Image adapted from [222], licensed under CC BY 4.0. Modifications were made to only include graphs related to LLI and LAM changes.

For charge (Figure 6.5a and 6.5c) and discharge (Figure 6.5b and 6.5d) for both cells, the ICA peaks trend to a higher voltage as the cells are cycled i.e. the peaks shifted to the right. According to [222], this shift can be used to ascribe the main driving mechanism for the capacity drop as LLI as seen in Figure 6.5e. The increase in voltage is due to the incomplete lithiation of the anode as an increasing number of lithium ions are consumed by parasitic reactions, such as the SEI growth. The voltage limits were kept the same (3.0 - 4.2 V) throughout the tests.

As the SEI grows, more lithium ions are consumed, which has the effect of reducing the lower potential regions of the anode. This results in incomplete lithiation during charging, resulting in a higher potential at the end of charge. To maintain the upper voltage limit, the cathode will have to compensate for a higher potential. The same is then true for the discharge, as the cathode will experience incomplete lithiation at the end of discharge to maintain the lower voltage limit [223]. The amplitude of the ICA curve peaks also consistently decreases as the cell ages, further indicating that the

lithiation of the electrodes is reduced due to LLI [224].

This degradation phenomenon agrees with the literature on cell degradation methods of NMC / graphite cells (see Figure 6.5e) [92, 225, 226]. LLI has been found to be the most prominent degradation mechanism at the anode [227]. The main cause of LLI has been found to be SEI formation and growth on the anode [228].

6.3.3 Ultrasonic response changes during degradation

The relationship between the SOH and the ultrasonic response was investigated, using the methods described in Section 6.2.4. In this case, the Spearman correlation coefficient was employed to determine the correlation of SOH estimation with the ultrasonic signal parameter throughout the test. The Spearman correlation coefficient rs can be computed using:

$$rs = \frac{cov(x_i, y_i)}{\sigma x_i \sigma y_i} \tag{6.9}$$

where $cov(x_i y_i)$ is the covariance of the rank variables x_i and y_i for the original data and σx_i, σy_i are the standard variations of the rank variables. The rs ranges from -1 to +1, where -1 is a perfect monotonous decreasing correlation and +1 is a perfectly monotonously increasing correlation. This was determined to best evaluate the relationship between the SOH and TOF as the change in TOF was observed to not be consistently linear. Similar statistical models, such as the Pearson correlation, would therefore not be best suited, as this will prioritise the linearity of the relationship.

The Spearman correlation coefficient was calculated for the TOF of all peaks in the A-Scan – for example, all peaks seen in Figure 6.1a against the change in SOH. Cell A saw 41 peaks were compared and cell B saw 40 peaks compared. From that, using the definition of Short and Long reflections in Section 6.2.4, four peaks were found, with two peaks for cell A and two for cell B. For Short A and Long A, the coefficient was -0.831 and 0.821, respectively. For Short and Long B, the coefficient was 0.906 and 0.810, respectively. All absolute values were above 0.8, which indicates a strong correlation between the permanent TOF shift and capacity fade. Notably, the short TOF for both cells had greater absolute values than the long TOF, which suggests that shorter TOF - signals that are reflected back earlier through the cell - are more reliable at detecting capacity fade. This could be related to the reduced number of superimposed interfaces on the signal, as the signal will have travelled through half of the cell rather than through the whole cell. This will require the assumption that the ratio of lithium-ions between the electrodes is consistent throughout the whole cell. It should be stated that not all peaks are equal; there were some peaks that had Spearman correlation coefficients nearing 0, suggesting a lack of correlation between the TOF and capacity fade. This highlights the importance of ensuring that the correct peak is used, not just the largest peak, when estimating the SOH of a cell. Correct meaning the peak with the strongest correlation between TOF and SOH.

The changes in acoustic signal against the change in SOH are shown in Figure 6.6 (where Figure 6.6a and 6.6c are Short A and Short B, and 6.6b and 6.6d are Long A and Long B, respectively). The colour gradient is employed to signify the cycle

number, wherein the gradient transitions from a lighter hue (earlier cycles) to a darker one (later cycles). The ultrasonic response for all cells showed deviation from cycle 1, which is considered the baseline signal. The average capacity fade for cell A was approximately 0.03% per cycle, and cell B had an average capacity fade of 0.02% per cycle. After 100 cycles, cell A had a remaining capacity of 96.42% and cell B had 97.6%.

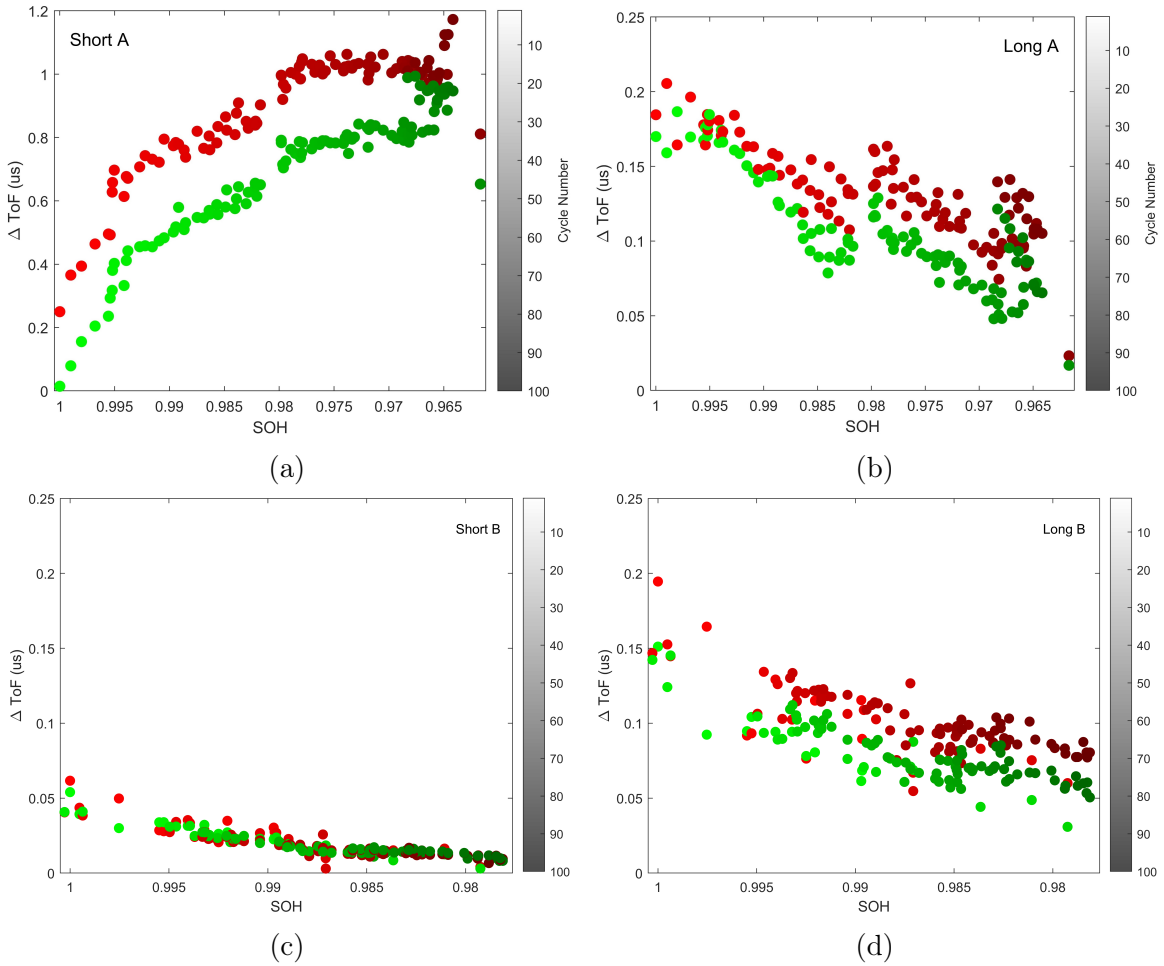

Figure 6.6: Comparison of (a) Short A, (b) Long A, (c) Short B and (d) Long B over 100 cycles. The green dots represent a SOC of 100% and the red dots represent a SOC of 0%. The hue of the dots represents the cycle number: the hue darkens as the cycle number increases. It should be noted the y-axis for a) is much larger than for the other figures to allow for readability.

Short A saw an increasing TOF change of 0.876 µs alongside a capacity fade of 3.58%. Conversely, Short B saw a decreasing TOF of 0.0393 µs over a 2.15% capacity drop. Long A saw a decrease in TOF by 0.101 µs over a drop in capacity of 3.58%. And Long B saw a permanent negative change in TOF for the long TOF of 0.109 µs over a drop in capacity of 2.15%. This is summarised in Table 6.2.

All peaks except Short A saw a linear decrease in TOF, which saw a significant

increase. There are several potential reasons that can result in unpredictable and unstable acoustic results [229]. One of these reasons is cell-to-cell manufacturing variation. There is limited coordinated effort to quantify such variations in product specification. This can result in variations not being identified until after experimental studies on the complete cell [230]. Another possible source of the difference observed between nominally identical cells is the transducer and associated bonding method. As the transducer is extremely sensitive, any difference in the surface it is bonded to, the pressure applied to the transducer, the frequency, the type of couplant, and the quality of the probe can have significant effects on the signal [231]. In this case, the transducers were from the same manufacturing batch, used the same couplant and were bonded using the same method, reducing the signal variation due to the transducer and bonding.

As the maximum capacity is decreasing with each cycle, the TOF difference between fully charged and fully discharged should see some slight changes as a result of the decreased Li-ion movement. Both cells produced results that differed from one another. Short A started with a difference of $\sim 0.24\ \mu s$, which decreased linearly to $\sim 0.17\ \mu s$. For the later peak, Long A started at 0.02 µs, ended at 0.04 µs. Both the selected peaks in cell B did not exhibit changes in the TOF difference as the cell degraded. Short B had a consistent average of $\sim 0.0052\ \mu s$, and Long B was constant at $\sim 0.024\ \mu s$. Both peaks saw very similar differences for each cycle, only differing in magnitude. The drop in SOH seen in Figure 6.4b and the difference in TOF seen in Figures 6.6b and 6.6c align well, suggesting accurate acoustic measurements of the maximum cyclical capacity of the cell.

As can be observed, there is an apparent consistent change in the TOF implying that the internal changes within the cell were being detected. Given the rate of degradation is seen to be relatively linear in Figure 6.4, linear regression was utilised to determine the TOF shift matched the capacity fade, shown in Figure 6.7. This provided an R-squared (R^2) that ranges between 0 and 1, where 0 means no correlation between the SOH and TOF and 1 is a perfect correlation between the two variables.

Figure 6.7 shows the R^2 values for the selected peaks of both cells and is summarised in Table 6.2. The short TOF had a greater R^2 for both cells, further suggesting that shorter TOF measurements have a stronger relationship with SOH regardless of the shift the signal undergoes. The degradation rate has been found to depend on the cathode chemistries and operating conditions [232]. For NMC cells, the cell degradation rate decreases as the cell is cycled long term [233]. As seen in Figures 6.6a and 6.6c, there is a slight gradient change as the SOH drops, which is not as visible in the Long reflections. Longer term testing will be needed to confirm this SOH bias to the Short reflections.

A shift to a shorter permanent TOF means a faster speed of sound through a cell. Using Equation 6.2, it can be assumed that this is in part caused by an increase in E (MPa), a decrease in ρ or a combination of the two. Conversely, a permanent shift to a larger nominal value will suggest the difference is decreasing. This is demonstrated within a single cycle, where the lithium-ions intercalate and de-intercalate with the anode and cathode. During charge, the lithium-ions de-intercalates from the cathode and intercalates into the anode, and the reverse is true when discharging. It has been

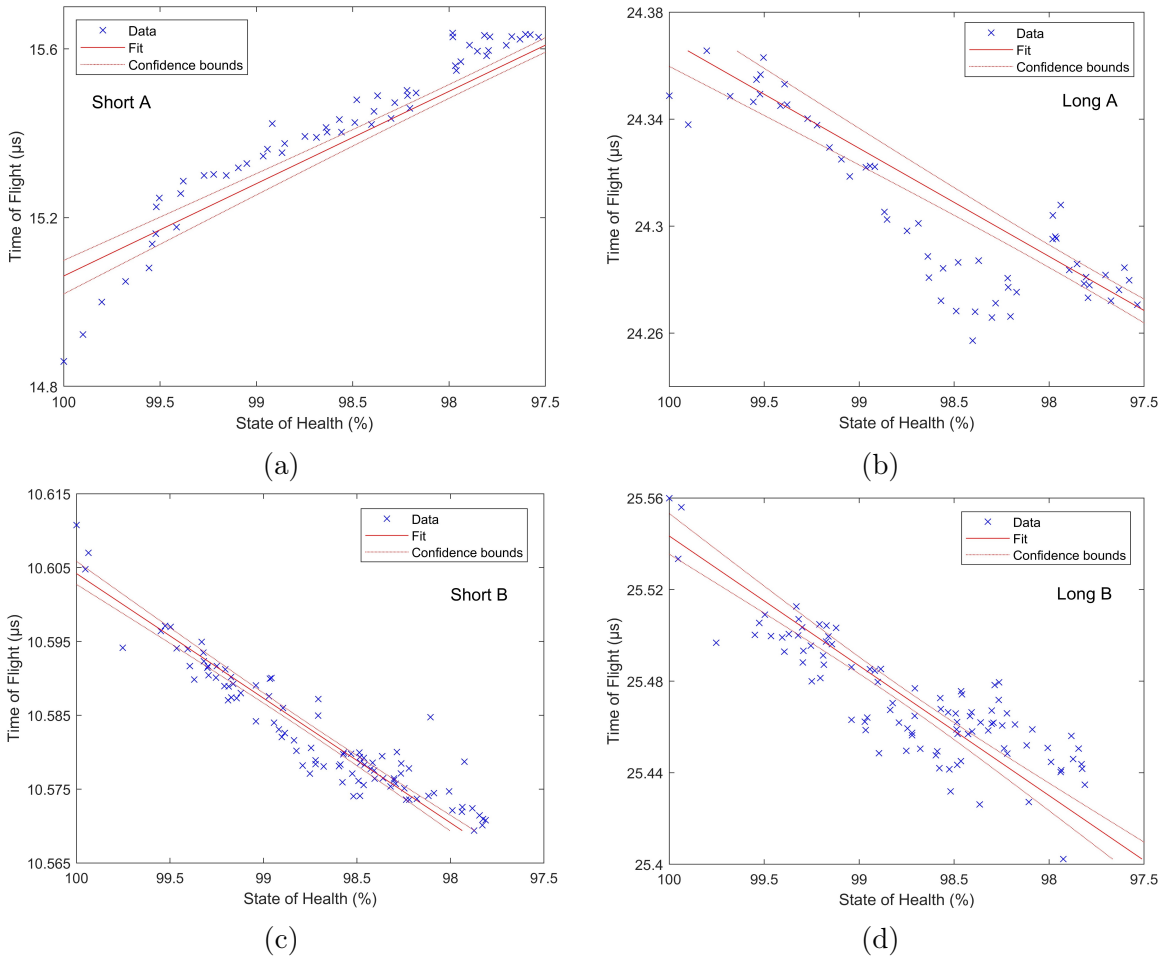

Figure 6.7: R^2 plots for a) Short A, b) Long A, c) Short B and d) Long B. The shorter peaks showed a stronger correlation with SOH compared to their longer counterparts.

Cell	Capacity Drop (%)	Capacity Drop per Cycle (%)	Peak	Spearman Correlation Coefficient	TOF Change (µs)	TOF Shift / Capacity Drop (µs / %)	Linear Regression
A	3.58	0.03	Short A	-0.831	0.876	0.245	0.874
			Long A	0.821	-0.101	-0.028	0.756
B	2.4	0.02	Short B	0.906	-0.0393	-0.018	0.898
			Long B	0.81	-0.109	-0.051	0.753

Table 6.2: Summary of capacity and TOF changes, along with correlations, for both cells and selected peaks.

shown that the anode has a much greater sensitivity to changes in the SOC than the

cathode, as between an SOC of 0 and 30% the anode layer can expand almost 10% and the Young's modulus can increase by 20% [234]. The Young's modulus of the anode triples as it becomes fully lithiated to LiC_6 [235]. The anode undergoes greater expansion during lithiation, seeing a volumetric expansion of 9.8% when charged from 0% to 30% SOC [234]. This is demonstrated across all peaks in Figure 6.6, where the TOF when fully charged (lithiated anode) is always less than when fully discharged (de-lithiated anode), i.e. the red dots are higher than the green dots in Figure 6.6. The volumetric expansion affects the TOF by affecting the propagation path of the acoustic signal; an increase in volume results in a longer path, and therefore the signal requires more time to cover the distance. This amplifies the change in TOF when combined with the change in the speed of sound, due to material properties. In the case of the permanent TOF shift, the continued growth in the SEI layer driving the LLI will gradually affect the TOF. A shift to a shorter permanent TOF means the speed of sound has increased through the cell, whilst a shift to a longer TOF represents a decrease in the cell's speed of sound.

Given the change seen in Figure 6.5 and general trend for Figure 6.6 of a decrease in permanent TOF, a relation of LLI to a negative shift in permanent TOF is not unreasonable. The inconsistency between the polarity of the correlations is likely to be caused by complex behaviours of multiple layers during cycling, as at each interface the ultrasonic signal will split as defined in Equation 6.5. It is worthy of note that the polarity can vary within the same signal, as Short A and Long A were from the same sensor monitoring the same cell. Similar results have been found in the literature. Reference [95] found that the selected peak saw a permanent shift to a shorter TOF as the NMC cell aged, while reference [96] saw a permanent shift to a longer TOF in the selected peak as the LCO cell aged. [94] also saw a permanent shift to a longer TOF in an LCO cell, but within 60 cycles the permanent shift gradually decelerated until there was no noticeable change in the TOF between cycles. It should be noted that the frequencies and the TOF of the selected peaks differed between these articles. However, all tracked peaks were from the first reflection. [96] noted that the TOF shift was likely due to swelling, while [95] and [94] did not discuss the degradation method.

Swelling was not detected within Cell A or Cell B. For Cell A, all short peaks (peaks within the first and second reflection) saw a permanent shift to a longer TOF, whilst all long peaks saw a permanent shift to a shorter TOF. This was not present in cell B, as the polarity matched between the two peaks. The direction of the permanent shifts seen in the cells matches that of that seen in [95], which had the same cell chemistry of NMC, whilst the others used a different cell chemistry. This suggests that the cell chemistry affects the direction of the permanent shift, though this will require further investigation.

6.3.4 State-of-health and ultrasonic fluctuations

As shown in Figure 6.4, the SOH measured in both cells underwent fluctuations as they degraded, particularly with cell B. Figures 6.8a and 6.8b show the SOH drop of cell A, with the Short A and Long A plotted alongside. The same for cell B can be seen in Figures 6.8b and 6.8d. There is a visible relationship between the SOH and

TOF fluctuations.

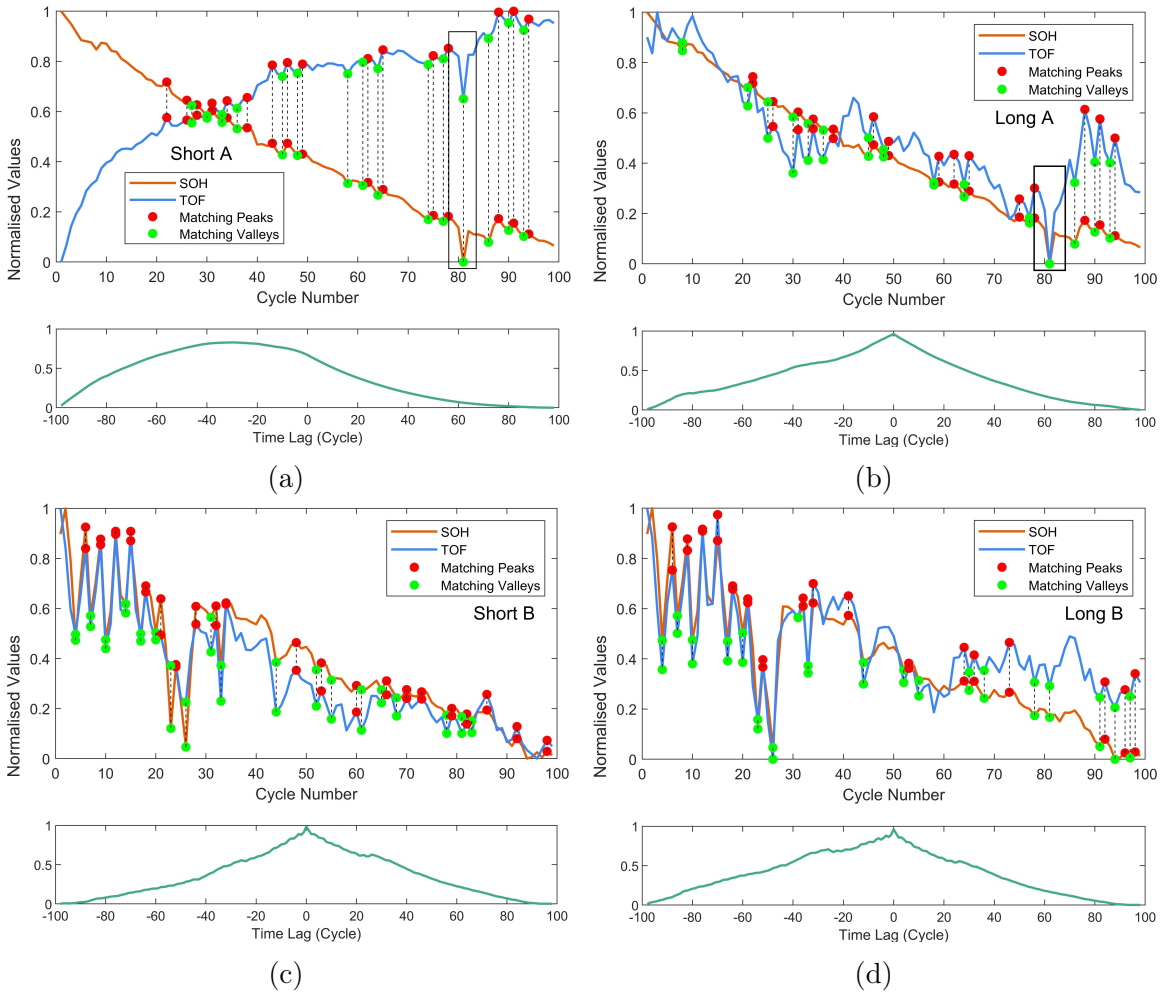

Figure 6.8: Matching peaks and valleys between the SOH estimation and TOF of Short A (a), Long A (b), Short B (c) and Long B (d). The time lag for the four peaks are also presented to highlight the sensitivity of the TOF to SOH changes.

Cell A experienced lower magnitude fluctuations than cell B; however, there was a significant drop around cycle 80, which is indicated by the black box. This perturbation is also observed in the ToF signal, despite the permanent shift leading to a longer TOF. The change in TOF was 0.167 µs, which is $\sim$ 19% of the total TOF shift. In comparison, the capacity fade of this perturbation was $\sim$ 15% of the total capacity drop. There are also SOH peaks and valleys that are reflected in the TOF, namely around cycles 40 and 90. The fluctuations show a clear correlation with the TOF response, show in Figure 6.8a. The fluctuations in Long A were greater in magnitude compared to the overall shift, along with a less linear shift as the cell was cycled. At cycle 80, the same significant valley is observed; however, the amplitude of the TOF shift is more significant than in Short A. The change in TOF was 0.036µs, which is $\sim$ 36% of the total permanent shift. Both the short and long signals observed this shift. Cell B showed unstable SOH readings for the first 30 cycles, as shown by

the significant fluctuations. Both the long and short TOF readings reflected these fluctuations as the signals oscillated in a similar manner.

Temporal dependencies between the TOF and SOH were explored using the cross-correlation technique, implemented through MATLAB's 'xcorr' function. The introduced time lag (τ_{lag}) quantifies the temporal relationship, indicating the extent to which the TOF lags behind or leads the SOH. A positive τ_{lag} indicates that the TOF precedes the SOH, while a negative τ_{lag} suggests the reverse, with a τ_{lag} of 0 denoting a simultaneous change in the TOF and SOH. It can be seen in Figures 6.8b, 6.8c and 6.8d that τ_{lag} is 0 when the correlation coefficient is highest. This alignment at $\tau_{\text{lag}} = 0$ indicates that the TOF dynamically shifts simultaneously with the SOH. In particular, the correlation strength is consistently observed to have its maximum value – all above 0.95 – at $\tau_{\text{lag}} = 0$ in the three subfigures. This is summarised in Table 6.3.

Peak	τ_{lag} (Cycle)	τ_{lag} Strength
Short A	-30	0.829
Long A	0	0.962
Short B	0	0.984
Long B	0	0.961

Table 6.3: Time lag location and strength for each peak.

For Figure 6.8a, the correlation for Short A is greatest at τ_{lag} = -30 cycles with a range of lags at which the two signals have similarities. This suggests the SOH precedes the TOF by a range of possible cycles, where the strongest correlation occurring with a difference of 30 cycles. This is unlikely given the results from the other peak, notably the valley at cycle 81 matching with no delay. This behaviour is not seen in the other peaks, suggesting that the signal is exhibiting anomalous behaviour. This could be based on the direction of the TOF shift, as Short A is the only peak that underwent an increase in TOF as the cell capacity dropped.

6.4 Conclusion

Accurate estimation of cell state-of-health can contribute to the increase in the safety and longevity of lithium-ion cells. In this work, two cells with a cycle life of 301 cycles were cycled at a C-rate of 0.3C for 100 cycles within manufacturer capacity limits to induce non-abusive degradation. The results displayed a strong correlation between the change in the ultrasonic time-of-flight response and cell degradation when analysing longer reflections. The direction of the shift matches work using the same cell chemistry, while cells with different chemistries tested within literature were found to have a different direction in the permanent TOF shift.

For shorter reflections, they were observed to behave differently, with one cell showing a decreased permanent shift and the other an increased permanent shift.

There are several reasons this may have occurred: one of them is manufacturing differences between the cells; another could be due to the transducer, as the Long TOF and Short TOF differed within the same signal. All reflections after Short A saw a decreased permanent shift, the same as seen in cell B. Systematic testing showcased the feasibility of ultrasound in monitoring the state-of-health of lithium ion cells. Through the use of IC analysis, the primary degradation method for the cells was observed to be the loss of lithium-ion inventory.

The investigations also found that although the rate of degradation was linear, there were fluctuations observed, resulting in inconsistent loss in state-of-health estimates. Ultrasonic time-of-flight responses were identified to react to these fluctuations, resulting in the detection of state-of-health variations that provide immediate responses. This was true regardless of the permanent shift direction. This offers the potential to observe regeneration phenomena and irregularities in the available capacity during operation. SOH anomalies can therefore be detected using ultrasound. However, a large dataset will be necessary for acoustic anomaly detection to be used on a larger scale.

In order to develop this dataset, standard and anomalous cause battery degradation will need to be accounted for. Controlling the variables that cause battery degradation will be necessary to ensure the accuracy of the estimations. One such set of variables would be the various degradation methods. Inducing different degradation methods as the primary mechanism in similar cycling conditions could provide insight into the relation between capacity drop and the resultant ultrasonic response. This could be performed by repeating the tests at various C-rates and varying temperatures, or under- and over-charging the cells. Long cycling will allow for observations of degradation and ultrasonic behaviour as the cell reaches the end of life. Including post-mortem analysis could determine the sources of degradation and allow validation of the ultrasonic response. Investigating the effect of the cathode chemistry on the direction of the permanent shift could improve the viability of this method for SOH estimation, as this is in contention in literature. This can be done using simultaneous testing of multiple cells of differing cathode chemistries.

Chapter 7

Acoustic Assessment of Lithium-Ion Batteries: Unravelling Temperature and Charge Contributions

Abstract

Lithium-ion batteries (LIBs) are critical for renewable energy storage, and accurate charge and health estimation remains a significant challenge. Acoustic sensing offers a unique method to observe lithium-ion movement between electrodes during battery operation. However, both the charge state and the internal temperature of the battery affect the acoustic response.

This study systematically investigates the interactions between temperature and charge state on acoustic signals through a novel thermal cycle methodology. Using a global sensitivity analysis, we demonstrate that temperature has a non-negligible and dominant effect on the acoustic signal, with a largely insignificant cooperative interaction with charge state. The results reveal temperature-induced variations in the acoustic signal that increase with charge level, though not uniformly.

These findings underscore the critical importance of temperature compensation in acoustic-based LIB estimation techniques. By quantifying the independent and cooperative effects of temperature and charge, this research provides the possibility of independently measuring thermal and SOC effects on the acoustic signal without the need for additional thermal sensing equipment.

Keywords: Lithium-ion battery; Ultrasonic acoustics; Global sensitivity analysis; Gaussian processing

7.1 Introduction

Lithium-ion batteries (LIBs) have emerged as a transformative energy storage technology since their commercial introduction by Sony in 1991. Characterized by high energy and power densities, extended cycle life, and minimal self-discharge [236–238], LIBs have become the dominant battery chemistry across portable electronics and the rapidly expanding electric vehicle (EV) market [3, 4]. This technological advancement presents a critical pathway to decarbonizing transportation, which currently accounts for 12% of global greenhouse gas emissions [239].

Despite widespread adoption, LIBs face significant challenges in real-time monitoring and safety. This is despite a low failure margin of 1 in 10-40 million batteries [240, 241]. Battery Management Systems (BMSs) have been developed to address these concerns, employing various sophisticated techniques such as neural networks and support vector machines working from a large real dataset [242], models such as the Thevenin model using open-circuit voltage measurements [149], and Coulomb counting [243].

These methods have been successfully implemented in real-world situations, but all of them are monitoring variables, such as cell voltage, current, and surface temperature [48], that are externally monitored from the cell; they are unable to monitor the movement of Li^+ which is the driving mechanism for LIB operation. The movement of Li^+ between the electrodes is assumed from electrical and electrochemical models [53]. These electrochemical systems use physics-based methods to provide information on the internal electrochemical dynamics of a LIB [244]. These models have been used to monitor changes in the electrochemical parameters such as terminal voltage [245, 246], detecting abusive operating conditions [247] and cell ageing [248]. However, these methods model the internal changes, albeit with high accuracy. Direct monitoring of the internal changes are not implemented with these models, as the external electrochemical variables such as the cell voltage or current and estimate them through the use of physics [244].

To address this gap, acoustic monitoring has emerged as a promising answer to direct monitoring of the internal dynamics. First introduced by Sood in 2014 [249], ultrasonic monitoring offers a unique approach to battery estimation by monitoring Li^+ movement between the electrodes causing material property changes during battery operation. These changes, primarily in bulk and shear moduli and density, directly influence acoustic wave propagation speed through a medium, allowing for indirect yet precise observation of electrochemical processes. The sound propagation speed is defined as:

$$c = \sqrt{\frac{K + \frac{4}{3}G}{\rho}} \tag{7.1}$$

Where: c = Speed of sound (m s^{-1}) - K = Bulk modulus (GPa) - G = Shear modulus (GPa) - ρ = Density of the material (kg m^{-3})

At each interface between two media, part of the acoustic wave will transmit into the new medium and part will be reflected. The ratio of the transmitted signal to

reflected signal is dependant on the difference in acoustic impedances (Z) of the two media. This is called the reflection coefficient (R), and is defined as:

$$R = \frac{Z_2 - Z_1}{Z_2 + Z_1} \tag{7.2}$$

where Z is defined as:

$$Z = \rho \times c \tag{7.3}$$

As the signal splits when interacting with an interface, the signal amplitude decreases with respect to the ratio of transmission to reflection. The signal also sees attenuation as it travels through a medium [250], and this can be defined as:

$$A = A_0 e^{-\alpha d} \tag{7.4}$$

Where: A = Final acoustic amplitude - A_0 = Initial acoustic amplitude - α= Attenuation coefficient - d = Distance travelled by the wave (m)

This can be observed as absorption, which is the conversion of acoustic energy into heat in the host medium.

As the speed of sound is affected by the changes in material properties, the time-of-flight (TOF) of the battery is also affected. This makes it a useful ultrasonic property for monitoring SOC, and will be explored within this work.

The relationship between TOF and SOC is known in the literature to be linear [80,251], as a result of the linear changes to the elastic moduli [252,253] and volumetric expansion [254–256] of the electrodes with respect to Li concentration. Equation 1 illustrates that the elastic moduli and density that are proportional to the speed of sound, and therefore the TOF. There are other variables that can affect the TOF in LIBs. The state-of-health (SOH) can permanently shift the base TOF as the cell degrades [179], which can differ between cathode chemistries [95, 96]; defects within the cell can notably alter the response [100]; and the internal structures of the cells can affect the signal, such as the number of layers [257].

Temperature, in comparison, has received less interest with regard to acoustic LIB monitoring, except for a few articles [174, 175, 258] developing methods to decouple and monitor temperature and charge during operation for thermal runaway detection. These have been summarised in Table 7.1. Temperature is known to cause thermal expansion and affect the way acoustic waves travel through different media, with an increase in temperature decreasing the speed of sound through a metals [259]. This is of note, as most LIBs have lithium-metal-oxide cathodes..

$$dL = L_0 \alpha (T_1 - T_0) \tag{7.5}$$

Where: dL = Change in Length (m) - L_0 = Initial Length (m) - α = Thermal expansion coefficient (K^{-1}) - T_1 = Final temperature (K) - T_0 = Initial temperature (K)

The electrodes have been found to expand mostly linearly with temperature [260, 261], which increases the travel path for the ultrasonic waves resulting in a longer

TOF if all other variables are constant. However, research is not in total agreement over the effects of temperature on TOF measurements. Some reports state temperature is not a significant variable to consider [6] whilst others state ultrasonic waves can be more sensitive to temperature than charge [262, 263].

In this study, we investigated the effects of temperature and charge on the acoustic signal when monitoring LIBs, both independently and combined. This was to determine the dependence or independence of the two variables upon the acoustic signal. In order to carry this out, a method of thermally cycling cells at different states-of-charge (SOCs) while recording the acoustic signal was used to create a matrix of data points of temperature, battery charge, and acoustics. Multiple cells were used in this study. We found that temperature and the TOF have a linear correlation - as temperature increases, the TOF increases. Charge has an inverse relationship with the TOF, as an increase in SOC results in a decrease in TOF. The two variables are mostly independent from one another when looking at the change in TOF, meaning that a change in temperature would cause a similar change in the TOF when performed at different SOCs. Our research not only addresses the current knowledge gap regarding temperature effects but also provides a foundational framework for improving the accuracy and reliability of acoustic monitoring techniques across different lithium-ion battery chemistries.

Table 7.1: Papers Addressing Temperature and TOF in LIBs.

Findings	Reference
Ultrasonic TOF was corrected for temperature effects using -10, 25 and 60 °C	[174]
Ultrasonic TOF can be used to detect temperature fluctuations	[258]
Corrected temperature effects on TOF for the use of detecting thermal runaway based on overcharging cells	[175]

7.2 Methodology

7.2.1 Materials and equipment

All pouch cells (NMC811/graphite) were purchased from RS Pro with stock number 125-1266, and were tested without further modifications. The cells were commercial lithium-ion pouch batteries with a capacity of 2000 mA h and a voltage range of 3.0 - 4.2 V. The cells had an NMC cathode and a graphite anode. The cells had dimensions of 63 x 43.5 x 7 mm and a weight of 40 g. The cells were from the same manufacturing batch and nominally are identical. The piezoelectric transducers were purchased from Del Piezo Specialties, and had a central frequency of 2 MHz. This frequency was determined based on previous work, outlined in [178], where 2 - 2.5 MHz was found to provide an acceptable balance between the sensitivity of the signal to internal changes, and the resistance of the signal to attenuation. These values, along with

the experimental parameters are shown in Table 7.2. The M-Bond 200 adhesive was purchased from Micro Measurements. The K-type thermocouples were purchased from RS Pro with stock number 621-2170. The Picoscope 5444D oscilloscope was purchased from Pico Technology.

7.2.2 Instrumentation

Piezoelectric transducers were bonded to the centre of a cell's surface using the M-Bond 200 adhesive at room temperature. The transducers were wrap-around as the cells were housed in plastic cases. The positive and negative electrode were both accessible from the top of the transducer, making the soldering of co-axial wires possible. The co-axial wires were stripped and the positive and negative cables were separated to be soldered onto the transducer electrodes. The thermocouples were attached to the surface of the cells using electrical tape. The transducer acted as a transmitter and receiver of the acoustic signal and was controlled by the Picoscope. The acquisition time was once a minute for all data types. The acoustic data was recorded for one second every minute and each capture recorded 50 pulses.

7.2.3 Thermal and charge cycling

The cells were thermally cycled in a MACCOR MTC-020 temperature chamber. The temperature was cycled in 5 °C steps, starting at 20 °C. The temperature was dropped to 10 °C, increased to 50 °C and returned to 20 °C, see Figure 7.1. The target temperatures were held for one hour. This provided a rest time for the cells to reach the target temperature and data collection. In order to negate the resting period for data analysis, a range of ±0.3 °C for the cell surface temperature was used to discriminate between resting data and thermally stable. The target temperature range was selected to test the effects of temperature on the acoustic signal within the normal battery operating temperatures. Temperature based degradation, such as SEI decomposition at ~80 °C and lithium plating at ~−20 °C were avoided to reduce additional influences on the acoustic signal. This thermal cycle was performed at various cell SOCs, increasing from 0% to 100% in 20% steps. The cells were charged in this manner using a MACCOR Model 3650 battery cycler. The cells were charged with a current of 0.3 C between 3 and 4.2 V.

7.2.4 Data analysis

Acoustic and temperature data were recorded using a bespoke LabVIEW VI, and the battery data was recorded using the MACCOR software. The acoustic data was averaged across the 50 pulses and filtered using MATLAB's *wdenoise* denoising function, applying a high-pass filter. A peak tracking method was used to identify each peak in the acoustic response and track their movement, both the amplitude and TOF, throughout the experiment [7]. Tracking the individual peaks provides the ability to determine if and how the amount of cell exposure affects the signal.

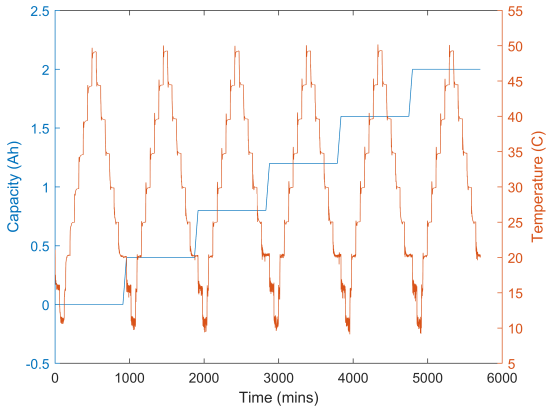

Figure 7.1: Visualisation of the charge and thermal cycling scheme.

Sensitivity analysis was performed in Python using the *romcomma* package. This package utilises global sensitivity analysis and Gaussian process regression to create a reduced order model [264]. Here, we employed the Sobol' index, a variance-based method that quantifies the individual and codependent contributions of the charge and temperature on the TOF. The Sobol' indices are computed by partitioning the total variance of the model output into components corresponding to each input parameter, as well as their interactions. For an input variable, the first-order Sobol' index represents the fraction of the output variance attributable solely to the variation in while higher-order, in this case total-order indices, capture the influence of interactions between multiple input factors. These indices are calculated through Monte Carlo sampling, where a large number of input-output pairs are generated to estimate the contribution of each input factor. The datasets underwent k-fold cross-validation. Each dataset was split into k=27 folds, where k-1 inputs were used for training the model, and the k-fold was used for testing. The testing fold was rotated through all data points. This method allowed for the confirmation that the model exhibited no bias toward any specific data points, but was trained on the larger trends of the dataset.

In this work, the GSA was used to detect the influence of the temperature and the SOC - based on the spread of the Li-ions between electrodes - on the acoustic signal. The input variables were the SOC and the surface temperature of the cells, and the output variable was the TOF measurements. The first order Sobol' indices contained the effect that the SOC and temperature had independently on the TOF. The second order Sobol' indices contained the co-dependent effects of both SOC and temperature on the TOF.

Table 7.2: Cell and Test Design Parameters.

Parameter	Value
Cell Capacity	2000 mAh
Cell Chemistry	NMC
SOC Step Increment	Increase of 20%
Charge Rate	0.3C
Voltage Range	3.0-4.2 V
Temperature Range	10 - 50 ℃
Temperature Step Increments	Change of ±5 ℃
Number of Discrete Points	54 - Nine Temperature at Six SOC
Time Held at Each Discrete Point	One Hour
Age of Cells	Fresh
Number of Full Charge Cycles	Zero - cells were only charged
Form Factor	Jelly Roll
Sensor Central Frequency	2 MHz

7.3 Results

7.3.1 Finding the acoustic influences

By thermally and electrochemically cycling the cells, the influence of each on the acoustic response could be determined. It is proposed propose that controlling these two parameters (temperature and charge) at stable points creates a discrete matrix to isolate their influences, with the acoustic signal captured via piezoelectric crystal in pulse-echo mode to characterise the internal active layers (Figure 7.2a). The temperature and charge of the cells were adjusted over a long time-frame to ensure uniformity of internal temperature and lithium-ion movement, respectively.

The resultant acoustic signal (A-Scan) from one of the cells (Figure 7.2b) shows multiple clear echoes where the initial pulse has travelled through the cell and reflected from individual active layers, such the separators and electrodes, and the back wall. The increase in amplitude at ca. 13 µs signifies the first full reflection (with preceding peaks resulting from a combination of transducer ringing, signal superposition and the first half reflection), whilst the amplitudes and TOFs of the second and third identified reflection groups suggest an acoustic barrier within the cell. This is to be expected, as the cells were prismatically wound, creating a pool of electrolyte in the centre of the cell. Given the prismatic winding design of the cells, it can be assumed that every 2 n - 1 echoes are half echoes, as the signal would split at the pool due to greater differences in acoustic impedances between the electrolyte and the active materials. As these echoes contain information for at least half of the cell, they can still be used for analysis. This also implies that the resultant acoustic echoes are a superposition of multiple reflections from individual layers within the cell, rather than each echo correlating to a specific layer or active component [7].

The surface plot of the signal for one thermal cycle demonstrates the significant

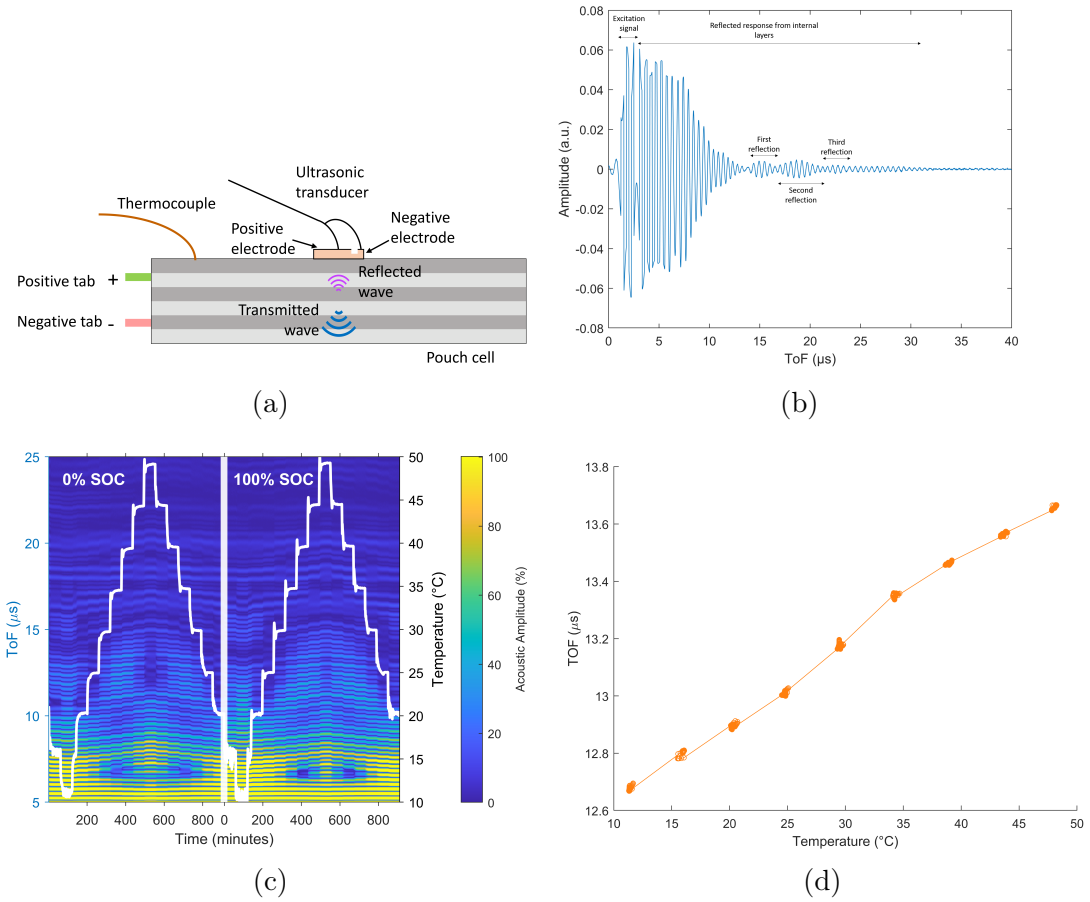

Figure 7.2: a) Schematic of ultrasonic monitoring setup for a LIB. b) The first three identifiable groups of acoustic reflections are highlighted. c) 3D plot comparison of a thermally cycled cell when fully discharged and fully charged, with temperature overlaid in black. d) a plot of the change in TOF of a single peak compared to the change in temperature.

effect temperature has on the acoustic signal (Figure 7.2c). The transitions between the temperature steps are clearly visible within the plot, with TOF increasing and decreasing in distinct increments alongside temperature changes; each step was maintained for one hour to ensure signal stability. With respect to temperature, the change in the TOF can be attributed to thermal expansion, which influences the TOF through two primary mechanisms: altering both the layer thickness (affecting acoustic travel path) and density.

The thickness of a material is inversely proportional to the density; as the thickness increases, the density decreases. The change in density affects the speed of sound through a material as defined in Equation 7.1, though our analysis suggests that the effect of the increased travel path outweighs the impact of the increased speed of sound when comparing the two SOCs presented in Figure 7.2c.

Figure 7.2c shows a comparison between the signals of a cell when fully discharged (left) and fully charged (right) during a thermal cycle. The comparison shows there

are some notable changes, mainly in the amplitude of the peaks. Observing the TOF of the two signals, the peaks from the transducer runoff line up as expected, as they are mostly unaffected by changes to the cell. From ca. 12 µs, slight offsets can be seen, which increase as the initial TOF increases. The changes observed are limited when compared to the influence of temperature.

In pursuit of a deeper understanding of the relationship between temperature and charge, we isolated selected peaks to plot the change in TOF through the cycles. First, the effect of temperature on a single acoustic peak at a constant SOC was plotted (Figure 7.2d). To ensure that temperature data from at least half of the cell was represented, under the assumption that the cell is mirrored across the acoustic barrier, the selected peak was taken from the first echo. A key observation is the linearity and reversibility of the plot; a positive correlation is seen between TOF and temperature. This is to be expected, given the volumetric thermal expansion α_v of solids, such as graphite or metals, is defined as:

$$\alpha_v = \frac{1}{V}\frac{dV}{dT} \tag{7.6}$$

where V = volume (m^{-3}) - T = temperature (°C) and $\frac{dV}{dT}$ = rate at which the volume changes with respect to changes in temperature. The changes in volume, be it expansion when heating or contraction when cooled, changes the path length the ultrasonic signal must travel. If the cell heats up, the travel path increases, so the signal has to travel further to pass through the cell. The speed of sound through the material would also change, as the internal layers decrease in density. If during operation, the Young's modulus would also change with the movement of the ions between the electrodes. All these have an effect on the TOF.

Similar findings have been observed in other works [265, 266]. Following from this, the same peak was tracked across all tested SOC (Figure 7.3a). The results suggest the SOC has a negative correlation with the TOF, reducing the initial time as the cell is charged. This confirms the transducers were working as intended, as the negative correlation has been recorded multiple times within literature and has become the basis of this estimation technique [80, 82, 83].

We observe distinct patterns in the TOF measurements across the different SOC and temperatures states, with the most significant TOF change occurs between 0% and 20% SOC, with characteristic overlapping near 50% SOC that persists across all examined temperatures. These observations largely align with the known behaviour of thermal expansion in LIBs, which varies as a function of both temperature and SOC [267]. Although electrodes undergo phase changes during charge-discharge cycles that affect thermal expansion [268], these effects are minimal compared to ionic movement during operation [267].

Our observations indicate that thermal expansion exhibits quadratic behaviour at lower temperatures, transitioning to a more linear pattern at higher temperatures. Above 25 °C, the TOF shift with temperature displays more linear characteristics across most SOCs. This agrees with results found by [267], where cells with a similar jelly roll design saw non-linear thermal expansion below 25 °C, and linear expansion above 25 °C. The reasoning provided was that thermal expansion was linear, but

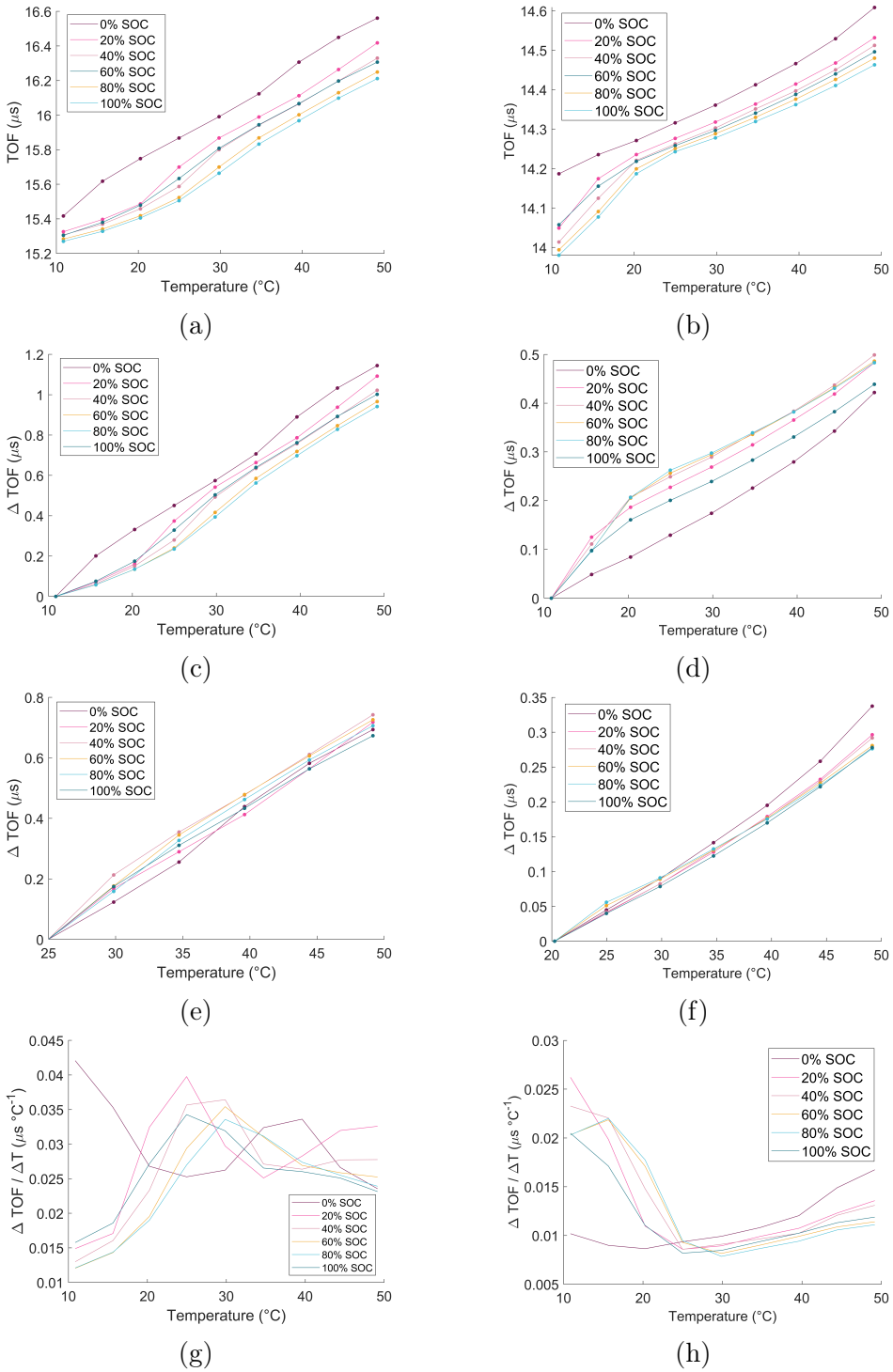

Figure 7.3: a) and c) TOF profile and subsequent change in TOF of selected peak the from the first reflection of Cell 1. e) presents the change in TOF of the peak from 25 °C as this is the temperature all SOC follow a similar trend. g) shows the gradient of the TOF changes across the SOC. b), d), f), and h) show the same for a random peak in Cell 2. f) shows from 20 °C for the same reasons as given for e).

at lower temperatures there is 'empty space' that the internal layers expand into, providing the difference in observed expansion behaviours. As the relationship between the TOF and temperature appear to be proportional, an increase in thermal expansion would result in a proportional increase in TOF. The increase in the TOF is a direct result of the thermal expansion, as the travel path of the acoustic signal has increased with the increase in temperature.

Although Cell 1 exhibits an increasing slope as the temperature increases to 25 °C, Cell 2 demonstrates a flattening trend under similar conditions. Both cells show behaviour at 0% SOC in lower temperatures that deviate from the other SOC, with these patterns persisting until specific temperature thresholds - 20 °C for Cell 1 and 25 °C for Cell 2. Beyond these thresholds (Figures 7.3g and 7.3c), the SOCs show stronger alignment, with a greater response at the lower SOC attributed to increased thermal expansion [267]. Looking at the first-order differential of the TOF (Figures 7.3d and 7.3h) reveals that between 20% and 100% SOC, the gradients follow similar trends without discernible correlation with magnitude. The gradient patterns between cells mirror each other, though Cell 1's gradient (7.3d) is approximately double in magnitude compared to Cell 2's. These characteristic patterns, including the distinctive behaviour at 0% SOC and the temperature threshold transitions, are consistently observed in the gradient analysis.

The characteristics of thermal sensitivity differ significantly between cells, with Cell 2 (Figure 7.3e) showing a sharper increase in TOF between lower temperatures, except for 0% SOC as discussed earlier, before transitioning to a shallower increase at higher temperatures, contrasting with the behaviour of Cell 1. Despite these differences, both cells exhibit monotonic non-decreasing behaviour in temperature-TOF relationships. Examining the differential responses of the TOF (Figures 7.3b and 7.3f) highlights a distinct difference in behaviour between 0% SOC and all other charge states, especially at lower temperatures. While the 20% to 100% SOCs exhibit consistent patterns across both cells (especially for Cell 2), the 0% SOC responses deviate significantly - displaying either contrary behaviour in Cell 1 or a greatly diminished response (Cell 2) from below 30 °C and 25 °C, respectively. This behaviour is clearly reflected in the absolute TOF measurements shown in Figures 7.3a and 7.3e.

7.3.2 Relationship between time-of-flight and temperature

As a linear relationship between temperature and the TOF has been shown for a peak (Figure 7.2d), this was confirmed using an AScan by comparing the ratio of the TOF of a peak at a given temperature to a reference temperature TOF_{ref}:

$$\frac{TOF}{TOF_{ref}} \tag{7.7}$$

In this case room temperature, 20 °C, was used as the reference temperature. The ratio for all cells, for all SOC are shown in Figure 7.4, where the solid lines represent the mean ratio, whilst the shaded areas represent the spread of the ratios across all peaks. The dotted lines mark the boundaries of the two standard deviation range.

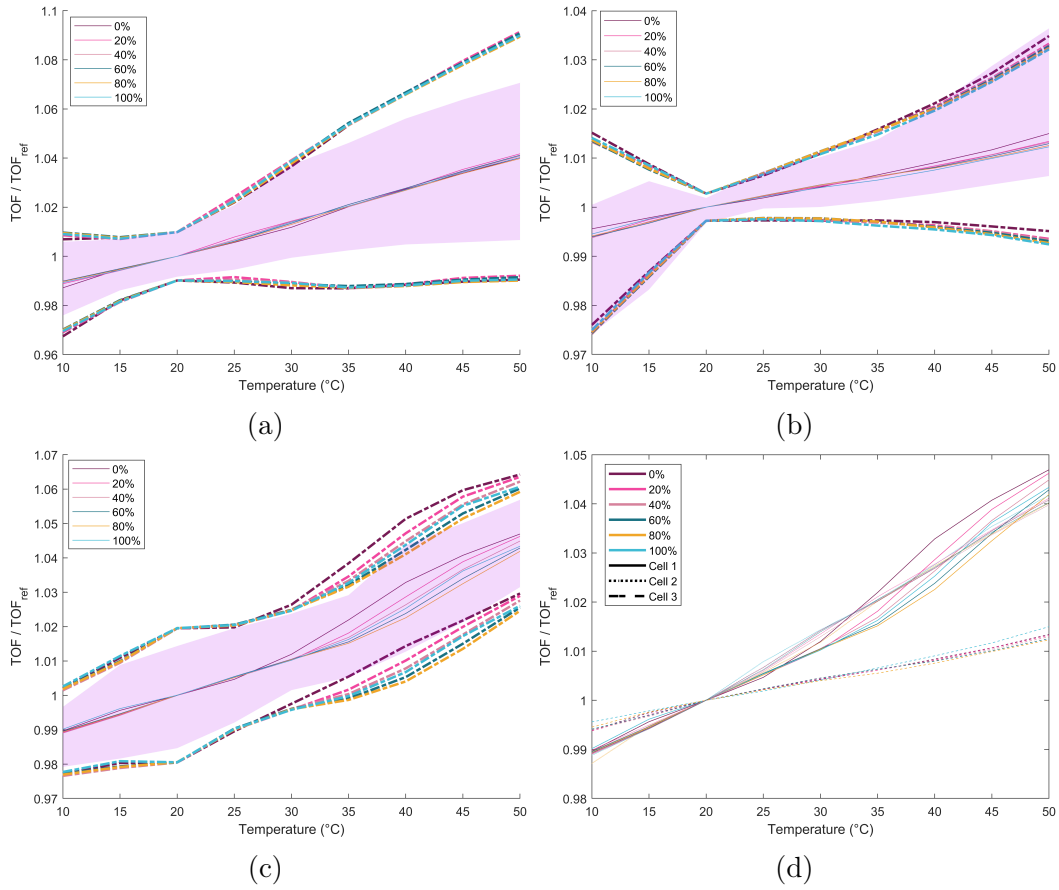

Figure 7.4: The ratio of TOFs (solid lines) for different SOC for a) Cell 1, b) Cell 2, and c) Cell 3, d) a comparison of the three cells. The pink shaded regions represent the spread of the ratios. The dotted lines enclose the regions within two standard deviations.

The mean ratios represent the average values for all peaks identified in the AScan of each respective cell; for instance, the mean ratio at 50 °C and 0% SOC in Figure 7.4a represents the average of all peaks detected in that specific cell condition. The shaded area is defined by the largest and smallest ratio observed across all SOCs, showcasing the spread.

The figures demonstrate a linear relationship between TOF and temperature across all peaks in the tested cells, with each cell showing the same linear trend and slope as temperature increases, regardless of SOC. The mean square error (MSE) for all SOCs across all cells is presented in Figure S1 (See Appendix A), with the largest MSE (2.49×10^{-5}) occurring between 0% and 100% SOC for Cell 3. However, the slope is not consistent across cells, as seen in Figure 7.4d, where Cell 2 has a shallower slope compared to the other cells. Cells 1 and 3 show remarkable agreement in their gradients.

Despite the good agreement in the mean trends, the spread suggests a wide variation in measurements across the acoustic response.The ranges exhibit decreasing values as temperature approaches 20 °C (with the inverse occurring at other temperatures),

although fluctuation amplitude varies between cells and temperature conditions; to evaluate the significance of this spread and validate the ratio's utility, we calculated two standard deviations for all trends (shown as dotted-dashed lines in Figures 7.4a, 7.4b and 7.4c). The shaded areas, which represent the maximum spread across all SOCs, are largely confined within two standard deviations, indicating a tight distribution of the ratios relative to a reference temperature near the mean values. For Cells 1 and 2, the standard deviations followed a similar trend to the data spread, albeit with a generally sharper slope. The viability of this ratio appears to improve as the temperature deviates from 20 °C. Meanwhile, Cell 3 saw a more linear pattern for the standard deviation, also similar to associated data spread. This was still constrained to within the two standard deviation however, showing the data spread is still tight around the mean values.

LIBs naturally undergo capacity fade through normal operation [269], which is accelerated through abusive operation or conditions such as high temperature. As the cell ages, the TOF is observed to undergo a shift that is independent of the change in SOC and temperature. This shift was found to increase or decrease, depending on the cell chemistry [92, 96]. The difference in TOF between fully charged and fully discharged as the cell degraded was negligible over 100 cycles of 300-cycle lifespan cells [179]. It could be hypothesised from this that this work that the ratio of $\mathrm{TOF}/\mathrm{TOF}_{\mathrm{ref}}$ could be consistent as the cell ages, though further experiments are needed to test this.

The physical, and therefore electrical, properties of a cell within a manufacturing batch are dependent on the production process, resulting in variations in the electrical properties of cells of the same manufacturing batch [269]. When comparing the ratios between cells in Figure 7.4d, this variation is observed as Cells 1 and 3 have comparable slopes, while Cell 2 has a shallower slope, but there is little variation between the SOCs within a cell. This variation in performance should be accounted for not only for acoustic monitoring, but as a general consideration when purchasing cells.

7.3.3 Sensitivity analysis

To delve deeper into the interaction and influence of the charge and temperature, we conducted a Global Sensitivity Analysis (GSA) using a variance-based decomposition to calculate the Sobol' indices [270]. This approach quantifies how input variables (in this case temperature and SOC) contribute to the output's variance both independently and through interaction. It decomposes the total variance into first-order effects (individual contributions of each input) and higher-order effects (interaction between inputs), calculating indices that represent the fraction of variance explained by each effect. Whilst we can see that both influence the acoustic signal, the individual effects of each are not clear; the acoustic signal is a superposition of the two variables. The co-dependent effect, or interaction between the two variables, is also unknown. Each output is a peak from the acoustic response, and the inputs are temperature and SOC. Each output had 54 data-points, as it was the combination of the nine temperature and six charge states. In order to present the data, each output in Figure 7.5 is an average across these 54 data-points

Although it is clear both temperature and state-of-charge (SOC) influence the acoustic signal, their individual and coupled effects are challenging to distinguish because of the superposition of their influences. Because the acoustic response changes result from both temperature and SOC variations, we treated each peak of the AScans as a separate output in our analysis. Given nine temperature and six charge states were measured, each output was an average of the combined 54 data points. When performing the analysis, the data is randomly divided into k subsets to apply k-fold cross-validation [271]. To balance between the number of data points per output and computational costs, the number of k-folds used was 27. Using a large number reduces the bias of a specific data subset. The sensitivity indices presented in Figure 7.5 represent the averages between these measurement points.

The results from the GSA are summarised in Figure 7.5, where the first order Sobol' indices for the charge and temperature influences on the TOF are presented. Across all three cells, temperature dominates the TOF changes compared to the SOC, which agrees with the results shown in Figure 7.3. The substantial difference in magnitude between input variables is noteworthy, with SOC accounting for merely 10% of ultrasonic variation, attributable to the narrow spacing observed between 20% and 100% SOC across the cells. There was an expected shift to a quicker TOF as the cells were charged, but this was overshadowed by the temperature, more noticeably in the higher temperature range (7.3c and 7.3g). A change of 10 °C would have the same effect on the TOF as full (dis)charging of the cell. This temperature difference could be achieved during normal operation [179], or exceeded if the C-rate is large enough. The number of peaks vary between the cells due to the cells. Limited coordination between manufacturers results in variation in cell-to-cell manufacturing, such as the amount of active material and discontinuities within the active materials [179].

Recall that the data shown in Figure 7.4 suggested insignificant influence from a combination of the charge and temperature. We used the GSA to confirm this co-dependent interactions by calculating the second-order Sobol' indices, looking at the second-order indices shows a similar result to the ratio of TOF to TOF_{ref}. The interaction between the two inputs has statistically zero effect on the TOF, evidencing that although temperature and charge individually influence the TOF, their interaction does not have a detectable impact. It should be stated that the internal heat generation from the resistance to ionic movement was not explored in this work, as the C-rate was kept low.

The shaded areas surrounding the first-order and second-order indices represent the uncertainty in our sensitivity measures, quantified as one standard deviation calculated through k-fold cross-validation analysis. These uncertainty bounds remained consistently narrow across all three cells for both first-order and second-order indices, with each peak's standard deviation averaged across the individual outputs. The tight spread indicates statistical stability in our partitioning of the variance between temperature and SOC effects. This statistical robustness, demonstrated through repeated cross-validation sampling, validates both the performance of the model and the reliability of our sensitivity measurements, lending additional support to our findings of the dominating effect of temperature on the acoustic signal compared to the SOC.

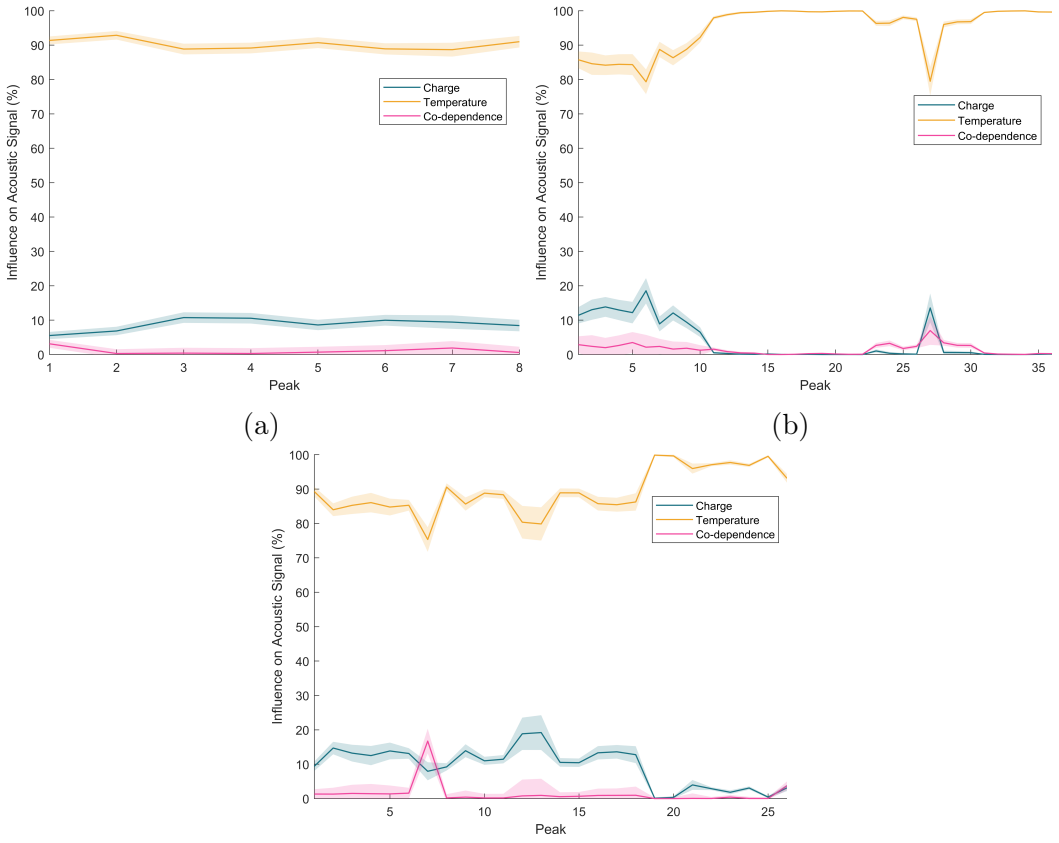

Figure 7.5: First-order Sobol' indices for charge (blue) and temperature (orange) for a) Cell 1, b) Cell 2, and c) Cell 3. The co-dependence (second-order) on the two inputs across the three cells are in pink.

7.4 Conclusion

Ultrasound has emerged as a valuable tool for monitoring battery performance, yielding information through transmission and reflection measurements of internal active materials. Although these investigations have resulted in significant developments, a deeper understanding of the discrete and coupled influences of thermal and SOC effects on the acoustic signal is required. In this work, a study was conducted on NMC lithium-ion cells to determine the influence of temperature and charge on the TOF of an ultrasonic acoustic signal. The results were collected through a thermal and charge cycle, allowing for a matrix of ultrasonic responses to different states of temperature and charge. We report significant effects of both temperature and charge, presenting evidence that temperature has a greater influence on the acoustic signal changes than charge. The question of co-dependency was also addressed. It was found that the interaction between temperature and charge is negligible and was significantly less than the individual influence of the two. We believe that our findings will bring attention to the mostly disregarded effects of temperature when using acoustics monitoring. Addressing this would accelerate the development of

accurate acoustic LIB SOC estimations in tandem with current BMSs.

Work should be conducted to isolate the dominance of the influence of temperature to make this technology viable for industrial application. The temperature and SOC of a cell have statistically independent effects on the acoustic TOF, implying the isolation and decoupling of the two inputs should be possible, deconvoluting one from the other using a ratio similar to the method performed by Owen et al. [174]. However, this method requires a thermocouple throughout the use of the cell or a method for statistical inference.

In order to progress this work, further testing should be performed at higher C-rates, and with continuous cell charging/discharging, to investigate the co-dependency of internal heat generation as a result of the resistance to ionic movement during operation.

Chapter 8

Acoustic Assessment of Lithium-Ion Batteries: Regression Modelling of Li-ion Battery State-of-Charge and Temperature

Abstract

Lithium-ion batteries require accurate state-of-charge and temperature monitoring to ensure safe operation and optimal performance across applications from electric vehicles to grid-scale energy storage. Current battery management systems rely on multiple sensors and electrical measurements that cannot directly probe internal electrode conditions. Ultrasonic monitoring offers a promising non-invasive approach to measure material property changes within operating batteries. However signals are complex because of the superposition of internal multi-layer reflections, and existing methods lack the sophisticated data processing needed for reliable state estimation.The integration of machine learning algorithms with ultrasonic measurements for battery state estimation remains unexplored. Here it is shown that linear regression models applied to ultrasonic time-of-flight measurements from a single piezoelectric crystal can accurately estimate the state-of-charge and temperature, achieving mean absolute errors of 0.40% for state-of-charge and 0.03°C for temperature in this proof-of-concept study. Contrary to expectations that complex non-linear models will be necessary, we found that linear regression outperformed Gaussian process regression when generalising to independent test cycles, demonstrating robust state-of-charge estimation with the added capability of simultaneous thermal monitoring. Furthermore, the robustness analysis reveals that the method tolerates realistic noise levels up to 15% and maintains critical temporal information, and that a single acoustic sensor can provide multiple monitoring functions traditionally requiring separate instrumentation. This proof-of-concept establishes the feasibility of machine learning-enhanced ultrasonic monitoring that could simplify battery management systems by reducing sensor requirements whilst providing direct measurement of internal electrode material changes. This approach demonstrates the first application of machine learning to ultrasonic battery monitoring, potentially enabling more streamlined battery management architectures with fewer monitoring components. It is anticipated that this combined acoustic-algorithmic approach will advance next-generation battery management systems by offering multi-parameter monitoring through simplified instrumentation, particularly valuable as battery applications demand more sophisticated state estimation with reduced system complexity.

Keywords: Machine learning, ultrasound, lithium-ion battery, monitoring, regression modelling

8.1 Introduction

As the energy sector moves towards carbon neutrality, the need for energy storage from renewable sources is becoming more prevalent. A widespread solution is lithium-ion batteries (LIBs), as a result of their competitive price, long operational lifespan, and high energy density [272–274]. Rapid growth in LIB production has led to the development of multiple methods of battery monitoring and management through battery management systems (BMS) [275, 276]. The implementation of a BMS can increase the longevity and safety of LIBs by measuring temperature, estimating the state of charge (SOC) and the state of health (SOH), and performing fault diagnostics [277–279]. There are numerous methods for battery estimation and evaluation employed by BMSs. However, these suffer from technical challenges such as limited measurable signals and time variability [280]. There is also the difficulty of temperature playing a large role in the cycling performance of LIBs by affecting the material properties of the active materials [281].

SOC is defined as the available capacity compared to the capacity when a battery is fully charged, and is represented as a percentage [39]. Various techniques have been developed to estimate SOC. These techniques base the estimations on directly monitored metrics such as coulomb counting or voltage [52, 282, 283], based on models, such as electrochemical impedance spectrometry (EIS) or equivalent circuit (ECM) [188, 284, 285], data-driven physics-based models [286, 287] and hybrid models [288].

Direct monitoring, such as open circuit voltage (OCV), coulomb counting (CC), and internal resistant (IR), utilise readily available parameters such as battery voltage, current, and internal resistance to estimate the SOC, respectively. These methods are simple, and as such are commonly employed for battery characterisation [289]. Coulomb counting has become the standard for SOC estimation in industry [287], due to its high accuracy for short term calculations.

EIS can provide accurate analysis of electrochemical processes, due to the strong relation between the impedance spectrum and battery chemistry [290]. This can be established using an ECM with parameters determined from the impedance data [291]. However, the impedance is sensitive to temperature differences. Real-world scenarios, such as EVs, tend to have irregular charging cycles and are not in temperature controlled environments, reducing the suitability of EIS for *in-situ* applications [39, 292].

Data-driven models, such as neural networks (NNs) and Gaussian processes (GPs), have been widely used in academia and industry for image recognition and result prediction [293, 294]. When applied to SOC estimation, data-driven models have the advantages of being chemistry agnostic, not needing predefined outcomes, and not requiring an accurate electrochemical state inside the battery [295, 296]. Each method has their its benefits, such as deep learning NNs being able to extract complex feature information [297] and GPs being able to use many dimensions to account for a large number of variables [298]. They aren't without challenges however - some models require large datasets to ensure accuracy, some need stable data for accurate operation and some are computationally intensive which current BMSs are ill equipped to handle [288, 299, 300].

An alternative method to direct monitoring was developed by Sood in 2014 [249]

based on the response to ultrasound. The method exploits the variation in the material properties of the electrodes as a battery undergoes charge and discharge. This method has since seen an increase in interest [6, 7, 179]. As found in [178], the relationship between temperature and the acoustic response in LIBs is understudied, as well as the greater battery monitoring field [295]. Our work combines ultrasonic measurements of internal electrode material changes and the improved accuracy of machine learning, GPR and linear regression (LR), to present the application combined accurate, real-time estimations of SOC and temperature through the use of a single piezoelectric crystal. This represents the first investigation combining machine learning (ML) with ultrasonic monitoring for LIB state estimation.

8.2 Results

This section presents the results of robustness of the ML models when controlling different parameters. First, the training and initial performance between the two models using a baseline dataset is investigated. The model with better performance is taken forward to test the stability of the estimation accuracy with different training datasets using single and dual charge cycles. Then, the model is assessed by controlling the amount of Gaussian noise, the charge cycle used for training, the stability across the multiple testing charge cycles, as described in Section 8.4, and the formatting of the ultrasonic wave. For all results, the comparison of the predicted values and the recorded results are presented and analysed. Table 8.1 presents an overview of the variables that were controlled.

Table 8.1: Overview of All Combinations of Variables

Variable	**Levels**	**Count**
Batteries	Battery 1, Battery 2	2
Number of Training Cycles	1, 2	2
Testing Cycles	1–5	5
Gaussian Noise	0%, 5%, 10%, 15%	4
Wave Formats	All, Averaged, Randomised, Two Peaks	4
Total Combinations	$\mathbf{2 \times 2 \times 5 \times 4 \times 4}$	**320**

8.2.1 LR vs GPR Training

The two models were trained on a combination of one and two charge cycles. The inputs were the ultrasonic peak TOF values, and the outputs were the SOC and temperature. This comparison aims to identify the most suitable approach for generalisation to independent test cycles. Figure 8.1 shows the combined results of the 20 folds used for cross-validation. The LR model showed consistency across the folds (Figures 8.1a and 8.1b), indicating no dependency on specific data subsets or training sets. This suggests

a linear relationship between the TOF of the peaks and both SOC and temperature. The consistency across the folds suggests the model has learned the general patterns of the ultrasonic behaviour. Table 8.2 summarises the performance metrics of the models.

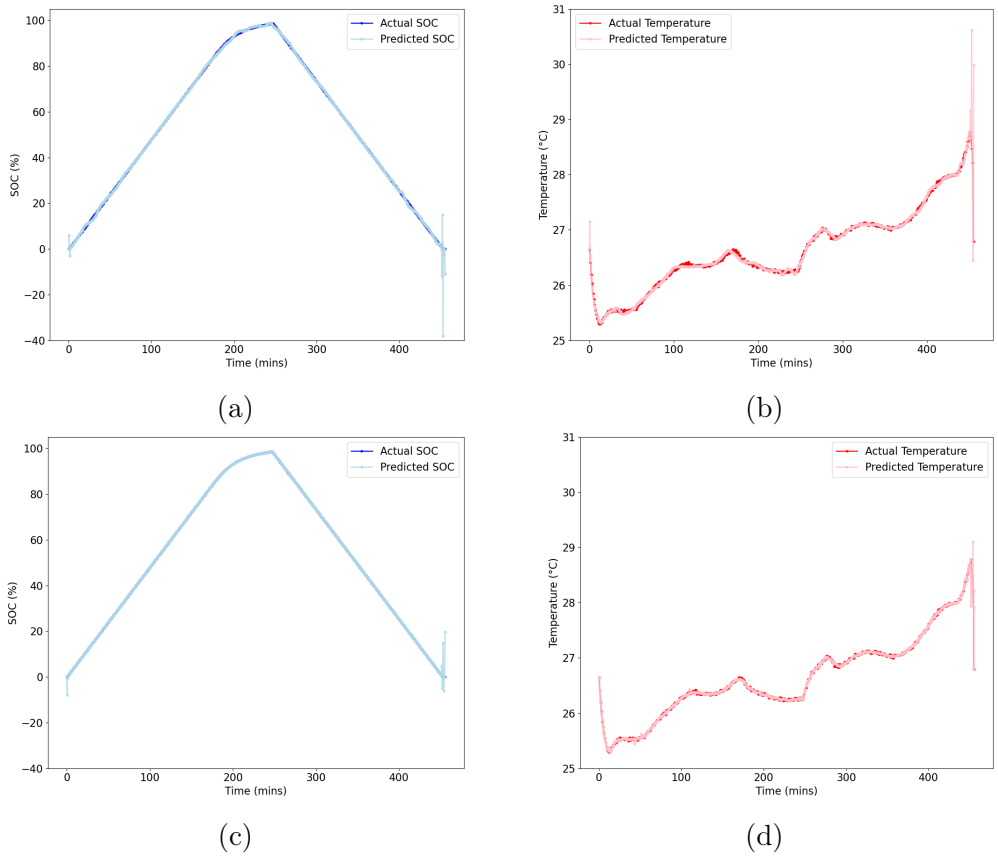

Figure 8.1: Training results from 20-fold cross-validation showing: a) LR SOC estimation, b) LR temperature estimation, c) GPR SOC estimation, and d) GPR temperature estimation.

	SOC		Temperature	
Model	MAE	RMSE	MAE	RMSE
LR	0.4%	1.54%	0.03 °C	0.15 °C
GPR	0.08%	0.91%	0.02 °C	0.06 °C

Table 8.2: Model training statistics.

Figure 8.1a demonstrates that whilst the linear model achieves high SOC accuracy, inconsistencies appear at charge cycle boundaries where the predictions have a larger range. The uncertainty bands reveal the model's limitations in capturing non-linear behaviour during the beginning of charge and the end of discharge. Temperature

estimation (Figure 8.1b) shows the linear model tracking the general thermal profile adequately, but with similar errors at the charge cycle boundaries.

The GPR results reveal substantial relative improvements despite both models achieving good absolute performance. For SOC estimation (Figure 8.1c), the GPR delivers an 80% reduction in mean absolute error (MAE) and halves the root-mean-square error (RMSE) compared to the linear approach. This improvement is particularly valuable given that even small SOC estimation errors can compromise battery management decisions. Temperature prediction (Figure 8.1d) shows more modest but still significant relative gains, with the GPR reducing the MAE by a third and the RMSE by 60%. While the absolute temperature errors are already small for both models, the superior performance of the GPR indicates meaningful non-linearities in the thermal response that warrant the increased model complexity.

The performance gains suggest that whilst a strong linear foundation exists in the ultrasonic-battery relationship, accounting for non-linear components provides measurable improvements. Given the already high accuracy of both approaches, the enhanced performance of the GPR demonstrates that the system contains exploitable non-linear patterns that may justify the computational overhead for more precision-critical applications.

8.2.2 Initial Test Performance

Whilst the cross-validation results give confidence in the capability of the two models, they do not provide the full picture. Cross-validation can mask generalisation failures, particularly in novel applications where model behaviour on independent data may differ substantially from training performance. This requires using an unseen testing dataset, which is presented in Figures 8.2 and 8.3. This dataset uses the earliest charge cycle selected for testing purposes, has no added noise and uses all available TOF peaks for both testing and training. Figures 8.2a and 8.2b are the model estimations compared to the experimental values, whilst Figures 8.2c and 8.2d provides the respective residual parity plots comparing the capabilities of the models to the true values across the charge cycle.

The test results reveal that, as expected, the use of an independent cycle reduced the accuracy of the estimation. The comparison plots show that for LR, the SOC and temperature estimations closely follow the experimental values during charge, with a slight deviation towards the end discharge. This is most noticeable at the end of the charge cycle, which is exaggerated with respect to Figure 8.1a.

Hysteresis is observed within the charge cycle (Figure 8.2c), with the charging stage overestimating and the discharging underestimating. This aligns with previous work that has found hysteresis in the TOF between charge and discharge grows as a cell is cycled [201]. Within this hysteresis, the discharge cycle will result in a larger TOF, and the opposite is true for charging. As the model did not account for this, the inverse is observed. The hysteresis is not present in Figure 8.2b, but discharging has a higher average temperature over charging. This has been observed in [301, 302], where discharging has a higher heat generation over charging. It is also seen that the end of discharge sees a large spike in temperature, resulting in non-linear behaviour

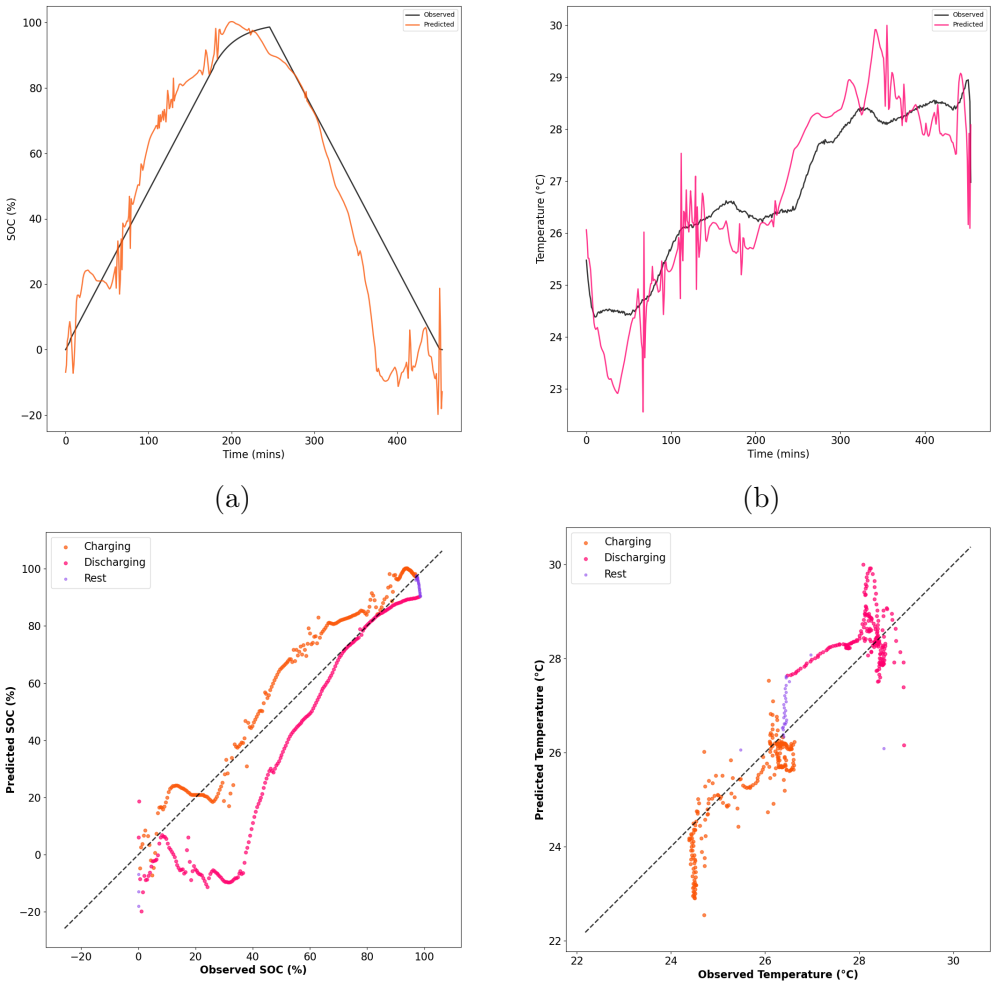

Figure 8.2: Performance of LR when estimating a test charge cycle.

that may be the cause of the error observed in the model.

Despite this, both the SOC and temperature saw predictions close to the true values with high r^2 values above 0.85. The predictions show good accuracy with fairly low RMSE and MAE values of 14.53% and 10.57% for the SOC, and 0.7 ℃ and 0.56 ℃ for the temperature. In contrast, the test cycle revealed areas for GPR development (Figure 8.3). The SOC and temperature estimations in Figures 8.3a and 8.3b reveal considerable deviations from experimental measurements throughout the charge cycle, resulting in a somewhat flat line around 60% SOC. The temperature estimation similarly suggests compromised accuracy, with a plateau being reached around 27 ℃. These results suggest GPR may require larger training datasets to achieve optimal generalisation, presenting an opportunity for future investigation.

The parity plots in Figures 8.3c and 8.3d further illustrate the GPR model's limitations, exhibiting more widely distributed predictions and lower correlation coefficients versus the LR results. Whilst the GPR model captured calibration data

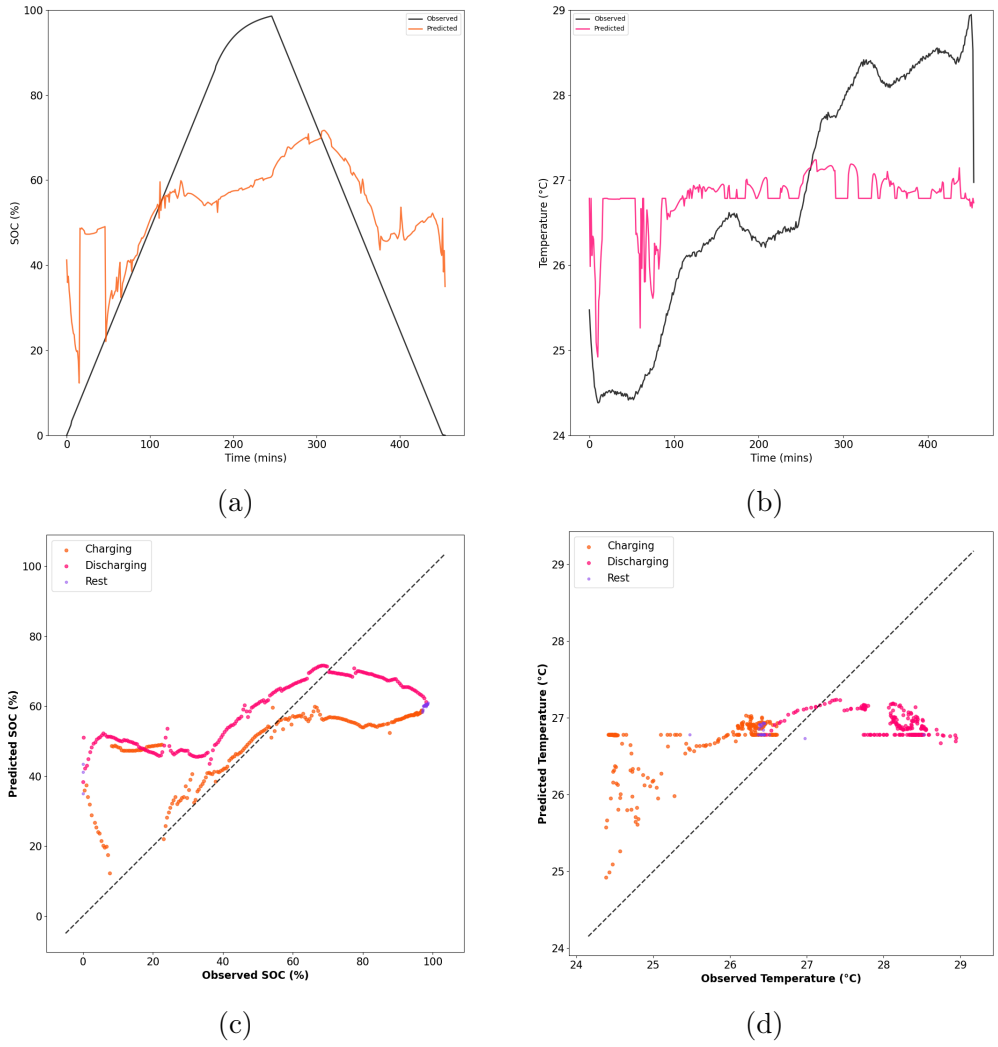

Figure 8.3: Performance of GPR when estimating a test charge cycle.

characteristics effectively during cross-validation but struggled to generalise these relationships to independent test cycles. This behaviour indicates that the increased model complexity was beneficial for fitting training observations. However, it may have resulted in over-fitting to cycle-specific patterns rather than learning the underlying ultrasonic-battery relationships. GPRs perform better when given from large training datasets to provide robust predictions, which was not the case with the limited training datasets used.

Overall, the high predictive accuracy shown by the LR model over the GPR enables confidence in the capabilities in the technique, and therefore will be further investigated in this work. In order to test the stability of the model, the effect of changing the charge cycles used for training and testing will be investigated. The first robustness test examined whether performance is consistent across multiple sequential charge cycles. This is not to dismiss the GPR, as the performance may improve with larger training datasets.

Additionally, the computational efficiency differs markedly between approaches. LR provides real-time prediction capabilities suitable for embedded BMS applications, whilst GPR requires substantially more computational resources for both training and inference. For proof-of-concept development, this computational advantage further supports LR selection for subsequent investigations.

8.2.3 Testing Cycles

A low number of five sequential charge cycles were chosen for model testing to minimise cell degradation effects. This section examines the performance of the model estimating across the different test cycles. Figure 8.4 presents the comparative results, revealing a cycle-dependent variability.

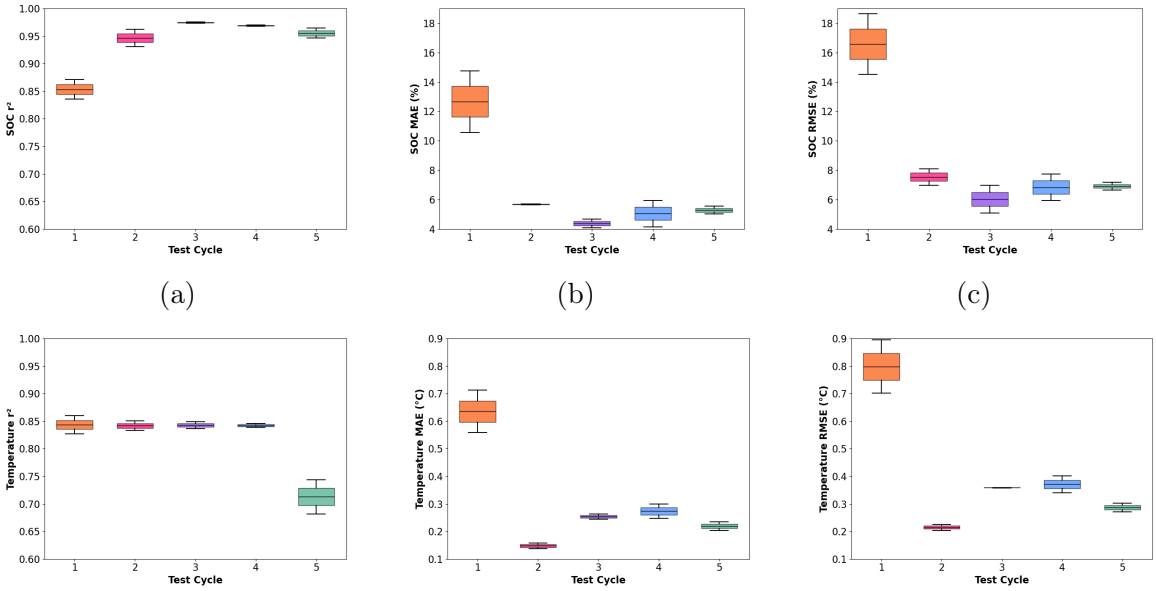

Figure 8.4: Performance of the LR model over multiple, independent testing charge cycles for SOC (a, b, c) and temperature (d, e, f).

Figures 8.4a and 8.4c show the SOC model had worse performance for the first cycle ($r^2 = 0.85$, RMSE = 16.7%). This is still a reasonable Pearson correlation value, though the RMSE is significantly larger than the training. This is shadowed by the later cycles; cycle 2 got scores of $r^2 = 0.95$ and RMSE = 7.4%, and cycle 3 achieved the best scores out of the five with $r^2 = 0.97$ and RMSE = 6.2%. The performance remained high for cycles 4-5 ($r^2 = 0.96$-0.97, RMSE = 6.8-7.0%). This showcases repeatable behaviour across multiple charge cycles that can be exploited with this model. However, this is limited to cycles temporally close to the training cycles. The variation in the ranges and mean values of the MAE plot, shown in Figure 8.4b, is very similar to the RMSE plot; the main difference is that the MAE averaged 2% lower than the RMSE for all cycles. This suggests the model has accurately learnt the patterns between the TOF and temperature, but the charge cycle boundaries are the

main limitation and the cause for the increased error margins whilst having a limited effect on the Pearson correlation (see Section 8.2.5 for further details).

Figure 8.4d presents the temperature predictions having similar behaviour, yet slightly worse performance, to the SOC. The r^2 values were equal across the first four cycles, ranging from 0.84-0.85, and cycle 1 exhibits similar anomalous behaviour in the error performance metrics. However, unlike the SOC estimation, the temperature estimation shows clear degradation in cycle 5 ($r^2 = 0.74$). Figure 8.4f reveals the RMSE remains comparable to earlier cycles. The temperature effects on TOF exhibit greater non-linearity than SOC effects. It should be noted that it remains reasonably linear. Similar to the SOC, Figures 8.4f and 8.4e show the RMSE and the MAE of the temperature estimations are similar in shape and magnitude, varying by a maximum of 0.2 ℃. This again showcases the solid understanding of the relationship between temperature and the TOF, limited largely by the charge cycle boundaries which affects the SOC estimations more than the temperature (discussed further in Section 8.2.5).

The consistently larger error metrics observed in cycle 1, and to an extent cycle 4, suggests that the ultrasonic signal behaviour varies between charge cycles. This phenomenon possibly reflects differences in the electrochemical or material properties of the electrodes, where the stress generation and recovery may vary as a result of multiple conditions. The acoustic properties measured through TOF may be influenced by lithium redistribution, electrode surface conditioning, or thermal equilibration effects.

This proof-of-concept suggests that SOC and temperature estimation may be feasible across multiple charge cycles when tested on the same single charge cycle. Despite this, the estimations at the charge cycle boundaries are greatly unpredictable, increasing the overall error margins of the model. As this is localised to the extreme boundaries, this suggests that ultrasonic-based battery monitoring systems has the capacity for general estimation of temperature and SOC over short-term cycling. Having established that LR maintains reasonable accuracy across consecutive cycles, we next investigated whether increasing the training dataset size could improve generalization performance.

8.2.4 Training Cycle

This section investigates how the number of training cycles affects the LR model performance. ML algorithms benefit from an increase in training data, as the recognition of the generalised patterns prevents over-fitting to specific behaviours. The five testing cycles were used to compare the performance of the model, which are illustrated in Figure 8.5.

From Figures 8.5a and 8.5d, and Table 8.3, the number of training cycles had inconsistent effects on the capture performance of the experimental data. For the SOC, the single cycle training datasets had a slightly lower average r^2 value compared to the dual cycle, yet the cycle outlier saw an increase in error with the increase in training data. The inverse is true for the temperature; the dual cycle had a better r^2 value for the outlier than the single cycle, but the average correlations saw a minimal reduction compared to the single cycle. The outliers have been identified as cycle 1 for the SOC and cycle 5 for the temperature, as seen in the previous section. The

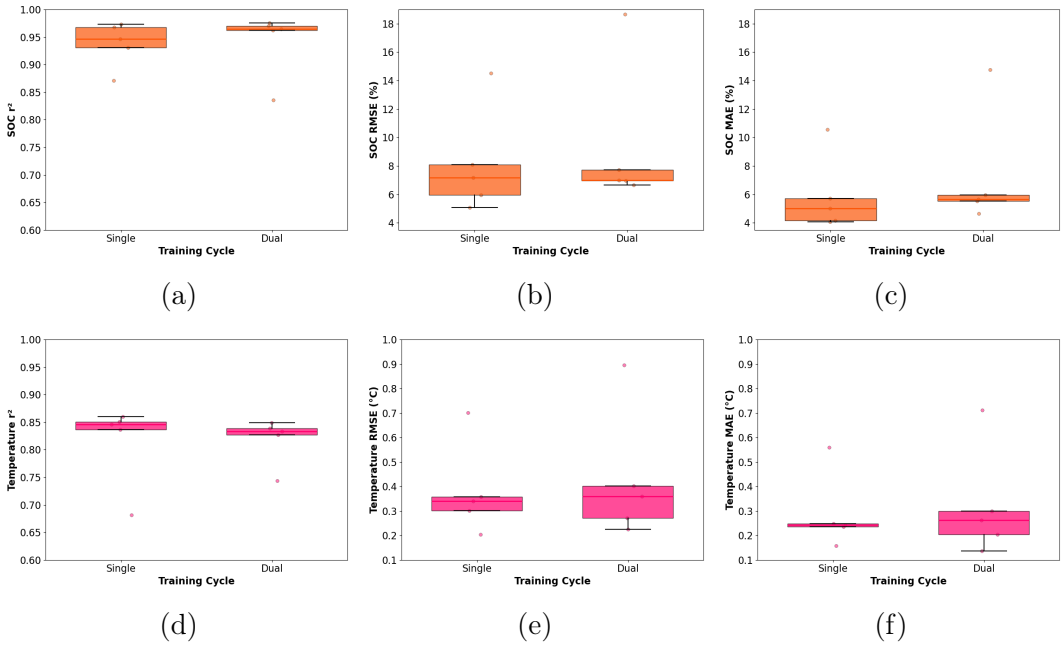

Figure 8.5: Performance of the LR model over one and two training cycles for SOC (a, b, c) and temperature (d, e, f).

other four cycles are closely packed together, with the clusters becoming tighter for SOC with the addition of another training cycle, whilst seeing little improvement for temperature. It should be stated that the overall changes in between the single and dual cycle training datasets in absolute terms are minimal, suggesting limited benefit with improving the fit of the model.

	SOC			Temperature		
Training Cycles	r^2	RMSE	MAE	r^2	RMSE	MAE
Single	0.94	8.10%	5.92%	0.85	0.38 °C	0.29 °C
Dual	0.97	9.14%	7.33%	0.83	0.43 °C	0.33 °C

Table 8.3: Training cycle statistics.

Moving to the error metrics, Figures 8.5b and 8.5c illustrate a similar result to Figure 8.5a; an improvement in cycle clusters with an increase in training data, and an increase in error for the outlier. Interestingly, the dual cycle in Figure 8.5c includes an additional outlier that is below the box plot. This is due to the limits of the box plot whiskers, being set at ± 1.5 x IQR. The MAE value of the outlier is also tighter to the box plot than the box plot of the single cycle training set. It should be noted that if the box plot was extended to include the bottom outlier, it will have a smaller range than the single cycle training dataset. These plots show the dual cycle training set is less susceptible to high variance in general and provides more stable results compared to the single cycle training set. This is expected as the charge/discharge curve of a

LIB is fairly predictable, as seen in Section 8.2.2. Providing more data for predictable behaviour will improve the accuracy of a model, which has been demonstrated here. The increased error in the outlier is likely due to the irregularities in the specific charge cycle. This does suggests the model was over-fitted to the training cycles, which were near identical. This implies the model will benefit from using charge cycles from various stages in the cell lifetime, and from using data from a large set of batteries to improve robustness. Given this is to be used throughout the life of a battery, increasing the number of batteries is preferential.

In comparison, the temperature estimation errors shown in Figures 8.5e and 8.5f present a different story. The non-outlying cycles saw a tighter grouping for the single cycle training set than the dual cycle. The dual cycle also saw greater errors for the outlier compared to the single cycle. This suggests the variation in temperature between cycles is less predictable than for the SOC, and therefore the model does not benefit from an increase in training charge cycles. The batteries were exposed to ambient temperature changes, such as lab equipment releasing heat during operation. In real world applications, batteries will be located in confined spaces and will be operated at different charge rates. These will have an affect on the temperature of the batteries that will need to be accounted for by the model. A similar story to Figure 8.5c in Figures 8.5e and 8.5f; the single cycle training set saw an outlier below the box plot, but when the box plot is expanded to include it, the box has a smaller range than the dual cycle training dataset. This indicates that despite the temperature model seemingly becomes more variable with an increase in temperature training data, it does improve robustness to edge cases. As the linear model is susceptible to errors around the charge cycle boundaries, an improvement in resilience to this is beneficial.

These initial results suggest both single-cycle and dual-cycle training are sufficient for this proof-of-concept, though future work should investigate optimal training strategies that reduce the potential for outliers. For SOC, an increase in training cycle numbers benefits the model due to its predictable nature, whilst temperature prediction sees a inconclusive improvement. If a charge cycle exhibits behaviour that is not expected, then using sequential charge cycles for training the model is inadequate for addressing this; it rather worsens the estimation. This could be mitigated by using a larger set of batteries or non-sequential charge cycles during training. The larger battery dataset is preferred as it should increase the cycle life of LIBs suitable for this technique.

8.2.5 Noise

This section investigates the effect of noise on the performance of the model, to provide insight into the robustness of the model with regards to realistic operation conditions. Real-world situations expose BMSs to various noise sources. These include electrical interference from other electronics, temperature fluctuations driven by external heating sources and degradation in the bonding or instrumentation of the system. To attempt to account for this, multiple levels of Gaussian noise (0%, 5%, 10% and 15%) were applied to the training data. The noise levels were determined using the standard deviation of the dataset. For example, the 5% noise level was applied by adding a

zero-mean Gaussian deviation with a standard deviation equal to 5% of the original signal's standard deviation to each data point. To have a useful comparison, only the noise level was changed; the model was trained on one charge cycle with all peaks used for estimation. The results of these are shown in Figure 8.6 and Table 8.4, which presents the average statistics of the five testing cycles.

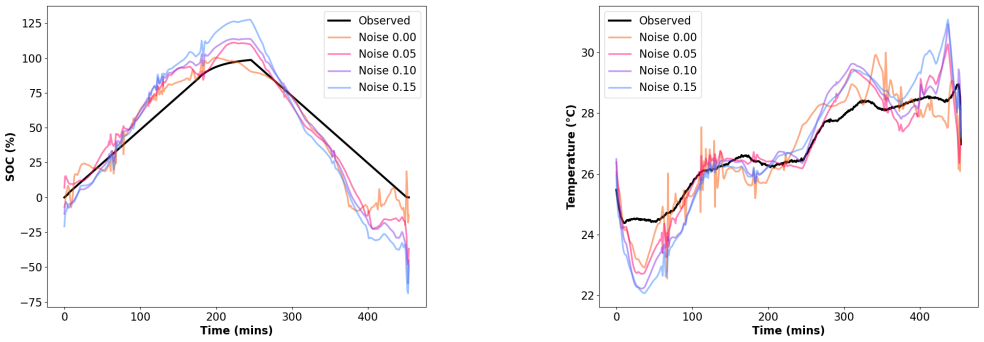

(a) (b)

Figure 8.6: Comparison of Gaussian noise levels on the estimation performance of a) SOC and b) temperature.

The noise levels are compared using the colour of each plot, with the black plot showing the experimental results. The plots illustrate that noise affects estimation accuracy but not the plot shape, with greater noise levels producing larger errors. The overestimation or underestimation remains mostly consistent across all noise levels, as seen with Figure 8.6a, though Figure 8.6b shows exceptions around 400 minutes where 5% and 10% noise levels see underestimation whilst 15% noise shows slight overestimation.

Figure 8.6a reveals noise primarily affects SOC estimation accuracy during transition regions, with limited effect during charge/discharge. Deviations reach +25% at end of charge and -75% at end of discharge for SOC. Figure 8.6b shows similar variation only at charge cycle boundaries, with ± 2 ℃ variation for maximum and minimum temperatures coinciding with cycle start and end. This behaviour was observed in Section 8.2.2, and is likely due to the non-linear behaviour that is observed at the charge cycle boundaries. The increased noise level will result in a larger deviation from a linear fit, resulting in the larger errors observed.

Comparing noise levels reveals interesting behavioural differences between SOC and temperature estimations. Table 8.4 shows the baseline 0% Gaussian noise provides accurate estimations, with Pearson correlations of 0.92 and 0.85 for SOC and temperature respectively, suggesting preference for SOC due to the more predictable nature of charge cycles compared to temperature variation.

The introduction of 5% Gaussian noise produced improvements in SOC estimation correlation, though RMSE and MAE increases indicate worsened prediction error. This provides evidence that the model is over-fitting to the training characteristics at the baseline level. The temperature estimation showed improvement across all metrics,

	SOC			Temperature		
Noise	r^2	RMSE	MAE	r^2	RMSE	MAE
0%	0.92	8.82%	5.90%	0.85	0.42 ℃	0.29 ℃
5%	0.93	10.12%	7.27%	0.89	0.38 ℃	0.25 ℃
10%	0.94	12.78%	9.97%	0.89	0.48 ℃	0.32 ℃
15%	0.93	17.24%	14.36%	0.91	0.55 ℃	0.36 ℃

Table 8.4: Gaussian noise statistics.

further suggesting baseline model was over-fitted to the training temperature, which has been shown to suffer from larger deviations than the SOC. The 10% noise level exhibits similar SOC behaviour, with improved error margins providing evidence of beneficial noise injection or regularisation, though estimation error at extreme ranges becomes more pronounced. The 15% noise level sees overall performance decrease, with largest RMSE and MAE for both parameters.

Figure 8.7 illustrates the parity and residual plots across noise levels. Figure 8.7a demonstrates strong SOC performance with data clustering tightly around the ideal diagonal, though a subtle S-shaped deviation suggests some non-linearity persisting across all noise levels, which is likely due to hysteresis observed in TOF measurements between charging and discharging.

The systematic bias in both SOC and temperature predictions reveals ultrasonic TOF behaviour that linear regression cannot adequately capture, due to non-linear characteristics. The curved residual distribution is characteristic of a model that oversimplifies a fundamentally non-linear relationship, potentially due to the hysteresis behaviour of the TOF mentioned in Section 8.2.1 [201], where the TOF during discharge is greater than during charge.

The consistent bias across all noise levels confirms this is a fundamental limitation of linear modelling rather than a measurement artefact. Cell ageing exacerbates this effect through progressive electrode degradation and mechanical property changes [303]. Since these charge cycles occurred partway through the experimental campaign, accumulated cycling stress will amplify the hysteresis compared to fresh cells, explaining the pronounced ±60% residual range observed. Capturing SOC-dependent hysteresis behaviour requires non-linear modelling approaches. Beyond noise resilience, practical implementation requires understanding how signal processing choices affect performance. The final robustness test examined whether simplified peak processing could maintain accuracy while reducing computational demands. Beyond noise resilience, practical implementation requires understanding how signal processing choices affect performance while meeting computational constraints.

The model shows reduced accuracy at very low SOC values with increased scatter across all noise conditions, but maintains good agreement at high SOC regions, despite estimated values exceeding observed values by up to 25%. Figure 8.7c shows strong predictive performance across the operational temperature range with data forming a tight cluster around the ideal diagonal. The scattering is slightly greater compared

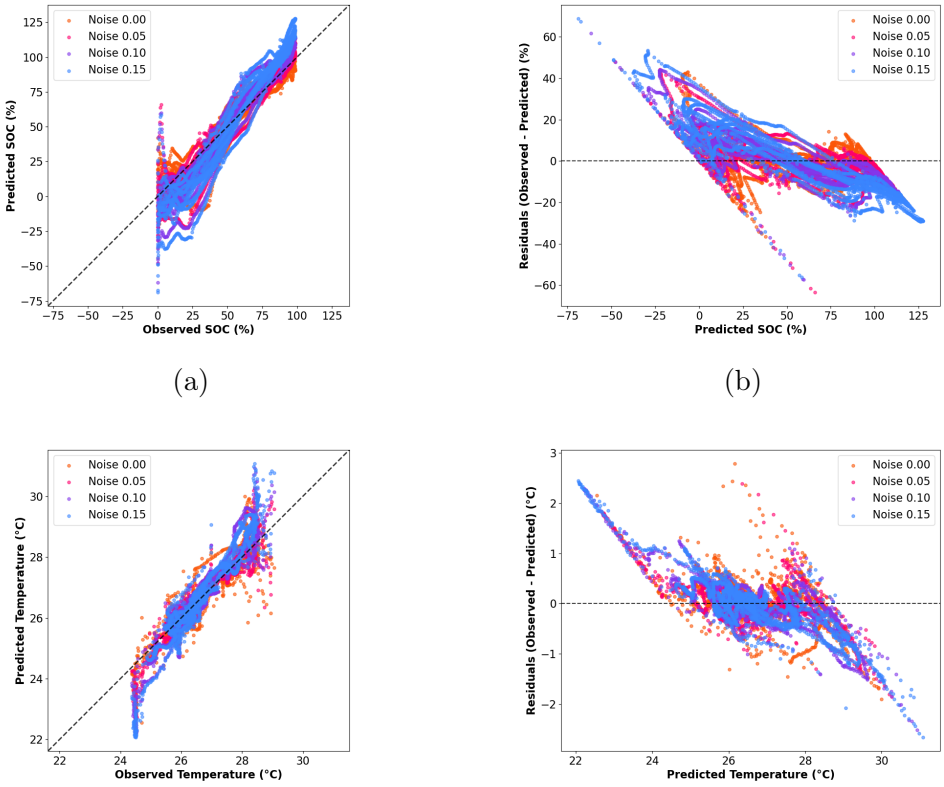

Figure 8.7: Noise level comparisons of the parity plots of the a) SOC and c) temperature, and residual plots of the b) SOC and) temperature.

to SOC, largely at temperature extremes, with maximum deviations ranging from -3 ℃ for lower noise levels to +2 ℃ for higher levels. All noise levels exhibit similar scattering, with the relatively narrow operational temperature range (approximately 9 ℃) resulting in compressed data distribution between 24-29 ℃.

The residual plots reveal systematic patterns providing insights for model development. Figure 8.7b shows curved distribution with residuals ranging from +60% at low predicted SOC to -25% at high values, indicating consistent overestimation below 25% SOC and underestimation above 50% SOC. This bias pattern remains consistent across all noise levels, suggesting underlying ultrasonic-battery relationships rather than measurement noise effects. Figure 8.7d exhibits similar characteristics with more constrained residual range, reflecting the narrower operational temperature window compared to the extended SOC range tested.

8.2.6 Peak Formatting

This section examines how different approaches to formatting and processing the ultrasonic peaks affect model performance. BMSs can have limited computational and memory power, particularly in automotive applications. While ultrasonic data

can provide a large amount of information that can be used for battery estimation, the BMS may not have have the capacity to utilise all of it. Therefore, simplified processing approaches could ease the integration into resource-limited hardware. To investigate this, four formatting methods were compared: using all available peaks (All Peaks), splitting all available peaks into two averaged peaks (Averaged Peaks), randomised the peak order before averaging down to two (Randomised Peaks), and only two selected peaks (Two Peaks). The peak formatting comparison employed identical training conditions: LR model, Battery 1, single training cycle, 0% noise. The results suggests significant sensitivity to peak selection. Figure 8.8 reveals that all reduced formatting approaches introduce systematic estimation errors, particularly at the charge cycle boundaries. A clear observation is keeping the temporal order of the peaks is necessary to ensure high accuracy. Temperature estimation exhibits even greater sensitivity to peak formatting than SOC, with substantial deviations throughout the cycle for reduced formatting methods.

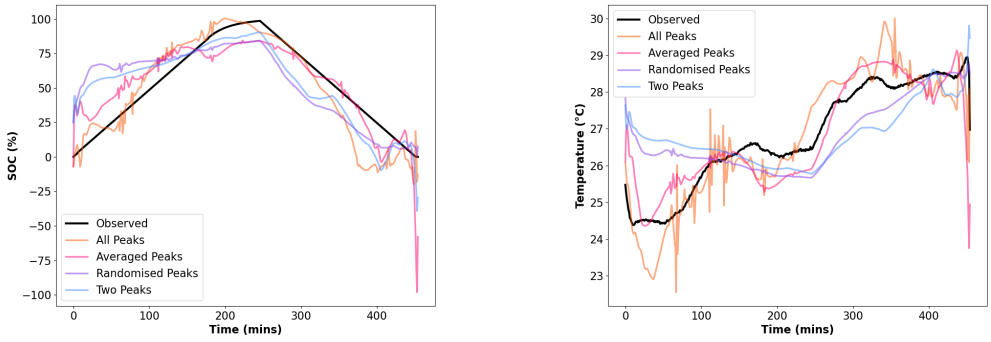

(a) (b)

Figure 8.8: Comparison of peak formatting methods on the estimation performance of a) SOC and b) temperature.

All Peaks established the performance baseline which can be compared to the other formats in Table 8.5. It is the baseline as it had the largest amount of data points available, and therefore has been explored in the previous sections. Averaged Peaks saw a drop in performance, indicating that the individual peaks contain information that is lost by averaging. The comparison between All Peaks and Averaged Peaks indicates that moderate signal processing simplification increases prediction errors, but it is acceptable for the proof-of-concept validation.

Randomised Peaks had the worst performance, suggesting that temporal sequence contains critical information for battery state estimation. The reduced performance when the peak order is disrupted indicates that there is a significant differences in information between the individual peaks, rather than the peaks behave the same. This is due to the travel path and superposition of the peaks; as the TOF increases, the path a peak travels increases and is subject to influence from a larger number of other peaks. This increases the complexity of the peak in question, and this increase seems to not be random given the drop in performance of Randomised Peaks compared to

Averaged Peaks. Two Peaks also yielded poor performance, with a similar estimation shape to the Randomised Peaks. A potential reason for the similar shapes could also be the lack of temporal continuity, as the peaks were deliberately selected from different points in the response. The peaks were still in temporal order, unlike the Randomised Peaks. This is likely the reason for the improvement from Two Peaks.

	SOC			Temperature		
Configuration	r^2	RMSE	MAE	r^2	RMSE	MAE
All Peaks	0.92	8.82%	5.90%	0.85	0.42 ℃	0.29 ℃
Averaged Peaks	0.82	12.95%	9.37%	0.76	0.46 ℃	0.29 ℃
Randomised Peaks	0.65	18.00%	14.81%	0.56	0.62 ℃	0.44 ℃
Two Peaks	0.78	14.06%	11.25%	0.41	0.72 ℃	0.52 ℃

Table 8.5: Peak format statistics.

Figure 8.9 shows that every format had the same underlying bias; SOC saw the same hysteresis as discussed in Section 8.2.2, and the temperature saw a trend to underestimate at higher temperatures and overestimate at lower temperatures. The boundary condition issue was also affected by the formatting, notably at the end of discharge. Interestingly, the worse performer was the Averaged Peaks, despite otherwise giving good results. The combination of the peaks increasing this error could imply the phenomenon causing this is located within a subsect of the peaks, which is in either the first or second half. Randomising the order reduces the impact of this grouping, explaining the improved boundary predictions of Randomised Peaks. This does not apply to the start of charge, as the increase in error aligns with the drop in general performance seen in Table 8.5.

The PCA was applied to all the formatting types after normalisation, which suggests that peak processing choices alter the fundamental information structure in ways that sophisticated mathematical optimization cannot fully compensate for. The reduced performance of Randomised Peaks even after PCA optimization provides further evidence that both the individual peaks and the response as a whole contain different information, and reducing or removing one can affect the accuracy of the model.

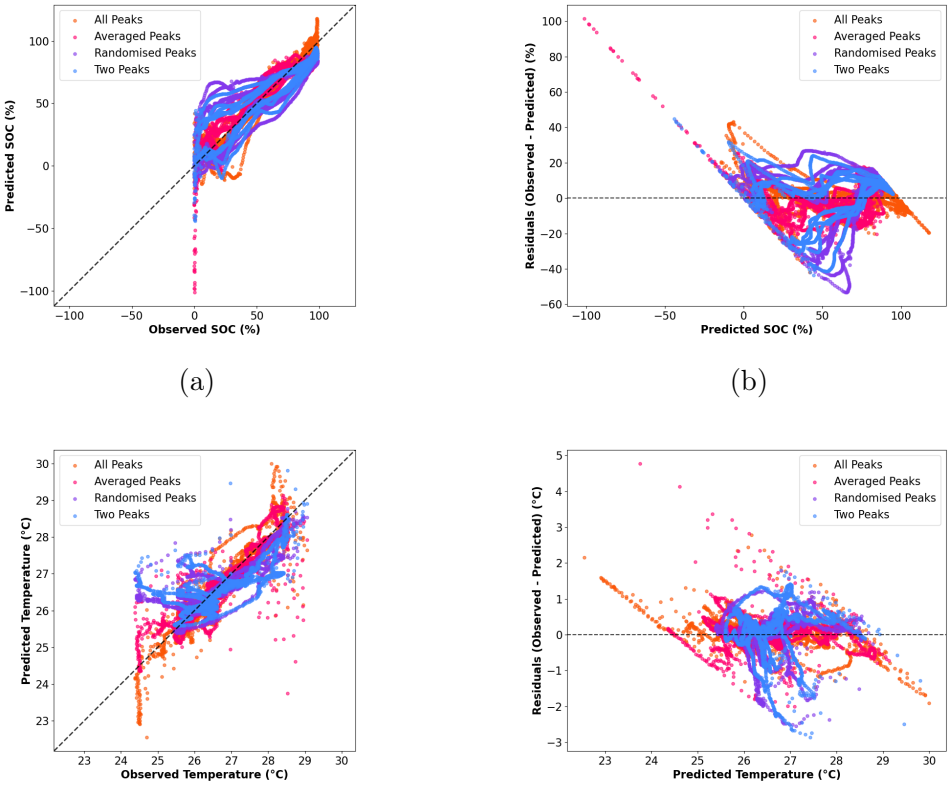

Figure 8.9: Comparison of the peak formatting using parity plots of the a) SOC and c) temperature, and residual plots of the b) SOC and d) temperature.

8.3 Conclusion

Accurate estimations of the state-of-charge and temperature can contribute to the improved safety, longevity and effectiveness of lithium-ion batteries. This study established the viability of estimating the state-of-charge and temperature of lithium-ion cells using regression algorithms trained on ultrasonic data. The models were trained on two sequential charge cycles, and were used to estimate the five subsequent charge cycles. The datasets for this work used a small number of sequential charge cycles from cells that underwent 100 charge cycles in a temperature control chamber. The cycles were split into training and testing cycles, with various levels of Gaussian noise and ultrasonic peak formats. The results successfully demonstrated that the linear regression model was able to provide feasible estimations of these variables under different parameters. It also highlighted the significant impact ultrasonic hysteresis can have on the accuracy of the estimations due to cell degradation. In addition to the findings of this work, this approach has the potential to provide researchers with a wider range of information from within the cell in conjunction with current BMS technologies.

These preliminary tests suggest the approach may be tolerant to noise up to 15%,

though error margins increase primarily at the extremes of SOC and temperature ranges during full discharge and charge states. This behaviour can be attributed to ultrasonic hysteresis effects resulting from changes in the elastic hardening and recovery due to cell degradation, which introduce non-linear characteristics that have limited impact on overall estimation capabilities.

Peak formatting proved more critical to the effectiveness of the model. Whilst the minimum requirement of two tracked peaks yielded poor estimations, utilising all available peaks provided strong correlation and low error margins. Interestingly, randomising peak order rather than maintaining temporal sequence produced similar degradation to using only two peaks, suggesting that individual peak behaviour varies across the signal due to increased complexity from accumulated internal reflections at longer time-of-flight intervals.

Future development opportunities include the use of a larger battery sample size (n>2) and investigation into performance on charge cycles further removed from the training cycles to assess long-term stability. Additionally, the systematic bias observed in residual analysis indicates promising directions for non-linear modelling approaches to better capture the underlying ultrasonic-battery relationships. These findings provide clear pathways for subsequent investigations to validate the approach across larger datasets, diverse battery chemistries, and extended operational conditions.

In conclusion, this research provides initial evidence that machine learning, specifically regression models, may play an important role in the future of lithium-ion batteries; in the potential commercialisation of ultrasonic monitoring, and for the extraction and exploitation of the information-rich data that ultrasound can provide. To develop this further, validation across larger battery populations, implementation of non-linear regression models to address systematic bias, and testing of different chemistries will be necessary to confirm whether these findings can be generalised across lithium-ion technology.

8.4 Methodology

8.4.1 Battery Instrumentation

This work used two lithium-ion pouch cells (designated cell 1 and cell 2). Both cells were sourced from the same supplier (RS Pro, London, England, stock number 125-1266) and shared identical specifications: 2000 mAh capacity, NMC cathode material, graphite anode, and dimensions of 63 $\times$ 43.5 $\times$ 7 mm. To minimise manufacturing variability, the cells were purchased at the same time, coming from the same manufacturing batch and day of manufacture.

Each battery was instrumented with an ultrasonic piezoelectric transducer measuring 10 $\times$ 5 mm (DeL Piezo Specialties, LLC, FL, US) with at a central frequency of 2 MHz. The transducers were permanently bonded to the cell surfaces using a commercial adhesive. The 2 MHz operating frequency was selected based on optimisation studies reported in the literature [7, 82, 206], which found this frequency provided an adequate balance between penetration depth, signal attenuation, and measure-

ment sensitivity. The experimental setup employed a pulse-echo setup, where each transducer functioned as both signal transmitter and receiver. Surface temperature measurements were obtained using thermocouples secured to each cell.

The cells underwent 100 charge cycles at 0.3C, described in [179]. The charge cycles were CCCV; with the cells charging from 3.0 V to 4.2 V at which point the voltage was held until the C-rate dropped to 0.03 C. The cells were then discharged at 0.3C to 3.0 V. The observed temperature range during testing was a result of internal heat generation during cycling.

The cycles used for training and testing for this work were taken from partway through this experiment. This was in order to remove influence from the SEI formation cycles, which could have an effect on the US signal.

8.4.2 Machine Learning

ML is a branch of computer science dedicated to the development of algorithms capable of learning and making decisions based on complex data [304, 305]. ML algorithms use data, either experimental or computational, to explain and predict the behaviour or properties of materials or applications without the need for repeat experiments or computation [306]. There are various techniques that can be utilised by ML, namely: supervised learning; unsupervised learning and reinforcement learning. Supervised learning is used to establish relations between inputs and outputs, unsupervised learning is used to decipher hidden patterns or features in a dataset, and reinforcement learning for performing a specific task through repeated dynamic interactions [307].

Supervised learning techniques were used in this work as the interest was in the relations between ultrasonic time-of-flight (TOF) measurements and battery SOC and temperature. Linear regression (LR) and Gaussian process regression (GPR) are popular supervised ML techniques, and were both employed to investigate the linear and non-linear relationships that have been observed previously [180].

The ML models used in this work were built using the PyCharm (2024.2.3) environment with Python (3.10.0). The codes were written with additional Python packages including, but not limited to: NumPy (1.26.4); pandas (1.5.0); GPflow (2.9.2); TensorFlow (2.10.1); and SciPy (1.14.1). The ML models were developed using the ROMCOMMA software library [264].

To address the high dimensionality of the ultrasonic data, principal component analysis (PCA) was applied to the training datasets. Multiple peaks were selected and tracked from the ultrasonic signal, resulting in a high dimension of inputs. PCA reduces the number of dimensions by rotating the data so that the new axes represent the largest variation in the data (principal components), see Figure 1 [308]. This reduces the computation time without significantly affecting the accuracy of the results [309].

In order to perform the PCA, the covariance matrix $\mathbf{S}$ of the input vectors was calculated using:

$$\mathbf{S} = \frac{1}{N}\sum_{k=1}^{N}(\mathbf{x}_k - \bar{\mathbf{x}})(\mathbf{x}_k - \bar{\mathbf{x}})^T \tag{8.1}$$

where N is the number of data-points, $\mathbf{x}$ represents the ultrasonic peaks per data-point and $\bar{\mathbf{x}}$ is the average ultrasonic value:

$$\bar{\mathbf{x}} = \frac{1}{N}\sum_{k=1}^{N}\mathbf{x}_k \tag{8.2}$$

Since $\mathbf{S}$ is symmetric, its eigendecomposition provides the eigenvalues $\boldsymbol{\lambda}$ and corresponding eigenvectors $\mathbf{V}$:

$$\mathbf{S} = \mathbf{V}\boldsymbol{\Lambda}\mathbf{V}^T \tag{8.3}$$

$$\mathbf{S}\mathbf{v}_k = \lambda_k\mathbf{v}_k \tag{8.4}$$

where $\mathbf{V} \in \mathbb{R}^{p\times p}$ is the matrix of eigenvectors that define the new principal components, $\boldsymbol{\Lambda} \in \mathbb{R}^{p\times p}$ is the diagonal matrix of eigenvalues, $\mathbf{v}_k$ is an eigenvector corresponding to the principal component direction, and λ_k is the associated eigenvalue quantifying the amount of variance along $\mathbf{v}_k$.

The ML models were trained using the reduced-dimension features as inputs to predict SOC and temperature. Both LR and GPR models were implemented to capture different aspects of the relationship between ultrasonic measurements and battery parameters. The methods for training these models employed k-fold cross-validation to assess robustness and prediction accuracy.

K-fold cross-validation with $k = 20$ was implemented for comprehensive model evaluation. While k=5 or k=10 is more standard, k=20 provides additional validation iterations to assess model consistency across data partitions. The dataset was randomly partitioned into 20 equally-sized folds. For each iteration, 19 folds were used for training whilst the remaining fold served as the validation set. This process was repeated 20 times, with each fold serving as the validation set exactly once. Model performance was evaluated using the Root Mean Square Error (RMSE) averaged across all 20 validation folds.

The LR was implemented using the Ordinary Least Squares (OLS) method. As previously stated, it has been suggested that the relationship between SOC and TOF is linear, allowing for the use of the simpler and more efficient OLS approach over methods such as the Generalised Least Squares. The linear regression model was formulated as:

$$\mathbf{Y} = \mathbf{X}\boldsymbol{\beta} + \boldsymbol{\varepsilon} \tag{8.5}$$

where $\mathbf{Y} \in \mathbb{R}^{n\times 2}$ is the matrix containing temperature and SOC observations as outputs, $\mathbf{X} \in \mathbb{R}^{n\times p}$ is the design matrix containing the ultrasonic features as inputs, $\boldsymbol{\beta} \in \mathbb{R}^{p\times 2}$ is the matrix of regression coefficients, and $\boldsymbol{\varepsilon} \in \mathbb{R}^{n\times 2}$ is the error matrix. Here, n is the number of data points and p is the number of ultrasonic peaks.

Unlike LR, GPR is a non-parametric ML method that creates a black-box function, where the underlying mechanism is hidden from the user. Being non-parametric means the data is used directly in the model without assuming a specific functional form. Bayesian conditioning [310] was used to identify the mean $f(\mathbf{x})$ and variance Σ_f using the ultrasonic TOF measurements as inputs and corresponding SOC and temperature recordings as outputs.

In this work, the radial basis function (RBF) kernel was used, which measures the similarity between each pair of input conditions $\mathbf{x}$ and $\mathbf{x}'$:

$$cov(\mathbf{y}(\mathbf{x}).\mathbf{y}'(\mathbf{x})) = k(\mathbf{x}, \mathbf{x}') = \sigma_f^2 \exp\left(-\frac{1}{2}(\mathbf{x} - \mathbf{x}')^T \mathbf{W}(\mathbf{x} - \mathbf{x}')\right) \tag{8.6}$$

where $\mathbf{x}$ and $\mathbf{x}'$ are the input vectors, and the hyperparameters $\mathbf{W}$ and σ_f^2 are the length scale matrix and signal variance, respectively. The GPR uses the kernel to weigh the importance of all previous data, utilising all information across the captured peaks of dataset $\mathcal{D}$.

Once trained, the GPR takes a $(1 \times d)$ row vector as input $\mathbf{x}$ to predict outputs for subsequent charge cycles using the predictive equations:

$$y(\mathbf{x}) \sim \mathcal{N}(\bar{f}(\mathbf{x}), \sigma_f^2 + \sigma_e^2) \tag{8.7}$$

where:

$$\bar{f}(\mathbf{x}) := k(\mathbf{x}, \mathbf{X})(\mathbf{K} + \sigma_e^2 \mathbf{I})^{-1} \mathbf{y} \tag{8.8}$$

$$\Sigma_f := k(\mathbf{x}, \mathbf{x}) - k(\mathbf{x}, \mathbf{X})(\mathbf{K} + \sigma_e^2 \mathbf{I})^{-1} k(\mathbf{X}, \mathbf{x}) \tag{8.9}$$

where σ_e^2 is the likelihood variance accounting for observed noise.

To improve computational stability and efficiency, Cholesky decomposition was employed in both the GLS and GPR models. This method is particularly useful when working with large covariance matrices that require inversion, which can often be a source of numerical error or instability.

In the OLS model, Cholesky decomposition was applied by setting the error covariance matrix to the identity matrix:

$$\mathbf{\Sigma} = \mathbf{I} = \mathbf{L}\mathbf{L}^T \tag{8.10}$$

where $\mathbf{L}$ is a lower triangular matrix. This transformation 'whitens' the data by removing correlated errors, allowing ordinary least squares to be applied more reliably.

In the GPR model, Cholesky decomposition was applied to the kernel matrix $\mathbf{K}$, which describes the similarity between all data points based on the inputs. A small noise term σ_n^2 was added to the diagonal to ensure numerical stability:

$$\mathbf{K}_{\text{reg}} = \mathbf{K} + \sigma_n^2 \mathbf{I} \tag{8.11}$$

This regularised matrix was then decomposed using Cholesky decomposition:

$$\mathbf{K}_{\text{reg}} = \mathbf{L}\mathbf{L}^T \tag{8.12}$$

This decomposition facilitates efficient computation of predictions and evaluation of model fit, particularly when calculating the log marginal likelihood:

$$\log p(\mathbf{y}|\mathbf{X}) = -\frac{1}{2}\mathbf{y}^T \mathbf{K}_{\text{reg}}^{-1} \mathbf{y} - \frac{1}{2}\log|\mathbf{K}_{\text{reg}}| - \frac{n}{2}\log(2\pi) \tag{8.13}$$

where $\mathbf{y}$ is the vector of training values (SOC or temperature), $\mathbf{X}$ is the matrix of inputs, and $|\mathbf{K}_{\text{reg}}|$ is the determinant of the regularised kernel matrix. Each term balances model fit against complexity.

To evaluate the prediction performance of the ML models, three statistical standards were employed:

1) Root Mean Square Error (RMSE):

$$\text{RMSE} = \sqrt{\frac{1}{n}\sum_{i=1}^{n}(\mathbf{y}_i - \hat{\mathbf{y}}_i)^2} \tag{8.14}$$

where n is the number of data points, y_i is the observed value, and $\hat{y}_i$ is the predicted value from the model.

2) Mean Absolute Error (MAE):

$$MAE = \frac{1}{n}\sum_{i=1}^{n}|\mathbf{y}_i - \hat{\mathbf{y}}_i| \tag{8.15}$$

which represents the average gap between the observed and predicted values.

3) Pearson Correlation Coefficient (r^2):

$$r^2 = (\frac{\sum(\mathbf{x}_i - \bar{\mathbf{x}})(\mathbf{y}_i - \bar{\mathbf{y}})}{\sqrt{\sum(\mathbf{x}_i - \bar{\mathbf{x}})^2(\mathbf{y}_i - \bar{\mathbf{y}})^2}})^2 \tag{8.16}$$

where x_i and y_i are the data points, and $\bar{x}$ and $\bar{y}$ are the mean of the x and y values, respectively. As linear regression is used in this work, testing the strength of the linear relationship was deemed appropriate.

Appendix A

MSE of ultrasonic time-of-flight and temperature

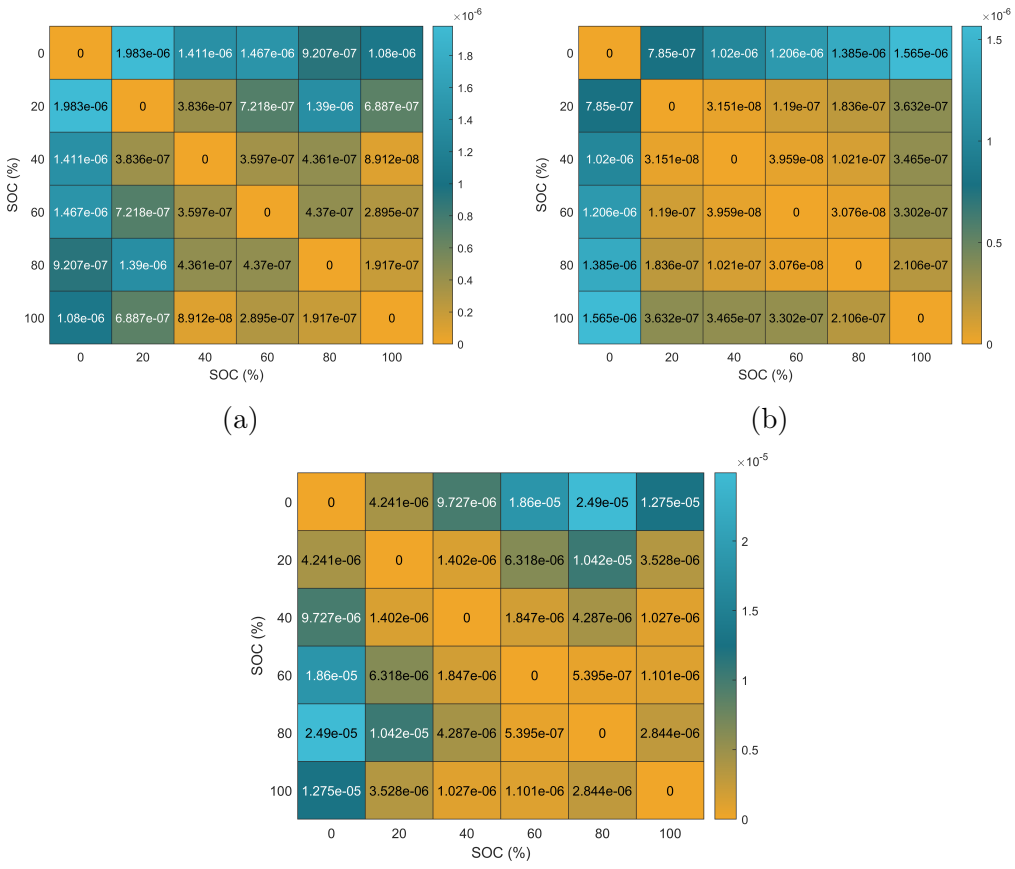

Figure A.1: The mean square error (MSE) for all SOCs for a) Cell 1, b) Cell 2, and c) Cell 3.

References

[1] M.S. Silberberg, P. Amateis, R. Venkateswaran, and L. Chen. *Chemistry: The molecular nature of matter and change*. McGraw-Hill, 2006.

[2] Bu-204: How do lithium batteries work? `https://batteryuniversity.com/article/bu-204-how-do-lithium-batteries-work`. Accessed: 2025-06-20.

[3] B. Nykvist and M. Nilsson. Rapidly falling costs of battery packs for electric vehicles. *Nature Climate Change*, 5, 2015.

[4] Y. Ding, Z. P. Cano, A. Yu, J. Lu, and Z. Chen. Automotive li-ion batteries: Current status and future perspectives. *Nature Climate Electrochemical Energy Reviews*, 2, 2019.

[5] T. A. Faunce, J. Prest, D. Su, S.J. Hearne, and F. Iacopi. On-grid batteries for large-scale energy storage: Challenges and opportunities for policy and technology. *MRS Energy and Sustainability*, 5(10), 2018.

[6] J. B. Robinson, M. Pham, M. D. R. Kok, T. M. M. Heenan, D. J. L. Brett, and P. R. Shearing. Examining the cycling behaviour of li-ion batteries using ultrasonic time-of-flight measurements. *Journal of Power Sources*, 444, 2019.

[7] R.J. Copley, D. Cumming, Y. Wu, and R.S. Dwyer-Joyce. Measurements and modelling of the response of an ultrasonic pulse to a lithium-ion battery as a precursor for state of charge estimation. *Journal of Energy Storage*, 36, 2021.

[8] J. Wen, Y. Yu, and C. Chen. A review on lithium-ion batteries safety issues: Existing problems and possible solutions. *Materials Express*, 2(3), 2012.

[9] Lithium-ion battery market size, share & trends analysis report by product (lco, lfp, nca, lmo, lto, nmc), by application (consumer electronics, energy storage systems, industrial), by region, and segment forecasts, 2022 - 2030. Accessed: 2023-02-02.

[10] Global electric vehicle outlook 2022. Accessed: 2023-02-02.

[11] Jaguar land rover-owner to spend £4bn on uk battery factory. Accessed: 2023-07-21.

[12] Eckard Helmers and Patrick Marx. Electric cars: technical characteristics and environmental impacts. *Environmental Sciences Europe*, 24, 2012.

[13] D.E. Schraufnagel, J.R. Balmes, C.T. Cowl, S.D. Matteis, S.H. Jung, K. Mortimer, R. Perez-Padilla, M.B. Rice, H. Riojas-Rodriguez, A. Sood, G.D. Thurston, T. To, A. Vanker, and D.J. Wuebbles. A review by the forum of international respiratory societies' environmental committee, part 1: The damaging effects of air pollution. *Chest*, 155, 2019.

[14] All-electric vehicles. Accessed: 2023-04-17.

[15] Yuqing Chen, Yuqiong Kang, Yun Zhao, Li Wang, Jilei Liu, Yanxi Li, Zheng Liang, Xiangming He, Xing Li, Naser Tavajohi, and Baohua Li. A review of lithium-ion battery safety concerns: The issues, strategies, and testing standards. *Journal of Energy Chemistry*, 59:83–99, 2021.

[16] Quanqing Zhao, Zefeng Guo, Yu Wu, Liqin Wang, Zhanli Han, Xilan Ma, Youqi Zhu, and Chuanbao Cao. Hierarchical flower-like spinel manganese-based oxide nanosheets for high-performance lithium ion battery. *Sci China Mater*, 62(10):1385–92, 2019.

[17] Lubing Wang, Sha Yin, Zhexun Yu, Yonggang Wang, TX Yu, Jing Zhao, Zhengchao Xie, Yangxing Li, and Jun Xu. Unlocking the significant role of shell material for lithium-ion battery safety. *Materials & Design*, 160:601–610, 2018.

[18] C.Y. Jhu, Y.W. Wang, C.Y. Wen, and C.M. Shu. Thermal runaway potential of $LiCoO_2$ and $Li(Ni_{1/3}Co_{1/3}Mn_{1/3})O_2$ batteries determined with adiabatic calorimetry methodology. *Applied Energy*, 100, 2012.

[19] K. Qian, Y. Li, Y.B. He, D. Liu, Y. Zheng, D. Luo, B. Li, and F. Kang. Abuse tolerance behavior of layered oxide-based li-ion battery during overcharge and over-discharge. *RSC Advances*, 80, 2016.

[20] T. Yokoshima, D. Mukoyama, F. Maeda, T. Osaka, Takazawa K, S. Egusa, S. Naoi, S. Ishikura, and K. Yamamoto. Direct observation of internal state of thermal runaway in lithium ion battery during nail-penetration test. *Journal of Power Sources*, 393, 2018.

[21] TechRadar. A new windows 11 bug has somehow charged a laptop battery to over 104Accessed: 2025-06-26.

[22] UmaTech. Fix wrong battery percentage in windows laptop, 2024. Accessed: 2025-06-26.

[23] PocketNow. Why is my battery estimate never accurate?, 2023. Accessed: 2025-06-26.

[24] Microsoft. How to fix the wrong estimate time on battery life using windows 10?, 2016. Accessed: 2025-06-26.

[25] HowToGeek. Why is my battery estimate never accurate?, 2016. Accessed: 2025-06-26.

[26] K. Liu, K. Li, Q. Peng, and C. Zhang. A brief review on key technologies in the battery management system of electric vehicles. *Front. Mech. Eng*, 14, 2019.

[27] Alice, the first all-electric passenger airplane, takes flight. Accessed: 2023-04-17.

[28] Alice, the world's first all-electric passenger jet, just aced her maiden flight. Accessed: 2023-07-21.

[29] C.M. Scala, R.J. Ditchburn, and S.K. Burke. Ndt of welds. In K.H. Jürgen Buschow, Robert W. Cahn, Merton C. Flemings, Bernhard Ilschner, Edward J. Kramer, Subhash Mahajan, and Patrick Veyssière, editors, *Encyclopedia of Materials: Science and Technology*, pages 5989–5991. Elsevier, Oxford, 2001.

[30] Juanjuan Zhu, Xiangwei Li, Scott Beamish, and Rob S Dwyer-Joyce. An ultrasonic method for measurement of oil films in reciprocating rubber o-ring seals. *Tribology International*, 167:107407, 2022.

[31] D.G. Aggelis, E. Leonidou, and T.E. Matikas. Subsurface crack determination by one-sided ultrasonic measurements. *Cement and Concrete Composites*, 34(2):140–146, 2012.

[32] L. Lu, X. Han, J. Li, J. Hua, and M. Ouyang. A review on the key issues for lithium-ion battery management in electric vehicles. *Journal of Power Sources*, 226, 2013.

[33] C. A. Zamai, D. Bavoso, A. A. Rodrigues, and J. A. S. Barbosa. *SISTEMA DE GESTIóN DE CARGA PARA BATERíAS DE ION-LITIO*. PhD thesis, Pontifical Javeriana University, 2018.

[34] X.P.Gao and H.X. Yang. Multi-electron reaction materials for high energy density batteries. *Energy and Environmental Science*, 3, 2009.

[35] Robert Schröder, Muhammed Aydemir, and Günther Seliger. Comparatively assessing different shapes of lithium-ion battery cells. *Procedia Manufacturing*, 8:104–111, 2017.

[36] K. Edström, M. Herstedt, and D. P. Abraham. A new look at the solid electrolyte interphase on graphite anodes in li-ion batteries. *Journal of Power Sources*, 153(2), 2006.

[37] R. Spotnitz and J. Franklin. Abuse behavior of high-power, lithium-ion cells. *Journal of Power Sources*, 113(1), 2003.

[38] M. A. Hannan, M. S. H. Lipu, A. Hussain, and A. Mohamed. A review of lithium-ion battery state of charge estimation and management system in electric vehicle applications: Challenges and recommendations. *Renewable and Sustainable Energy Reviews*, 78, 2017.

[39] J.P. Rivera-Barrera, N. Muñoz-Galeano, and H.O. Sarmiento-Maldonado. Soc estimation for lithium-ion batteries: Review and future challenges. *Electronics*, 102(6), 2017.

[40] J. Duan, X. Tang, H. Dai, Y. Yang, W. Wu, X. Wei, and Y. Huang. Building safe lithium-ion batteries for electric vehicles. *Electrochemical Energy Reviews*, 3, 2019.

[41] Guannan Qian, Federico Monaco, Dechao Meng, Sang-Jun Lee, Guibin Zan, Jizhou Li, Dmitry Karpov, Sheraz Gul, David Vine, Benjamin Stripe, et al. The role of structural defects in commercial lithium-ion batteries. *Cell Reports Physical Science*, 2(9), 2021.

[42] X. Feng, D. Ren, X. He, and M. Ouyang. Mitigating thermal runaway of lithium-ion batteries. *Joule*, 4, 2020.

[43] V. Pop, H. J. Bergveld, P H L Notten, and P. P. L. Regtien. State-of-the-art of battery state-of-charge determination. *Measurement Science and Technology*, 16, 2005.

[44] Peipei Xu, Junqiu Li, Nuo Lei, Feikun Zhou, and Chao Sun. An experimental study on the mechanical characteristics of li-ion battery during overcharge-induced thermal runaway. *International journal of energy research*, 45(14):19985–20000, 2021.

[45] Liya Guo, Daisy B Thornton, Mohamed A Koronfel, Ifan EL Stephens, and Mary P Ryan. Degradation in lithium ion battery current collectors. *Journal of Physics: Energy*, 3(3):032015, 2021.

[46] T. Langner, T. Sieber, and J. Acker. Studies on the deposition of copper in lithium-ion batteries during the deep discharge process. *Scientific Reports*, 11(6316), 2021.

[47] C. Fear, D. Juarez-Robles, J.A. Jeevarajan, and P.P. Mukherjee. Elucidating copper dissolution phenomenon in li-ion cells under overdischarge extremes. *Journal of the Electrochemical Society*, 165, 2018.

[48] K. W. E. Cheng, B. P. Divakar, H. Wu, K. Ding, and H. F. Ho. Battery-management system (bms) and soc development for electrical vehicles. *IEEE Transactions on Vehicular Technology*, 60, 2015.

[49] D.N.T. How, M.A. Hannan, M.S.H. Lipu, and P.J. Ker. State of charge estimation for lithium-ion batteries using model-based and data-driven methods: A review. *IEEE Access*, 7, 2019.

[50] Thanh-Son Dao, Chandrika P Vyasarayani, and John McPhee. Simplification and order reduction of lithium-ion battery model based on porous-electrode theory. *Journal of Power Sources*, 198:329–337, 2012.

[51] M. Berecibar, I. Gandiaga, I. Villarereal, N. Omar, J. Van Mierlo, and P. Van den Bossche. Critical review of state of health estimation methods of li-ion batteries for real applications. *Renewable and Sustainable Energy Reviews*, 56, 2016.

[52] Jinhao Meng, Mattia Ricco, Guangzhao Luo, Maciej Swierczynski, Daniel-Ioan Stroe, Ana-Irina Stroe, and Remus Teodorescu. An overview and comparison of online implementable soc estimation methods for lithium-ion battery. *IEEE Transactions on Industry Applications*, 54, 2017.

[53] Wladislaw Waag, Christian Fleischer, and Dirk Uwe Sauer. Critical review of the methods for monitoring of lithium-ion batteries in electric and hybrid vehicles. *Journal of Power Sources*, 258, 2014.

[54] K.S. Ng, C.S. Moo, Y.P Chen, and Y.C. Hsieh. Enhanced coulomb counting method for estimating state-of-charge and state-of-health of lithium-ion batteries. *Applied Energy*, 86, 2009.

[55] Y. Xing, W. He, M. Pecht, and K.L. Tsui. State of charge estimation of lithium-ion batteries using the open-circuit voltage at various ambient temperatures. *Applied Energy*, 113, 2014.

[56] L. Ungurean, G Cârstoiu, M.V. Micea, and V. Groza. Battery state of health estimation: a structured review of models, methods and commercial devices. *Internaltional Journal of Energy Research*, 41, 2017.

[57] D. Andre, C. Appel, T. Soczka-Guth, and D.W. Sauer. Advanced mathematical methods of soc and soh estimation for lithium-ion batteries. *Journal of Power Sources*, 224, 2013.

[58] Y. Xing, E.W.M. Ma, K.L Tsui, and M. Pecht. An ensemble model for predicting the remaining useful performance of lithium-ion batteries. *Microelectronics Reliability*, 53, 2013.

[59] D. Liu, J. Pang, J. Zhou, Y. Peng, and M. Pecht. Prognostics for state of health estimation of lithium-ion batteries based on combination gaussian process functional regression. *Microelectronics Reliability*, 4, 2013.

[60] J. Jiang and C. Zhang. *Fundamentals and Applications of Lithium-ion Batteries in Electric Drive Vehicles*. John Wiley & Sons Singapore Pte Ltd, 1 edition, 2017.

[61] J. Kräutkramer and H. Kräutkramer. *Ultrasonic Testing of Materials*. Springer, 3 edition, 2013.

[62] K Nowacki and W Kasprzyk. The sound velocity in an alloy steel at high-temperature conditions. *International Journal of Thermophysics*, 31(1):103–112, 2010.

[63] L Leibowitz and RA Blomquist. Thermal conductivity and thermal expansion of stainless steels d9 and ht9. *International journal of thermophysics*, 9(5):873–883, 1988.

[64] C-W Lin and JPM Trusler. The speed of sound and derived thermodynamic properties of pure water at temperatures between (253 and 473) k and at pressures up to 400 mpa. *The Journal of chemical physics*, 136(9), 2012.

[65] Alireza Bahadori and Hari B Vuthaluru. Prediction of bulk modulus and volumetric expansion coefficient of water for leak tightness test of pipelines. *International Journal of Pressure Vessels and Piping*, 86(8):550–554, 2009.

[66] Christian Vogt, Karim Laihem, and Christopher Wiebusch. Speed of sound in bubble-free ice. *The Journal of the Acoustical Society of America*, 124(6):3613–3618, 2008.

[67] John J Neumeier. Elastic constants, bulk modulus, and compressibility of h2o ice ih for the temperature range 50 k–273 k. *Journal of Physical and Chemical Reference Data*, 47(3), 2018.

[68] Huimin Han, Li Wei, Nizar Faisal Alkayem, and Maosen Cao. Embedded ultrasonic inspection on the mechanical properties of cold region ice under varying temperatures. *Sensors*, 23(13):6045, 2023.

[69] Henri Bader. Density of ice as a function of temperature and stress. Technical report, Cold Regions Research and Engineering Laboratory (US), 1964.

[70] S.W. Flax, N.J. Pelc, G.H. Glover, F.D Gutmann, and M. Mclachlan. Spectral characterization and attenuation measurements in ultrasound. *Ultrasonic Imaging*, 5, 1983.

[71] Seong-Hyun Park, Sungho Choi, Dong-Gi Song, and Kyung-Young Jhang. Microstructural characterization of additively manufactured metal components using linear and nonlinear ultrasonic techniques. *Materials*, 15, 2022.

[72] H. Brunskill. *The Real-Time Characterisation of Dry Machine Element Contacts Using Ultrasonic Reflectometry*. PhD thesis, University of Sheffield, 2013.

[73] P. Vigoureux. *Ultrasonics*. Chapman and Hall Ltd., 1950.

[74] H. G. Tattersall. The ultrasonic pulse-echo technique as applied to adhesion testing. *Journal of Physics D: Applied Physics*, 819(6), 1973.

[75] Steven L. Garrett. *Reflection, Transmission, and Refraction*, pages 513–542. Springer International Publishing, Cham, 2020.

[76] Jack Blitz and Walter G Mayer. Fundamentals of ultrasonics, 1964.

[77] D. Ensminger and L. J. Bond. *Ultrasonics: Fundamentals, Technologies, and Applications*. CRC Press, 2011.

[78] M. Barksi, P. Kedziora, A. Muc, and P. Romanowicz. Structural health monitoring (SHM) methods in machine design and operation. *Archive of Mechanical Engineering*, 61, 2014.

[79] Y. Fang, L. Lin, H. Feng, Z. Lu, and G.W. Emms. Review of the use of air-coupled ultrasonic technologies for nondestructive testing of wood and wood products. *Computers and Electronics in Agriculture*, 137, 2017.

[80] J.J. Chang, X.F. Zeng, and T.L. Wan. Real-time measurements of lithium-ion batteries state-of-charge based on air-coupled ultrasound. *AIP Advnaces*, 9, 2019.

[81] B. Sood, M. Osterman, and M. Pecht. Health monitoring of lithium-ion batteries. In *2013 IEEE Symposium on Product Compliance Engineering (ISPCE)*. IEEE, 2013.

[82] A. G. Hsieh, S. Bhadra, B. J. Hertzberg, P. J. Gjeltema, A. Goy, J. W. Fleischer, and D. A. Steingart. Electrochemical-acoustic time of flight: in operando correlation of physical dynamics with battery charge and health. *Energy & Environmental Science*, 8(5), 2015.

[83] L. Gold, T. Bach, W. Virsik, A. Schmitt, J. Müller, T.E.M Staab, and G. Sextl. Probing lithium-ion batteries' state-of-charge using ultrasonic transmission – concept and laboratory testing. *Journal of Power Sources*, 343, 2017.

[84] Y.S. Zhang, A.N.O. Radhakrishnan, J.B. Robinson, R. E. Owen, T.G. Tranter, E. Kendrick, P.R. Shearing, and D.J.L. Brett. In situ ultrasound acoustic measurement of the lithium-ion battery electrode drying process. *Applied Materials & Interfaces*, 13, 2021.

[85] H. Popp, M. Koller, M. Jahn, and A. Bergmann. Mechanical methods for state determination of lithium-ion secondary batteries: A review. *Journal of Energy Storage*, 32, 2020.

[86] J.M.Thijssen, G. Weijers, and C.L. de Korte. Objective performance testing and quality assurance of medical ultrasound equipment. *Ultrasound in Medicine & Biology*, 33, 2007.

[87] Fan Yang, Qian Mao, Jiaming Zhang, Shilin Hou, Guocui Bao, Ka wai Eric Cheng, Jiyan Dai, and Kwok-Ho Lam. Real-time state-of-charge estimation for rechargeable batteries based on in-situ ultrasound-based battery health monitoring and extended kalman filtering model. *Applied Energy*, 381, 2025.

[88] E. Cabrera-Castillo, F. Niedermeier, and A. Jossen. Calculation of the state of safety (SOS) for lithium ion batteries. *Journal of Power Sources*, 324, 2016.

[89] R. Fu, M. Xiao, and S. Choe. Modeling, validation and analysis of mechanical stress generation and dimension changes of a pouch type high power li-ion battery. *Journal of Power Sources*, 224, 2013.

[90] H. Popp, M. Koller, S. Keller, G. Glanz, R. Klambauer, and A. Bergmann. State estimation approach of lithium-ion batteries by simplified ultrasonic time-of-flight measurement. *IEEE Access*, 7, 2019.

[91] F. Grimsmann, F. Brauchle, T. Gerbert, A. Gruhle, M. Knipper, and J. Parisi. Hysteresis and current dependence of the thickness change of lithium-ion cells with graphite anode. *Journal of Energy Storage*, 12, 2017.

[92] P. Ladpli, F. Kopsaftopoulus, and F.K. Chang. Estimating state of charge and health of lithium-ion batteries with guided waves using built-in piezoelectric sensors/actuators. *Journal of Power Sources*, 2018.

[93] Y. Fan, S. Dixon, R.S. Edwards, and X. Jian. Ultrasonic surface wave propagation and interaction with surface defects on rail track head. *NDT and E International*, 40, 2007.

[94] G. Davies, K.W. Knehr, B. van Tassell, T. Hodson, S. Biswas, A.G. Hsieh, and D.A. Steingart. State of charge and state of health estimation using electrochemical acoustic time of flight analysis. *Journal of The Electrochemical Society*, 164(12), 2017.

[95] P. Ladpli, R. Nardari, F. Kopsaftopoulus, Y. Wang, and F.K. Chang. Design of multifunctional structural batteries with health monitoring capabilities. *European Workshop on Structural Health Monitoring*, 2016.

[96] Y. Wu, Y. Wang, W.K.C. Yung, and M. Pecht. Ultrasonic health monitoring of lithium-ion batteries. *Electronics*, 8(7), 2019.

[97] L. Oca, N. Guillet, R. Tessard, and U. Iraola. Lithium-ion capacitor safety assessment under electrical abuse tests based on ultrasound characterization and cell opening. *Journal of Energy Storage*, 23, 2019.

[98] C. Bommier, W. Chang, J. Li, S. Biswas, G. Davies, J. Nanda, and D. Steingart. Operando acoustic monitoring of SEI formation and long-term cycling in NMC/SiGr composite pouch cells. *Journal of The Electrochemical Society*, 167(2), 2020.

[99] J. B. Robinson, M. Maier, G. Alster, T. Compton, D.J.L. Brett, and P.R. Shearing. Spatially resolved ultrasound diagnostics of li-ion battery electrodes. *Physical Chemistry Chemical Physics*, 21(12), 2019.

[100] J.B. Robinson, R.E. Owen, M.D.R. Kok, M. Maier, J. Majasan, M. Braglia, R. Stocker, T. Amietszajew, A.J. Roberts, R. Bhagat, D. Billsson, J.Z. Olson, J. Park, G. Hinds, A.A. Tidblad, D.J.L. Brett, and P.R. Shearing. Identifying

defects in li-ion cells using ultrasound acoustic measurements. *Journal of The Electrochemical Society*, 167(12), 2020.

[101] L. Kong, C. Li, J. Jiang, and M.G. Pecht. Li-Ion Battery Fire Hazards and Safety Strategies. *Energies*, 11(9), 2018.

[102] X. Feng, M. Ouyang, X. Liu, L. Lu, Y. Xia, and X. He. Thermal runaway mechanism of lithium ion battery for electric vehicles: A review. *Energy Storage Materials*, 10, 2018.

[103] X. Feng, M. Fang, X. He, M. Ouyang, L. Lu, H. Wang, and M. Zhang. Thermal runaway features of large format prismatic lithium ion battery using extended volume accelerating rate calorimetry. *Journal of Power Sources*, 255, 2014.

[104] A.W. Golubkov, D. Fuchs, J. Wagner, H. Wiltsche, C. Stangl, G. Fauler, G. Voitic, A. Thaler, and V. Hacker. Thermal-runaway experiments on consumer li-ion batteries with metal-oxide and olivin-type cathodes. *RSC Adv.*, 4, 2014.

[105] Q.S. Wang, J.H. Sun, X.I. Yao, and C.H. Chen. Thermal behavior of lithiated graphite with electrolyte in lithium-ion batteries. *Journal of the Electrochemical Society*, 153, 2006.

[106] D.P. Abraham, E.P Roth, R. Kostecki, K. McCarthy, S. MacLaren, and D.H. Doughty. Diagnostic examination of thermally abused high-power lithium-ion cells. *Journal of Power Sources*, 161, 2006.

[107] D.P. Finegan, M. Scheel, J.B. Robinson, B. Tjaden, M. Di Michiel, G. Hinds, D. J. L. Brett, and P. R. Shearing. Investigating lithium-ion battery materials during overcharge-induced thermal runaway: an operando and multi-scale x-ray CT study. *Physical Chemistry Chemical Physics*, 18(45), 2016.

[108] D.P. Finegan, M. Scheel, J.B. Robinson, B. Tjaden, I. Hunt, T.J. Mason, J. Millichamp, M. Di Michiel, G.J. Offer, G. Hinds, D.J.L. Brett, and P.R. Shearing. In-operando high-speed tomography of lithium-ion batteries during thermal runaway. *Nature Communications*, 6(1), 2015.

[109] G.H. Kim, A Pesaran, and R. Spotnitz. A three-dimensional thermal abuse model for lithium-ion cells. *Journal of Power Sources*, 170, 2007.

[110] D.D. Macneil and J.R. Dahn. Test of reaction kinetics using both differential scanning and accelerating rate calorimetries as applied to the reaction of lixcoo2 in non-aqueous electrolyte. *Journal of Physical Chemistry A*, 105, 2001.

[111] G. Chen and T.J. Richardson. Thermal instability of olivine-type limnpo4 cathodes. *Journal of Power Sources*, 195, 2010.

[112] A. Kvasha, C. Gutiérrez, U. Osa, I. de Meatza, J.A. Blazquez, H. Macicior, and I. Urdampilleta. A comparative study of thermal runaway of commercial lithium ion cells. *Energy*, 159, 2018.

[113] Q. Wang, J. Sun, X. Yao, and C. Chen. Thermal stability of lipf$_6$/ec + dec electrolyte with charged electrodes for lithium ion batteries. *Thermochimica Acta*, 437(1), 2005.

[114] S. Liang, W. Yan, X. Wu, Y. Zhang, Y. Zhu, H. Wang, and Y. Wu. Gel polymer electrolytes for lithium ion batteries: Fabrication, characterization and performance. *Solid State Ionics*, 318, 2018.

[115] E. P. Roth and D. H. Doughty. Thermal abuse performance of high-power 18650 Li-ion cells. *Journal of Power Sources*, 128(2), 2004.

[116] M. N. Richard and J. R. Dahn. Accelerating Rate Calorimetry Study on the Thermal Stability of Lithium Intercalated Graphite in Electrolyte. II. Modeling the Results and Predicting Differential Scanning Calorimeter Curves. *Journal of The Electrochemical Society*, 146(6), 1999.

[117] D. D. MacNeil, L. Christensen, J. Landucci, J. M. Paulsen, and J. R. Dahn. An Autocatalytic Mechanism for the Reaction of Li_xCoO_2 in Electrolyte at Elevated Temperature. *Journal of The Electrochemical Society*, 147(3), 2000.

[118] I. Belharouak, Y.-K. Sun, W. Lu, and K. Amine. On the safety of the $Li_4Ti_5O_{12}$/$LiMn_2O_4$ lithium-ion battery system. *Journal of The Electrochemical Society*, 154, 2007.

[119] P.J. Bugryniec, J.N. Davidson, D.J. Cumming, and S.F. Brown. Pursuing safer batteries: Thermal abuse of LiFePO4 cells. *Journal of Power Sources*, 414, 2019.

[120] R. Korthauer. *Handbuch Lithium-Ionen-Batterien*. Springer, 1 edition, 2013.

[121] H. Zappen, G. Fuchs, A. Gitis, and D. Sauer. In-operando impedance spectroscopy and ultrasonic measurements during high-temperature abuse experiments on lithium-ion batteries. *Batteries*, 6(2), 2020.

[122] T. Waldmann, M. Wilka, M. Kasper, M. Fleischhammer, and M Wohlfahrt. Temperature dependent ageing mechanisms in lithium-ion batteries -a post mortem study. *Journal of Power Sources*, 262, 2014.

[123] Q. Wang, J. Sun, X. Chen, G. Chu, and C. Chen. Effects of solvents and salt on the thermal stability of charged licoo$_2$. *Materials Research Bulletin*, 44, 2009.

[124] D.D. MacNeil, Z. Lu, Z. Chen, and J.R. Dahn. A comparison of the electrode/electrolyte reaction at elevated temperatures for various li-ion battery cathodes. *Journal of Power Sources*, 108, 2002.

[125] O.S. Mendoza-Hernandez, H. Ishikawa, Y. Nishikawa, Y. Maruyama, and M. Umeda. Cathode material comparison of thermal runaway behavior of li-ion cells at different state of charges including over charge. *Journal of Power Sources*, 280, 2015.

[126] P. Peng and F. Jiang. Thermal safety of lithium-ion batteries with various cathode materials: A numerical study. *International Journal of Heat and Mass Transfer*, 103, 2016.

[127] P. Biensan, B. Simon, J. Peres, A. de Guibert, M. Broussely, J.M Bodet, and F. Perton. On safety of lithium-ion batteries. *Journal of Power Sources*, 81-82, 1999.

[128] Y. Wang, J. Jiang, and J.R. Dahn. The reactivity of delithiated $Li(Ni_1/3Co_{1/3}Mn_{1/3})O_2$, $Li(Ni_{0.8}Co_{0.15}Al_{0.05})O_2$ or $LiCoO_2$ with non-aqueous electrolyte. *Electrochemistry Communications*, 9, 2007.

[129] Y. Huang, Y.C. Lin, D.M. Jenkins, N.A. Chernova, Y. Chung, B. Radhakrishnan, I.H. Chu, J. Fang, Q. Wang, F. Omenya, S.P Ong, and M.S. Whittingham. Thermal stability and reactivity of cathode materials for li-ion batteries. *Applied Materials and Interfaces*, 8, 2016.

[130] Z. Zhang, D. Fouchard, and J. Rea. Differential scanning calorimetry material studies: implications for the safety of lithium-ion cells. *Journal of Power Sources*, 70, 1998.

[131] Q. Wang, J. Sun, and C. Chen. Thermal stability of delithiated $LiMn_2O_4$ with electrolyte for lithium-ion batteries. *Journal of the Electrochemical Society*, 154, 2007.

[132] S.K. Martha, O. Haik, E. Zinigrad, I. Exnar, T. Drezen, J.H. Miners, and D. Aurbach. On the thermal stability of olivine cathode materials for lithium-ion batteries. *Journal of the Electrochemical Society*, 158, 2011.

[133] H. Joachin, T.D. Kaun, K. Zaghib, and J. Prakash. Electrochemical and thermal studies of carbon-coated $LiFePO_4$ cathode. *Journal of the Electrochemical Society*, 156, 2009.

[134] J. Gong, Q. Wang, and J. Sun. Thermal analysis of nickel cobalt lithium manganese with varying nickel content used for lithium ion batteries. *Thermochimica Acta*, 655, 2017.

[135] Q. Wang, B. Mao, S.I. Stoliarov, and J. Sun. A review of lithium ion battery failure mechanisms and fire prevention strategies. *Progress in Energy and Combustion Science*, 73, 2019.

[136] T.Y. Lu, C.C. Chang, S.H. Wu, K.C. Chen, S.J. Lin, C.Y. Wen, and C.M. Shu. Thermal hazard evaluations of 18650 lithium-ion batteries by an adiabatic calorimeter. *Journal of thermal analysis and calorimetry*, 114(3), 2013.

[137] S.K. Martha, B. Markovsky, J. Grinblat, Y. Cofer, O. Haik, E. Zinigrad anjd D. Aurbach, T. Drezen, D. Wang, F. Deghenghi, and I. Exnar. $LiMnPO_4$ and $LiMn_{0.8}Fe_{0.2}PO_4$ as advanced cathode materials for rechargeable lithium-ion batteries. *Journal of the Electrochemical Society*, 2010.

[138] C.Y. Lee, S.J Lee, M.S. Tang, and P.C. Chen. In situ monitoring of temperature inside lithium-ion batteries by flexible micro temperature sensors. *Sensors*, 11, 2011.

[139] X. Feng, J. Sun, M. Ouyang, F. Wang, X. He, L. Lu, and H. Peng. Characterization of penetration induced thermal runaway propagation process within a large format lithium ion battery module. *Journal of Power Sources*, 275, 2015.

[140] B. Liu, S. Yin, and J. Xu. Integrated computation model of lithium-ion battery subject to nail penetration. *Applied Energy*, 183, 2016.

[141] B. Liu, F. Wang, B. Fan, Z. Zhang, and F. Pei. Influence of penetration speeds on power li-ion-cell's safety performance. *Journal of Automotive Safety and Energy*, 4, 2013.

[142] H. Maleki and J.N. Howard. Internal short circuit in li-ion cells. *Journal of Power Sources*, 191, 2009.

[143] B. Mao, H. Chen, Z. Chi, T. Wu, and Q. Wang. Failure mechanism of the lithium ion battery during nail penetration. *International Journal of Heat and Mass Transfer*, 122, 2018.

[144] J. Liu, Q. Duan, W. Peng, L. Feng, M. Ma, S. Hu, J. Sun, and Q. Wang. Slight overcharging cycling failure of commercial lithium-ion battery induced by the jelly roll destruction. *Process Safety and Environmental Protection*, 160, 2022.

[145] H. Zheng, Q. Sun, G. Liu, X. Song, and V.S. Battaglia. Correlation between dissolution behavior and electrochemical cycling performance for $LiNi_{1/3}Co_{1/3}Mn_{1/3}O_2$-based cells. *Journal of Power Sources*, 207, 2012.

[146] N.K. Sharma and V.K. Peterson. Overcharging a lithium-ion battery: effect on the lixc6 negative electrode determined by in situ neutron diffraction. *Journal of Power Sources*, 244, 2013.

[147] D. Ren, X. Feng, L. Lu, M. Ouyang, S. Zheng, J. Li, and X. He. An electrochemical-thermal coupled overcharge-to-thermal-runaway model for lithium ion battery. *Journal of Power Sources*, 364, 2017.

[148] K. Kumai, H. Miyashiro, Y. Kobayashi, K. Takei, and R. Ishikawa. Gas generation mechanism due to electrolyte decomposition in commercial lithium-ion cell. *Journal of Power Sources*, 81, 1999.

[149] Y.B. He, F. Ning, Q.H. Yang, Q.S. Song, B. Li, F. Su, H. Du, Z.Y. Tang, and F. Kang. Structural and thermal stabilities of layered $Li(Ni_{1/3}Co_{1/3}Mn_{1/3})O_2$ materials in 18650 high power batteries. *Journal of Power Sources*, 196, 2011.

[150] Y. Saito, K. Takano, and A. Negishi. Thermal behaviors of lithium-ion cells during overcharge. *Journal of Power Sources*, 97, 2001.

[151] R.A. Leising, M.J. Palazzo, E.S. Takeuchi, and K.J. Takeuchi. Abuse testing of lithium-ion batteries: Characterization of the overcharge reaction of $LiCoO_2$/Graphite cells. *Journal of The Electrochemical Society*, 148, 2001.

[152] J. Weng, X. Yang, D. Ouyang, M. Chen, G. Zhang, and J. Wang. Comparative study on the transversal/lengthwise thermal failure propagation and heating position effect of lithium-ion batteries. *Applied Energy*, 255, 2019.

[153] G. Zhang, X. Wei, S. Chen, J. Zhu, G. Han, X. Tang, W. Hua, H. Dai, and J. Ye. Comprehensive investigation of a slight overcharge on degradation and thermal runaway behavior of lithium-ion batteries. *ACS Applied Materials and Interfaces*, 13, 2021.

[154] J. Liu, Q. Duan, L. Feng, M. Ma, J. Sun, and Q. Wang. Capacity fading and thermal stability of $LiNi_xCo_yMn_zO_2$/graphite battery after overcharging. *Journal of Energy Storage*, 29, 2020.

[155] T. Cai, S. Pannala, A.G. Stefanopoulou, and J.B. Siegel. Battery internal short detection methodology using cell swelling measurements. In *2020 American Control Conference (ACC)*, 2020.

[156] H.A. Gabber, A.M. Othman, and M.R. Abdussami. Review of battery management systems (bms) developmentand industrial standards. *Technoligies*, 9, 2021.

[157] N.E. Galushkin, N.N. Yazvinskaya, and D.N Glaushkin. Mechanism of gases generation during lithium-ion batteries cycling. *Journal of the Electrochemical Society*, 166, 2019.

[158] B. Rowden and N. Garcia-Araez. A review of gas evolution in lithium ion batteries. *Energy Reports*, 6(5), 2020.

[159] M. Metzger, B. Strehle, S. Solchenbach, and H.A. Gasteiger. Origin of H_2 Evolution in LIBs: H_2O reduction vs. electrolyte oxidation. *Journal of the Electrochemical Society*, 162(5), 2016.

[160] R. jung, M. Metzger, F. Maglia, C. Stinner, and H.A. Gasteiger. Oxygen release and its effect on the cycling stability of $LiNi_xMn_yCo_zO_2$ (nmc) cathode materials for li-ion batteries. *Journal of the Electrochemical Society*, 164, 2016.

[161] R. bernhard, M. Metzger, and H.A. Gasteiger. Gas evolution at graphite anodes depending on electrolyte water content and sei quality studied by online electrochemical mass spectrometry. *Journal of the Electrochemical Society*, 162(10), 2015.

[162] D.P. Finegan, E. Darcy, M. Keyser, B. Tjaden, T.M.M. Heenan, R. Jervis, J.J. Bailey, N.T. Vo, O.V. Magdysyuk, M. Drakopoulos, M. Di Michiel, A. Rack, G. Hinds, D.J.L. Brett, and P.R. Shearing. Identifying the cause of rupture of li-ion batteries during thermal runaway. *Advanced Science*, 5(1), 2018.

[163] T. Cai, A.G. Stefanopoulou, and J.B. Siegel. Modeling li-ion battery temperature and expansion force during the early stages of thermal runaway triggered by internal shorts. *Journal of The Electrochemical Society*, 2019.

[164] L. Huang, Z. Zhang, Z. Wang, L. Zhang, X. Zhu, and D.D. Dorrell. Thermal runaway behavior during overcharge for large-format lithium-ion batteries with different packaging patterns. *Journal of Power Sources*, 25, 2019.

[165] M.T.M. Pham, J.J. Darst, D.P. Finegan, J.B. Robinson, T.M.M. Heenan, M.D.R. Kok, F. Iacoviello, R.Owen, W.Q. Walker, O.V. Magdysyuk, T. Connolley, E. Darcy, G. Hinds, D.J.L Brett, and P.R. Shearing. Correlative acoustic time-of-flight spectroscopy and x-ray imaging to investigate gas-induced delamination in lithium-ion pouch cells during thermal runaway. *Journal of Power Sources*, 470, 2020.

[166] J. Chen, D. Ren, H. Hsu, L. Wang, X. He, C. Zhang, X. Feng, and M. Ouyang. Investigating the thermal runaway features of lithium-ion batteries using a thermal resistance network model. *Applied Energy*, 295, 2021.

[167] T. Cai, A.G. Stefanopoulou, and J.B. Siegel. Early detection for li-ion batteries thermal runaway based on gas sensing. *ECS Transactions*, 2019.

[168] Z. Wei, J. Zhao, H. He, G. Ding, H. Cui, and L. Liu. Future smart battery and management: Advanced sensing from external to embedded multi-dimensional measurement. *Journal of Power Sources*, 489, 2021.

[169] S. Koch, K.P. Birke, and R. Kuhn. Fast thermal runaway detection for lithium-ion cells in large scale traction batteries. *Batteries*, 2018.

[170] J. Klink, A. Hebenbrock, J. Grabow, N. Orazov, U. Nylen, R. benger, and H.P. Beck. Comparison of model-based and sensor-based detection of thermal runaway in li-ion battery modules for automotive application. *Batteries*, 8, 2022.

[171] M.K. Tran, A. Mevawalla, A. Aziz, S. Panchal, Y. Xie, and M. Fowler. A review of lithium-ion battery thermal runaway modeling and diagnosis approaches. *Processes*, 2022.

[172] W. Chang, C. Bommier, T. Fair, J. Yeung, S. Patil, and D. Steingart. Understanding adverse effects of temperature shifts on li-ion batteries: An operando acoustic study. *Journal of the Electrochemical Society*, 2020.

[173] Ozren Jović, Dario Omanović, Marina Zelić, and Ivanka Pižeta. Center of gravity (cog) method as a tool in processing of voltammetric signals. *Electroanalysis*, 27(10):2347–2356, 2015.

[174] R.E. Owen, J.B. Robinson, J.S. Weaving, M.T.M. Pham, T.G. Tranter, T.P. Neville, D. Billson, M. Braglia, R. Stocker, A.A. Tidblad, P.R. Shearing, and D.J.L. Brett. Operando ultrasonic monitoring of lithium-ion battery temperature

and behaviour at different cycling rates and under drive cycle conditions. *Journal of The Electrochemical Society*, 2022.

[175] M.C. Appleberry, J.A. Kowalski, S.A. Africk, J. Mitchell, T.C. Ferree, V. Chang, V. Parekh, Z. Xu, Z. Ye, J.F. Whitacre, and S.D. Murphy. Avoiding thermal runaway in lithium-ion batteries using ultrasound detection of early failure mechanisms. *Journal of Power Sources*, 2022.

[176] R. Xiong, J. Cao, Q. Yu, H. He, and F. Sun. Critical review on the battery state of charge estimation methods for electric vehicles. *IEEE Access*, 6, 2018.

[177] K. Movassagh, A. Raihan, B. Balasignam, and K. Pattipati. A critical look at coulomb counting approach for state of charge estimation in batteries. *Energies*, 14(14), 2021.

[178] D. Williams, R. Copley, P. Bugryniec, R. Dwyer-Joyce, and S. Brown. A review of ultrasonic monitoring: Assessing current approaches to li-ion battery monitoring and their relevance to thermal runaway. *Journal of Power Sources*, 590, 2024.

[179] D. Williams, J. Green, P. Bugryniec, S. Brown, and R. Dwyer-Joyce. Battery age monitoring: Ultrasonic monitoring of ageing and degradation in lithium-ion batteries. *Journal of Power Sources*, 631, 2025.

[180] Daniel Williams, Robert Milton, Joshua Taylor, Robert Dwyer-Joyce, and Solomon Brown. Acoustic assessment of lithium-ion batteries: Unravelling temperature and charge contributions. *Journal of Power Sources*, 665, 2026.

[181] Lien-Yang Chou, Yusheng Ye, Hiang Kwee Lee, Wenxiao Huang, Rong Xu, Xin Gao, Renjie Chen, Feng Wu, Chia-Kuang Tsung, and Yi Cui. Electrolyte-resistant dual materials for the synergistic safety enhancement of lithium-ion batteries. *Nano letters*, 21(5):2074–2080, 2021.

[182] Zeyu Chen, Rui Xiong, Jinpeng Tian, Xiong Shang, and Jiahuan Lu. Model-based fault diagnosis approach on external short circuit of lithium-ion battery used in electric vehicles. *Applied Energy*, 184:365–374, 2016.

[183] Office for Product Safety and Standards. https://www.gov.uk/government/publications/personal-light-electric-vehicle-plev-battery-safety-research. Technical report, UK Government, 2025.

[184] Department for Business, Office for Product Safety Trade, Standards, and Energy Industrial Strategy Department for Business. Domestic battery energy storage systems. Technical report, UK Government, 2020.

[185] V. Ramadesigan, P.W.C. Northrop, S. De, S. Santhanagopalan, R.D. Braatz, and V.R. Subramanian. Modeling and simulation of lithium-ion batteries from a systems engineering perspective. *Journal of the Electrochemical Society*, 159, 2012.

[186] G.O. Sahinoglu, M. Pajovic, Z. Sahinoglu, Y. Wang, P.V. Orlik, and T. Wada. Battery state-of-charge estimation based on regular/recurrent gaussian process regression. *IEEE Transactions on Inducstrial Electronics*, 65, 2018.

[187] S. Wang, K. Rafiz, J. Liu, and J.Y.S. Lin. Effects of lithium dendrites on thermal runaway and gassing of lifepo$_4$ batteries. *Sustainable Energy and Fuels*, 4, 2020.

[188] G.L. Plett. Extended kalman filtering for battery management systems of lipb-based hev battery packs: Part 1. background. *Journal of Power Sources*, 134, 2004.

[189] I.S. Kim. A technique for estimating the state of health of lithium batteries through a dual-sliding-mode observer. *IEEE Transactions on Power Electronics*, 25, 2010.

[190] R. Xiong, L. Li, and J. Tian. Towards a smarter battery management system: A critical review on battery state of health monitoring methods. *Journal of Power Sources*, 405, 2018.

[191] G. Vennan, A. Sahoo, and S. Ahmed. A survey on lithium-ion battery internal and external degradation modeling and state of health estimation. *Journal of Energy Storage*, 52, 2022.

[192] Y.o Liu, C. Liu, Y. Liu, F. Sun, J. Qiao, and T. Xu. Review on degradation mechanism and health state estimation methods of lithium-ion batteries. *Journal of Traffic and Transportation Engineering (English Edition)*, 10, 2023.

[193] C. Weng, J. Sun, and H. Peng. A unified open-circuit-voltage model of lithium-ion batteries for state-of-charge estimation and state-of-health monitoring. *Journal of Power Sources*, 258, 2014.

[194] J. Remmlinger, M. Buchholz, T. Soczka-Guth, and K. Dietmayer. On-board state-of-health monitoring of lithium-ion batteries using linear parameter-varying models. *Journal of Power Sources*, 239, 2013.

[195] Feng Jiang, Yuqian Chen, Shaohua Ju, Qinyu Zhu, Libo Zhang, Jinhui Peng, Xuming Wang, and Jan D. Miller. Ultrasound-assisted leaching of cobalt and lithium from spent lithium-ion batteries. *Ultrasonics Sonochemistry*, 48, 2018.

[196] Chunhong Lei, Iain Aldous, Jennifer M. Hartley, Dana L. Thompson, Sean Scott, Rowan Hanson, Paul A. Anderson, Emma Kendrick, Rob Sommerville, Karl S. Ryder, and Andrew P. Abbott. Lithium ion battery recycling using high-intensity ultrasonication. *Green Chemistry*, 23, 2021.

[197] Sunghyun Jie, Joonhee Kang, Seunghun Baek, and Byeongyong Lee. Enhanced electrochemical performance of li-ion battery via ultrasonic-assisted inorganic-rich and thin sei layer. *Ultrasonics Sonochemistry*, 100, 2023.

[198] Voon-Kean Wong, Yue Hu, Zi Wen Tham, Yi Fan Chen, Menglong Liu, Kai En Lim, Sung Joon Park, Fangsen Cui, and Lei Zhang. Measurement of elastic constant matrix of carbon fiber composites with an ultrasonic 2d-array transducer. *IEEE Sensors Journal*, 22, 2022.

[199] Bo Sun, Chuang Zhang, Suzhen Liu, Zhicheng Xu, and Lianbing Li. Ultrasonic inspection of pouch-type lithium-ion batteries: a review. *Nondestructive Testing and Evaluation*, 2024.

[200] G. Zhao, Y. Liu, G. Liu, S. Jiang, and W. Hao. State-of-charge and state-of-health estimation for lithium-ion battery using the direct wave signals of guided wave. *Journal of Energy Storage*, 39, 2021.

[201] J.Y. Kim, J.H. Jo, and J.W. Byeon. Ultrasonic monitoring performance degradation of lithium ion battery. *Microelectronics Reliability*, 114, 200.

[202] T. Guan, S. Sun, F. Yu, Y. Gao, P. Fan, P. Zuo, C. Du, and G. Yin. The degradation of licoo2/graphite batteries at different rates. *Electrochimica Acta*, 279, 2018.

[203] R. Xiong, Y. Pan, W. Shen, H. Li, and F. Sun. Lithium-ion battery aging mechanisms and diagnosis method for automotive applications: Recent advances and perspectives. *Renewable and Sustainable Energy Reviews*, 131, 2020.

[204] T. Guan, S. Sun, Y. Gao, C. Du, P. Zuo, Y. Cui, L. Zhang, and G. Yin. The effect of elevated temperature on the accelerated aging of LiCoO $_2$/mesocarbon microbeads batteries. *Applied Energy*, 177, 2016.

[205] D. Wong, B. Shrestha, D.A. Wetz, and J.M. Heinzel. Impact of high rate discharge on the aging of lithium nickel cobalt aluminum oxide batteries. *Journal of Power Sources*, 280, 2015.

[206] Hongbin Sun, Nitin Muralidharan, Ruhul Amin, Vivek Rathod, Pradeep Ramuhalli, and Ilias Belharouak. Ultrasonic nondestructive diagnosis of lithium-ion batteries with multiple frequencies. *Journal of Power Sources*, 549, 2022.

[207] S.J. Drake, M. Martin, D.A. Wetz, J.K. Ostanek, S.P. Miller, J.M. Heinzel, and A. Jain. Heat generation rate measurement in a li-ion cell at large c-rates through temperature and heat flux measurements. *Journal of Power Sources*, 285, 2015.

[208] Lena Spitthoff, Paul R. Shearing, and Odne Stokke Burheim. Temperature, ageing and thermal management of lithium-ion batteries. *Energies*, 14(5), 2021.

[209] H. Amiri and B. Makkiabadi. A review of ultrasound thermometry techniques. *Frontiers in Biomedical Technologies*, 7, 2020.

[210] R.J. Copley and R.S. Dwyer-Joyce. Prediction of the internal structure of a lithium-ion battery using a single ultrasound wave response. *Journal of Energy Storage*, 72, 2023.

[211] S. Poll B. Saha, K. Goebel and J. Christophersen. Prognostics methods for battery health monitoring using a bayesian framework. *IEEE Transactions on Instrumentation and Measurement*, 58, 2009.

[212] B.E. Olivares and M.A. Cerda Muñoz. Particle-filtering-based prognosis framework for energy storage devices with a statistical characterization of state-of-health regeneration phenomena. *IEEE Transactions on Instrumentation and Measurement*, 62, 2013.

[213] Z. Chen, Q. Xue, R. Xiao, Y. Liu, and J. Shen. State of health estimation for lithium-ion batteries based on fusion of autoregressive moving average model and elman neural network. *IEEE Access*, 7, 2019.

[214] G. Liu, M. Ouyang, L. Lu, J. Li, and X. Han. Analysis of the heat generation of lithium-ion battery during charging and discharging considering different influencing factors. *Journal of Thermal Analysis and Calorimetry*, 116, 2014.

[215] L. Zhang, L. Wang, C. Lyu, J. Li, and J. Zheng. Non-destructive analysis of degradation mechanisms in cycle-aged Graphite/$LiCoO_2$ batteries. *Energies*, 7, 2014.

[216] F.A. Soto, A. Marzouk, F. El-Mellouhi, and P.B. Balbuena. Understanding ionic diffusion through sei components for lithium- ion and sodium-ion batteries: Insights from first-principles calculations. *Chemistry of Materials*, 30, 2018.

[217] L. Yao, S. Xu, A. Tang, F. Zhou, J. Hou, Y. Xiao, and Z. Fu. A review of lithium-ion battery state of health estimation and prediction methods. *World Electric Vehicle Journal*, 12, 2021.

[218] D.I. Stroe, M. Swierczynski, S.K. Kær, and R. Teodorescu. Degradation behavior of lithium-ion batteries during calendar ageing—the case of the internal resistance increase. *IEEE Transactions on Power Electronics*, 54, 2018.

[219] H. Sun, J. Sun, K. Zhao, L. Wang, and K. Wang. Data-driven ica-bi-lstm-combined lithium battery soh estimation. *Mathematical Problems in Engineering*, 2022, 2022.

[220] T.S. Pathan, M. Rashid, M. Walker, W.D. Widanage, and E. Kendrick. Active formation of li-ion batteries and its effect on cycle life. *Journal of Physics: Energy*, 1, 2019.

[221] T. Plattard, N. Barnel, L. Assaud, S. Franger, and J.M. Duffault. Combining a fatigue model and an incremental capacity analysis on a commercial nmc/graphite cell under constant current cycling with and without calendar aging. *Batteries*, 5, 2019.

[222] M. Dubarry and D. Anseán. Best practices for incremental capacity analysis. *Frontiers in Energy Research*, 10, 2022.

[223] I. Bloom, L.K. Walker, J.Basco, D.P. Abraham, J.P. Christophersen, and C.D. Ho. Differential voltage analyses of high-power lithium-ion cells. 4. cells containing nmc. *Journal of Power Sources*, 195, 2010.

[224] R. Carter, T.A. Kingston, R.W. Atkinson, M. Parmananda, M. Dubarry, C. Fear, P.P. Mukherjee, and C.T. Love. Directionality of thermal gradients in lithium-ion batteries dictates diverging degradation modes. *Cell Reports Physical Science*, 2, 2021.

[225] M. Kemeny, P. Ondrejka, and M. Mikolasek. Incremental capacity analysis for prediction of li-ion battery degradation mechanisms: Simulation study. In *The 13th International Conference on Advanced Semiconductor Devices And Microsystems,*, 2020.

[226] J. Wang, J. Purewal, P. Liu, J. Hicks-Garner, S. Soukazian, W. Sherman, A. Sorenson, L. Vu, H. Tataria, and M.W. Verbrugge. Degradation of lithium ion batteries employing graphite negatives and nickel-cobalt-manganese oxide þ spinel manganese oxide positives: Part 1, aging mechanisms and life estimation. *Journal of Power Sources*, 269, 2014.

[227] X. Han, M. Ouyang, L. Lu, J. Li, Y. Zheng, and Z. Li. A comparative study of commercial lithium ion battery cycle life in electrical vehicle: Aging mechanism identification. *Journal of Power Sources*, 251, 2014.

[228] R. Deshpande, M. Verbrugge, Y.T. Cheng, J. Wang, and P. Liu. Battery cycle life prediction with coupled chemical degradation and fatigue mechanics. *Journal of The Electrochemical Society*, 159, 2012.

[229] Kangpei Meng, Xiaoping Chen, Wen Zhang, Wesley Chang, and Jun Xu. A robust ultrasonic characterization methodology for lithium-ion batteries on frequency-domain damping analysis. *Journal of Power Sources*, 547, 2022.

[230] Shriram Santhanagopalan and Ralph E. White. Quantifying cell-to-cell variations in lithium ion batteries. *International Journal of Electrochemistry*, 2012(1), 2012.

[231] Jude O Majasan, James B Robinson, Rhodri E Owen, Maximilian Maier, Anand NP Radhakrishnan, Martin Pham, Thomas G Tranter, Yeshui Zhang, Paul R Shearing, and Dan JL Brett. Recent advances in acoustic diagnostics for electrochemical power systems. *Journal of Physics: Energy*, 3(3), 2021.

[232] Y. Preger, H.M. Barkholtz, A. Fresquez, D.L. Campbell, B.W. Juba, J. Romàn-Kustas, S.R. Ferreira, and B. Chalamala. Degradation of commercial lithium-ion cells as a function of chemistry and cycling conditions. *Journal of The Electrochemical Society*, 167, 2020.

[233] Y. Li, M. Bettge, B. Polzin, Y. Zhu, M. Balasubramanian, and D. P. Abraham. Understanding long-term cycling performance of $Li_{1.2}Ni_{0.15}Mn_{0.55}Co_{0.1}O_2$–Graphite lithium-ion cells. *Journal of The Electrochemical Society*, 160, 2013.

[234] J. Xu, B. Liu, and D. Hu. State of charge dependent mechanical integrity behavior of 18650 lithium-ion batteries. *Scientific Reports*, 6, 2016.

[235] Y. Qi, H.B. Guo, L.G. Hector, and A. Timmons. Threefold increase in the young's modulus of graphite negative electrode during lithium intercalation. *Journal of the Electrochemical Society*, 157, 2010.

[236] Xin Lai, Ming Yuan, Xiaopeng Tang, Yuejiu Zheng, Jiajun Zhu, Yuedong Sun, Yuanqiang Zhou, and Furong Gao. State-of-power estimation for lithium-ion batteries based on a frequency-dependent integer-order model. *Journal of Power Sources*, 594, 2024.

[237] Jiaxing Yang, Hengyun Zhang, Yidong Xu, and Peichao Li. Analysis of heat generation in lithium-ion battery components and voltage rebound based on electrochemical and thermal coupled model. *Journal of Energy Storage*, 72, 2023.

[238] Yuejiu Zheng, Hang Wu, Wei Yi, Xin Lai, Haifeng Dai, Xuebing Han, and Minggao Ouyang. A novel classification method of commercial lithium-ion battery cells based on fast and economic detection of self-discharge rate. *Journal of Power Sources*, 478:229039, 2020.

[239] World Resource Institute. World greenhouse gas emissions: 2020, 2023. [Accessed: 2024-06-18].

[240] D.H. Doughty and E.P Roth. A general discussion of li ion battery safety. *Applied Energy*, 2012.

[241] T.B. Reddy. *Linden's Handbook of Batteries*. McGraw-Hill Education, 2011.

[242] Jun Xu, Chunting Chris Mi, Binggang Cao, Junjun Deng, Zheng Chen, and Siqi Li. The state of charge estimation of lithium-ion batteries based on a proportional-integral observer. *IEEE Transactions on Vehicular Technology*, 63, 2014.

[243] Cyril Truchot, Matthieu Dubarry, and Bor Yann Liaw. State-of-charge estimation and uncertainty for lithium-ion battery strings. *Applied Energy*, 119, 2014.

[244] Abbas Fotouhi, Daniel J Auger, Karsten Propp, Stefano Longo, and Mark Wild. A review on electric vehicle battery modelling: From lithium-ion toward lithium–sulphur. *Renewable and Sustainable Energy Reviews*, 56:1008–1021, 2016.

[245] Weihan Li, Decheng Cao, Dominik Jöst, Florian Ringbeck, Matthias Kuipers, Fabian Frie, and Dirk Uwe Sauer. Parameter sensitivity analysis of electrochemical model-based battery management systems for lithium-ion batteries. *Applied Energy*, 269:115104, 2020.

[246] Alexander P Schmidt, Matthias Bitzer, Árpád W Imre, and Lino Guzzella. Experiment-driven electrochemical modeling and systematic parameterization for a lithium-ion battery cell. *Journal of Power Sources*, 195(15):5071–5080, 2010.

[247] Md Ashiqur Rahman, Sohel Anwar, and Afshin Izadian. Electrochemical model parameter identification of a lithium-ion battery using particle swarm optimization method. *Journal of Power Sources*, 307, 2016.

[248] Jonas Keil and Andreas Jossen. Electrochemical modeling of linear and nonlinear aging of lithium-ion cells. *Journal of The Electrochemical Society*, 167(11):110535, 2020.

[249] B. Sood, C. Hendricks, M. Osterman, and M. Pecht. Health monitoring of lithium-ion batteries. *EDFA Technical Articles*, 16, 2014.

[250] Kanji Ono. A comprehensive report on ultrasonic attenuation of engineering materials, including metals, ceramics, polymers, fiber-reinforced composites, wood, and rocks. *Applied Sciences*, 10, 2020.

[251] Santhakumar Sampath, Xuesong Yin, Zi Wen Tham, Yi Fan Chen, and Lei Zhang. Real-time and non-contact estimation of state of charge for lithium-ion battery using laser ultrasonics. *Journal of Power Sources*, 605:234544, 2024.

[252] Vivek B Shenoy, Priya Johari, and Yue Qi. Elastic softening of amorphous and crystalline li–si phases with increasing li concentration: a first-principles study. *Journal of Power Sources*, 195(19):6825–6830, 2010.

[253] Y. Qi, H. Guo, L.G. Hector, and A. Timmons. Threefold increase in the young's modulus of graphite negative electrode during lithium intercalation. *Journal of The Electrochemical Society*, 157, 2010.

[254] Stephen J Harris and Peng Lu. Effects of inhomogeneities – nanoscale to mesoscale – on the durability of li-ion batteries. *The Journal of Physical Chemistry C*, 117(13):6481–6492, 2013.

[255] Matthew T McDowell, Seok Woo Lee, William D Nix, and Yi Cui. 25th anniversary article: understanding the lithiation of silicon and other alloying anodes for lithium-ion batteries. *Advanced materials*, 25(36):4966–4985, 2013.

[256] Yukinori Koyama, Timothy E Chin, Urs Rhyner, Richard K Holman, Steven R Hall, and Y-M Chiang. Harnessing the actuation potential of solid-state intercalation compounds. *Advanced Functional Materials*, 16(4):492–498, 2006.

[257] Ming Huang, Niall Kirkaldy, Yan Zhao, Yatish Patel, Frederic Cegla, and Bo Lan. Quantitative characterisation of the layered structure within lithium-ion batteries using ultrasonic resonance. *Journal of Energy Storage*, 50:104585, 2022.

[258] R. Owen, W. Wiśniewska, M. Braglia, R. Stocker, P.R. Shearing, D.j.l. Brett, and J.B. Robinson. Operando ultrasonic monitoring of the internal temperature of lithium-ion batteries for the detection and prevention of thermal runaway. *Journal of The Electrochemical Society*, 171, 2010.

[259] Rymantas Kazys and Vaida Vaskeliene. High temperature ultrasonic transducers: A review. *Sensors*, 21, 2021.

[260] V Baran, O Dolotko, MJ Mühlbauer, A Senyshyn, and H Ehrenberg. Thermal structural behavior of electrodes in li-ion battery studied in operando. *Journal of The Electrochemical Society*, 165(9):A1975, 2018.

[261] Eunkang Lee, Shoaib Muhammad, Taewhan Kim, Hyunchul Kim, Wontae Lee, and Won-Sub Yoon. Tracking the influence of thermal expansion and oxygen vacancies on the thermal stability of ni-rich layered cathode materials. *Advanced Science*, 7(12):1902413, 2020.

[262] Hongbin Sun, Nitin Muralidharan, Ruhul Amin, Vivek Rathod, Pradeep Ramuhalli, and Ilias Belharouak. Ultrasonic nondestructive diagnosis of lithium-ion batteries with multiple frequencies. *Journal of Power Sources*, 549, 2022.

[263] Qingdi Ke, Shouzhi Jiang, Wanpeng Li, Wu Lin, Xinyu Li, and Haihong Huang. Potential of ultrasonic time-of-flight and amplitude as the measurement for state of charge and physical changings of lithium-ion batteries. *Journal of Power Sources*, 549:232031, 2022.

[264] Robert A. Milton. Reduced Order Modelling using Global Sensitivity Analysis and Gaussian Process Regression, 11 2017.

[265] H. N. G. Wadley, S. J. Norton, F. Mauer, B. Droney, Eric Albert Ash, C. M. Sayers, Eric Albert Ash, and C. B. Scruby. Ultrasonic measurement of internal temperature distribution. *Philosophical Transactions of the Royal Society of London. Series A, Mathematical and Physical Sciences*, 320, 1986.

[266] Juliano Scholz Slongo, Jefferson Gund, Thiago Alberto Rigo Passarin, Daniel Rodrigues Pipa, Júlio Endress Ramos, Lucia Valeria Arruda, and Flávio Neves Junior. Effects of thermal gradients in high-temperature ultrasonic non-destructive tests. *Sensors*, 22, 2022.

[267] K. Oh and B.I. Epureanu. A novel thermal swelling model for a rechargeable lithium-ion battery cell. *Journal of Power Sources*, 303, 2016.

[268] V.A. Sethuraman, M.J. Chon, M. Shimshak, N. Van Winkle, and P.R. Guduru. In situ measurement of biaxial modulus of si anode for li-ion batteries. *Electrochemistry Communications*, 12, 2010.

[269] Daniel Evans, Daniel Martin Brieske, Claas Tebruegge, and Julia Kowal. Analysis of the impact of manufacturing-induced cell-to-cell variation for high-power applications. *Journal of Power Sources*, 614, 2024.

[270] Sanjay R Arwade, Mohammadreza Moradi, and Arghavan Louhghalam. Variance decomposition and global sensitivity for structural systems. *Engineering Structures*, 32(1):1–10, 2010.

[271] Katerina Konakli and Bruno Sudret. Global sensitivity analysis using low-rank tensor approximations. *Reliability Engineering & System Safety*, 156, 2016.

[272] Matthew Li, Jun Lu, Zhongwei Chen, and Khalil Amine. 30 years of lithium-ion batteries. *Advanced Materials*, 30(33), 2018.

[273] John B. Goodenough and Kyu-Sung Park. The li-ion rechargeable battery: A perspective. *Journal of the American Chemical Society*, 135(4), 2013.

[274] George E. Blomgren. The development and future of lithium ion batteries. *Journal of The Electrochemical Society*, 164(1), 2016.

[275] Haifeng Dai, Bo Jiang, Xiaosong Hu, Xianke Lin, Xuezhe Wei, and Michael Pecht. Advanced battery management strategies for a sustainable energy future: Multilayer design concepts and research trends. *Renewable and Sustainable Energy Reviews*, 138, 2021.

[276] Qian Lin, Jun Wang, Rui Xiong, Weixiang Shen, and Hongwen He. Towards a smarter battery management system: A critical review on optimal charging methods of lithium ion batteries. *Energy*, 183, 2019.

[277] Guangfang Hu, Peifeng Huang, Zhonghao Bai, Qingsong Wang, and Kaixuan Qi. Comprehensively analysis the failure evolution and safety evaluation of automotive lithium ion battery. *ETransportation*, 10, 2021.

[278] Ting Cai, Puneet Valecha, Vivian Tran, Brian Engle, Anna Stefanopoulou, and Jason Siegel. Detection of li-ion battery failure and venting with carbon dioxide sensors. *ETransportation*, 7, 2021.

[279] Leo Wildfeuer and Markus Lienkamp. Quantifiability of inherent cell-to-cell variations of commercial lithium-ion batteries. *ETransportation*, 9, 2021.

[280] Long Zhou, Xin Lai, Bin Li, Yi Yao, Ming Yuan, Jiahui Weng, and Yuejiu Zheng. State estimation models of lithium-ion batteries for battery management system: Status, challenges, and future trends. *Batteries*, 9(2), 2023.

[281] Shuai Ma, Modi Jiang, Peng Tao, Chengyi Song, Jianbo Wu, Jun Wang, Tao Deng, and Wen Shang. Temperature effect and thermal impact in lithium-ion batteries: A review. *Progress in Natural Science: Materials International*, 28(6):653–666, 2018.

[282] Wenlu Zhou, Yanping Zheng, Zhengjun Pan, and Qiang Lu. Review on the battery model and soc estimation method. *Processes*, 9, 2021.

[283] Xin Xiong, Shun-Li Wang, Carlos Fernandez, Chun-Mei Yu, Chuan-Yun Zou, and Cong Jiang. A novel practical state of charge estimation method: an adaptive improved ampere-hour method based on composite correction factor. *International journal of energy research*, 44, 2020.

[284] Junfu Li, Lixin Wang, Chao Lyu, and Michael Pecht. State of charge estimation based on a simplified electrochemical model for a single licoo2 battery and battery pack. *Energy*, 133, 2017.

[285] Xuanju Dang, Li Yan, Kai Xu, Xiru Wu, Hui Jiang, and Hanxu Sun. Open-circuit voltage-based state of charge estimation of lithium-ion battery using dual neural network fusion battery model. *Electrochimica Acta*, 188, 2016.

[286] Ali Jokar, Barzin Rajabloo, Martin Désilets, and Marcel Lacroix. Review of simplified pseudo-two-dimensional models of lithium-ion batteries. *Journal of Power Sources*, 327:44–55, 2016.

[287] Christopher R. Lashway and Osama A. Mohammed. Adaptive battery management and parameter estimation through physics-based modeling and experimental verification. *IEEE Transactions on Transportation Electrification*, 2:454–464, 2016.

[288] Zhenhua Cui, Licheng Wang, Qiang Li, and Kai Wang. A comprehensive review on the state of charge estimation for lithium-ion battery based on neural network. *International Journal of Energy Research*, 46(5), 2022.

[289] Ingvild B Espedal, Asanthi Jinasena, Odne S Burheim, and Jacob J Lamb. Current trends for state-of-charge (soc) estimation in lithium-ion battery electric vehicles. *Energies*, 14(11):3284, 2021.

[290] Emanuele Buchicchio, Alessio De Angelis, Francesco Santoni, Paolo Carbone, Francesco Bianconi, and Fabrizio Smeraldi. Battery soc estimation from eis data based on machine learning and equivalent circuit model. *Energy*, 283:128461, 2023.

[291] Uwe Westerhoff, Thorsten Kroker, Kerstin Kurbach, and Michael Kurrat. Electrochemical impedance spectroscopy based estimation of the state of charge of lithium-ion batteries. *Journal of Energy Storage*, 8, 2016.

[292] D Andre, M Meiler, K Steiner, Ch Wimmer, T Soczka-Guth, and DU Sauer. Characterization of high-power lithium-ion batteries by electrochemical impedance spectroscopy. i. experimental investigation. *Journal of Power Sources*, 196(12), 2011.

[293] Yuechen Liu, Linjing Zhang, Jiuchun Jiang, Shaoyuan Wei, Sijia Liu, and Weige Zhang. A data-driven learning-based continuous-time estimation and simulation method for energy efficiency and coulombic efficiency of lithium ion batteries. *Energies*, 10(5), 2017.

[294] Xiao Feng, Yang Zhang, Le Kang, Licheng Wang, Chongxiong Duan, Kai Yin, Jinbo Pang, and Kai Wang. Integrated energy storage system based on triboelectric nanogenerator in electronic devices. *Frontiers of Chemical Science and Engineering*, 15, 2021.

[295] Lawnardo Sugiarto, Zijie Huang, and Yi-Chun Lu. Battery lifetime prediction using surface temperature features from early cycle data. *Energy Environ. Sci.*, 18, 2025.

[296] Zhe Li, Jun Huang, Bor Yann Liaw, and Jianbo Zhang. On state-of-charge determination for lithium-ion batteries. *Journal of Power Sources*, 348, 2017.

[297] Chong Bian, Huoliang He, and Shunkun Yang. Stacked bidirectional long short-term memory networks for state-of-charge estimation of lithium-ion batteries. *Energy*, 191, 2020.

[298] Jie Wang. An intuitive tutorial to gaussian process regression. *Computing in Science & Engineering*, 25(4), 2023.

[299] Matteo Galeotti, Lucio Cinà, Corrado Giammanco, Stefano Cordiner, and Aldo Di Carlo. Performance analysis and soh (state of health) evaluation of lithium polymer batteries through electrochemical impedance spectroscopy. *Energy*, 89, 2015.

[300] Elixabete Sarasketa-Zabala, Egoitz Martinez-Laserna, Maitane Berecibar, Inigo Gandiaga, Lide Mercedes Rodriguez-Martinez, and Igor Villarreal. Realistic lifetime prediction approach for li-ion batteries. *Applied energy*, 162, 2016.

[301] Chunrong Zhao, Wenjiong Cao, Ti Dong, and Fangming Jiang. Thermal behavior study of discharging/charging cylindrical lithium-ion battery module cooled by channeled liquid flow. *International Journal of Heat and Mass Transfer*, 120:751–762, 2018.

[302] Panding Wang, Xinyi Zhang, Le Yang, Xingyu Zhang, Meng Yang, Haosen Chen, and Daining Fang. Real-time monitoring of internal temperature evolution of the lithium-ion coin cell battery during the charge and discharge process. *Extreme Mechanics Letters*, 9:459–466, 2016. Mechanics of Energy Materials.

[303] Kaiyang Zeng and Jing Zhu. Surface morphology, elastic modulus and hardness of thin film cathodes for li-ion rechargeable batteries. *Mechanics of Materials*, 91:323–332, 2015.

[304] Arthur L Samuel. Some studies in machine learning using the game of checkers. *IBM Journal of research and development*, 3(3):210–229, 1959.

[305] Tom M Mitchell and Tom M Mitchell. *Machine learning*, volume 1. McGraw-Hill New York, 1997.

[306] Asif Mahmood and Jin-Liang Wang. Machine learning for high performance organic solar cells: current scenario and future prospects. *Energy Environ. Sci.*, 14:90–105, 2021.

[307] Tânia F. G. G. Cova and Alberto A. C. C. Pais. Deep learning for deep chemistry: Optimizing the prediction of chemical patterns. *Frontiers in Chemistry*, Volume 7, 2019.

[308] Felipe L. Gewers, Gustavo R. Ferreira, Henrique F. De Arruda, Filipi N. Silva, Cesar H. Comin, Diego R. Amancio, and Luciano Da F. Costa. Principal component analysis: A natural approach to data exploration. *ACM Comput. Surv.*, 54(4), 2021.

[309] Yani Zhu, Chaoyang Zhu, and Xiaoxin Li. Improved principal component analysis and linear regression classification for face recognition. *Signal Processing*, 145, 2018.

[310] C.K.I Williams and C.E. Rasmussen. *Gaussian Processes for Machine Learning*. The MIT Press, 2006.